Measurements and Modification of Sheared Flows and Stability on the Compact Toroidal Hybrid Stellarator

by

Mark Cianciosa

A dissertation submitted to the Graduate Faculty of
Auburn University
in partial fulfillment of the
requirements for the Degree of
Doctor of Philosophy

Auburn, Alabama
May 6, 2012

Keywords: Stellarator, Plasma

Approved by

Edward E. Thomas, Jr., Chair, Professor of Physics
Stephen Knowlton, Professor of Physics
James Hanson, Professor of Physics
Stuart Loch, Professor of Physics

Abstract

Sheared flows arising from spatially inhomogeneous, transverse electric fields are common phenomena found in space, laboratory, and fusion plasmas. These flows are a source of free energy that can drive or suppress instabilities. In space plasmas, numerous observations of electrostatic and electromagnetic instabilities at various scale lengths have been made. By contrast, in fusion plasmas, edge localized sheared flows provide a barrier against cross field particle transport and the presence of these flows are associated with enhanced confinement regimes (H-mode). Understanding how these flows provide enhanced confinement is of critical importance to current and future fusion experiments. This work is an experimental investigation of sheared flow generation and the corresponding response of the plasma in a stellarator type fusion device.

This work is performed in the Compact Toroidal Hybrid (CTH) stellarator device. The CTH stellarator is a five field period continuously wound stellarator run with $100ms$ long plasmas. Primary plasma generation and heating is provided through Electron Cyclotron Resonance Heating (ECRH) with a secondary Ohmic heating system. Flow experiments are performed by modifying the radial electric field by inserting a biased electrode past the last closed flux surface. Plasma parameters are measured using a Triple Probe. Plasma flows are measured using a Gundestrup Probe.

Flows in CTH are studied by examining the effects that three dimensional geometries have on fluid flows. The interpretation of probe measurements in highly shaped fields is achieved by transforming laboratory space positions to magnetic flux coordinate space positions. Biasing experiments will modify the edge electric fields, measure the induced flows, demonstrate the role electric fields play inducing flows and measure the enhancement or degradation of plasma stability in the presence of these flows. Instabilities that arise will be identified by examining various parameter scales to narrow down the vast spectrum of plasma instabilities.

Acknowledgments

I would like to start by thanking mom and dad for putting up with me though out this long process. Paying my way though under my undergrad education was the greatest gift someone can give. I would like to thank all the physics professors at SUNY Potsdam. You set the bases for my career to come. A special thanks goes out to Dr. William E. Amatucci, Dr. Gurudas Ganguli and all the people I worked with at NRL. Though you I got my start in plasma physics, met my future thesis advisor and ended up at Auburn University.

In my time at Auburn, I need to thank all the people I have worked with through out the years. Everyone that I have worked with in the Plasma Sciences Laboratory and the Compact Toroidal Hybrid groups has made this work possible. Finally to my thesis committee for reading though this long document and making my defense seem less painless than I thought it was going to be. Finally and most importantly, I thank Dr. Edward E. Thomas Jr., my thesis advisor. None of this would be possible without the research Grant awards, mentoring and friendship over the years.

Table of Contents

List of Figures

List of Tables

List of Abbreviations

Φ_f	Floating Potential
$\bar{\iota}$	Rotational Transform
m_e	Electron Mass
m_i	Ion Mass
n_e	Electron Density
Φ	Electric Potential
Φ_p	Plasma Potential
B^u	Contravariant component of magnetic field in $\boldsymbol{e}_u$ direction.
B^v	Contravariant component of magnetic field in $\boldsymbol{e}_v$ direction.
B_s	Covariant component of magnetic field in $\boldsymbol{e}^s$ direction.
B_u	Covariant component of magnetic field in $\boldsymbol{e}^u$ direction.
B_v	Covariant component of magnetic field in $\boldsymbol{e}^v$ direction.
c_s	Acoustic speed.
e	Elementary charge
I	Current
J	Jacobian
k_b	Boltzmann constant

M	Ratio of speed to c_s.
r_L	Larmor Radius
T_e	Electron Temperature
T_i	Ion Temperature
Z	Ionization number
CTH	Compact Toroidal Hybrid
FFT	Fast Fourier Transform
LCFS	Last Closed Flux Surface
MHD	Magnetohydrodynamic
RK4	4^{th} order Runge-Kutta
UHV	Ultra High Vacuum

Chapter 1

Introduction

The standard of living in the modern western world is made possible through the generation of abundant energy mainly in the form of electricity. Electricity right now is generated by various non-renewable means such as coal, oil, natural gas and nuclear and renewable sources such as wind, solar and hydro power. Each system has its strengths and weaknesses. Coal, oil and natural gas represent relatively cheap energy sources with a mature technological basis that enables power plants that are simple to build and operate, and allow continuous generation of electricity. However, they come at a cost of environmental damage via the generation of harmful chemicals and the generation of greenhouse gases during normal operation. Moreover, these sources all have a finite fuel supply that at current consumption levels could be depleted within the next century.

The current generation of renewable energy technologies, particularly wind and solar, are clean forms of energy avoiding the generation of harmful chemicals and greenhouse gases. Further more, energy is extracted from resources with little danger of being depleted on short time scales. However these sources are often dependent on local climate and weather conditions such as wind patterns and cloud cover which may vary. These technologies are still relatively immature and expensive compared to fossil fuels. As such, these sources cannot be solely relied upon for continuous industrial scale production of electrical power.

There are two forms of energy production where the properties of matter at the atomic level can be leveraged. One form is nuclear fission where energy is generated from the break up and decay of heavy elements. Developed during the 1950s, nuclear fission power accounts for 19.6% of power generated in the United States today[2]. However, fears over safety and nuclear proliferation have resulted in a reluctance to rely on fission as a future energy source. The second form of nuclear

energy, fusion, is an actively researched energy source with the goal of safe clean abundant energy generation.

1.1 Fusion

Fusion is a process where by lighter nuclei combine to form heavier nuclei. This fusion of particles is accompanied by a release of energy. In the sun naturally occurring deuterium-deuterium ($D = H^2$)

$$D + D \rightarrow T\,(1.01\text{ MeV}) + p(3.02\text{ MeV}) \tag{1.1a}$$

$$D + D \rightarrow He^3\,(0.82\text{ MeV}) + n(2.45\text{ MeV}) \tag{1.1b}$$

powers the sun in equal amounts.

In order for two particles to fuse however, the nuclei must overcome the Coulomb repulsion. Classically the Coulomb barrier is on the order of 1 MeV. However quantum mechanics allows for particles of lower incident energies to tunnel through this barrier. Figure 1.1 show various fusion cross sections for several fusion reactions[1]. The fusion cross-section represents the probability of an incident particle, of a certain energy, to overcome the Coulomb barrier.

While there are many possible fusion reactions, the particular process of interest for controlled fusion is the deuterium-tritium (DT, $T = H^3$) reaction defined as,

$$D + T \rightarrow He^4\,(3.5\text{ MeV}) + n\,(14.1\text{ MeV}) \tag{1.2}$$

where a 3.5 MeV α particle and a 14.1 MeV neutron are produced. This process has the highest fusion cross-section at low incident energies. However it still requires plasmas with thermal energies in the range of 10 keV.

This presents a challenge to a fusion power plant as plasmas in this range can cause damage to a vessel created to contain it. Aside from stars which use gravity to confine the hot plasma, there are two types of fusion confinement methodologies employed today. Inertial confinement, where

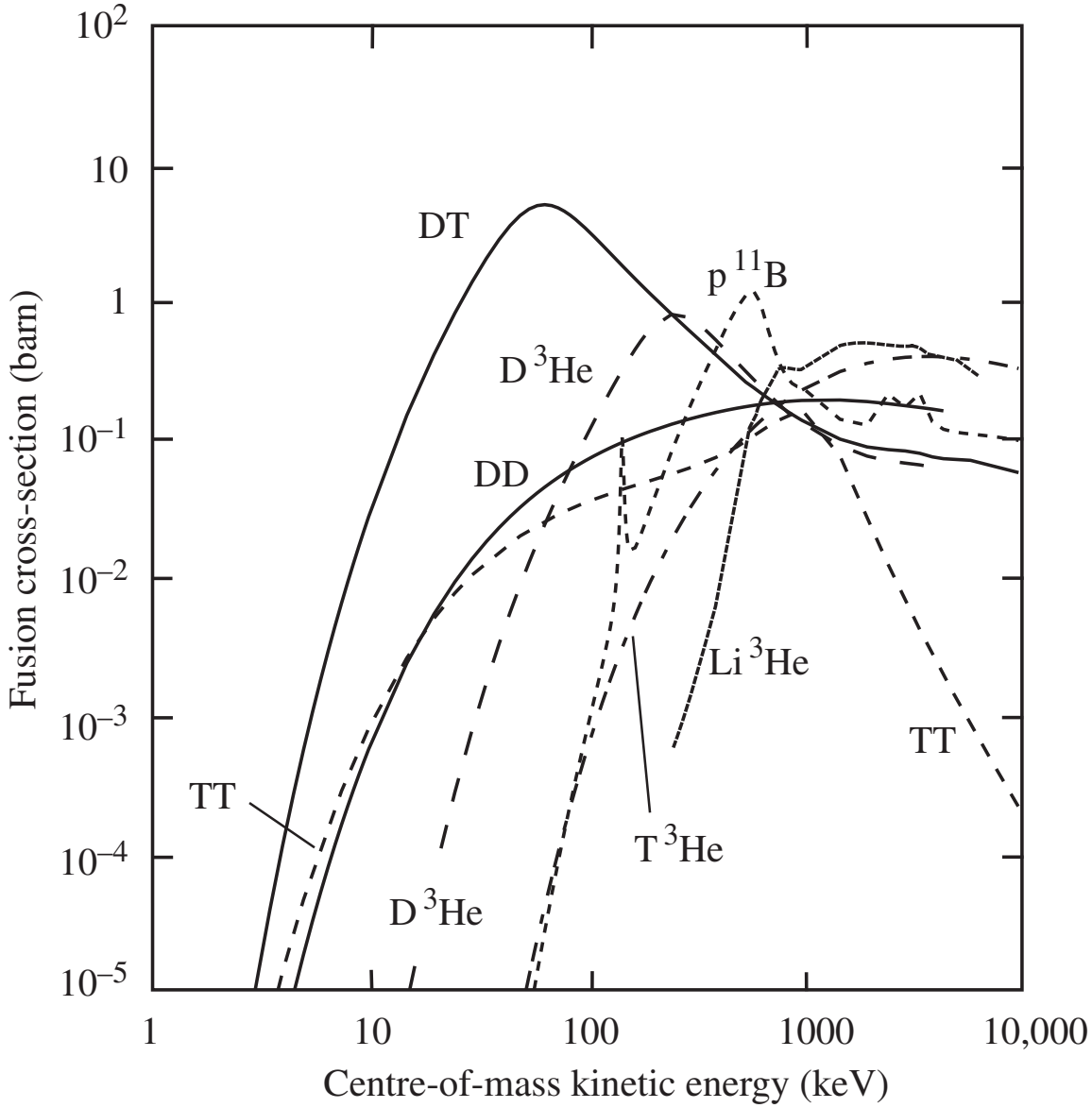

Figure 1.1: Fusion cross-sections for various fusion reactions[1].

typically focused high power lasers are used to compress the fusion fuel, is outside the scope of this dissertation. The type of fusion confinement related to the work in this dissertation is magnetic confinement, where magnetic fields are used to hold the plasma.

1.2 Magnetic Confinement

A charged particle in a magnetic field experiences the Lorentz force given by

$$\boldsymbol{F}_m = q\boldsymbol{v} \times \boldsymbol{B} \tag{1.3}$$

where $\boldsymbol{F}_m$ force of the magnetic field ($\boldsymbol{B}$) on a charged particle. q is the electric charge and $\boldsymbol{v}$ is the velocity of the charged particle. For a particle moving perpendicular to a magnetic field line, the Lorentz force produces a force pulling the particle toward that field line. This causes the particle to orbit around the magnetic field line with a characteristic frequency called the gyro frequency

$$\Omega_\alpha = \frac{|q|B}{m} \tag{1.4}$$

at a characteristic radius known as the Larmor radius,

$$\rho_L = \frac{mv_\perp}{|q|B} \tag{1.5}$$

where m is the mass of a charged particle and $v_\perp$ is the component of the particle velocity perpendicular to the magnetic field vector $\boldsymbol{B}$. In the absence of collisions, this orbital motion traps the particle on the magnetic field line. An infinitely long magnetic field would confine a particle indefinitely however, this configuration is impossible to build. Therefore magnetic confinement research is tasked with challenge of developing a "finite" magnetic configuration that can confine a thermonuclear plasma with minimal losses.

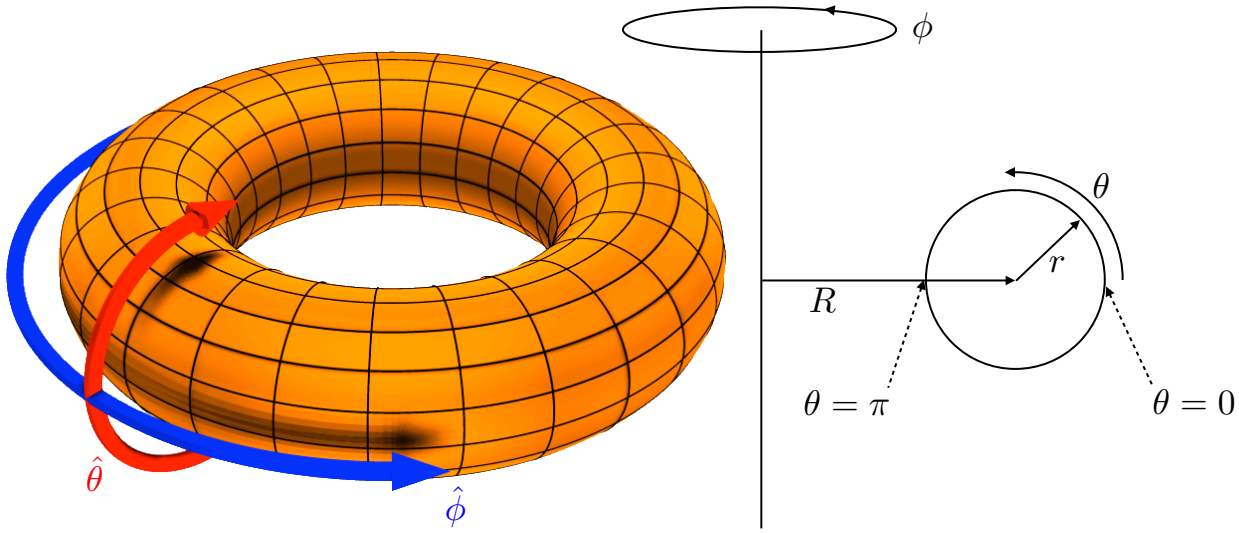

Figure 1.2: A torus. The blue arrow points in the toroidal direction. The red arrow points in the poloidal direction. The drawing on the right shows the major radius R, minor radius r and the directions of increasing toroidal ϕ and poloidal θ angle.

1.2.1 Toroidal Devices

In an attempt to produce an "infinitely long" magnetic field, consider a configuration in which the field lines are curved back onto themselves avoiding contact with a vessel wall. This leads to the most common geometry of magnetic confinement devices, the torus is shown in Figure 1.2. The geometry of a torus is decried by a major radius measured from the central core to the center of the machine. The angle ϕ sweeps a direction the long way around the torus or the toroidal direction. In this dissertation, the angle ϕ is measured counterclockwise as seen from looking down on the top of the torus.

The minor radius (r) is measured from the end of the major radius (R). The angle θ sweeps a direction the short way around the torus or the poloidal direction. At any toroidal cross-section, the angle θ is measured counterclockwise. That is, the outboard side is at an angle of $\theta = 0$ with inboard side at $\theta = \pi$. The top and bottom are located at $\theta = \frac{\pi}{2}$ and $\theta = \frac{3\pi}{2}$ respectively.

The curvature of the magnetic lines causes a larger magnetic field strength to be produced on the inboard side, where the magnetic field lines become compressed, as compared to the outboard

side. This gradient in the magnetic field introduces a particle drift given by[3]

$$\boldsymbol{v}_{\nabla B} = \pm \frac{v_\perp r_L}{2} \frac{\boldsymbol{B} \times \nabla B}{B^2} \tag{1.6}$$

where r_L is the Larmor radius defined by equation 1.5. The $\pm$ is determined by the sign of the charge of a particle. In addition this curvature causes a drift defined by

$$\boldsymbol{v}_R = \frac{m v_\parallel^2}{qB^2} \frac{\boldsymbol{R}_c \times \boldsymbol{B}}{R_c^2} \tag{1.7}$$

where R_c is a radius of curvature. Because these two drifts are additive, particles in a purely toroidal magnetic field will acquire a vertical drift and eventually intersect the vessel wall.

To nullify the inherent vertical drift of charged particles in a purely toroidal magnetic field, a poloidal component is added to the magnetic field. This component creates a twisting of the field lines and produces a helical-toroidal trajectory of the magnetic field line. A consequence of this magnetic geometry, is that a particle traveling along a field line that is drifting up on the outboard side, will begin to drift down as the field line curves down on the inboard side. Moreover, the addition of the poloidal magnetic field leads to the generation of magnetic flux surfaces.

Modern magnetic fusion devices vary in the production of magnetic fields from configurations where magnetic fields are produced entirely from external coils to configurations where the magnetic field is generated by a combination of external and induced currents in the plasma itself. This dissertation will focus on measurements performed on a stellarator, a toroidal fusion configuration in which the magnetic field is produced entirely by external coils. However, a number of the phenomena observed in the work have also been reported in tokamaks, a current-carrying toroidal plasma configuration. Because of data from both tokamak and stellarator devices will be discussed in this work, a brief description of each device is given.

Tokamak

The tokamak is a device producing a toroidally symmetric magnetic geometry with nested magnetic surfaces. In tokamaks, the poloidal component to the magnetic field is provided by a toroidally driven plasma current induced by a transformer. The degree of "twist" of the magnetic field in a tokamak is parameterized by the safety factor q, the ratio of the number of times a magnetic field line traverses toroidally per the number of times that a magnetic field line traversed poloidally. In addition to providing a poloidal twist, the driven plasma current has the added benefit of heating the plasma. The simplicity of the design lead to rapid early advances in tokamak performance. By 1968 it was revealed at the Novosibirsk Conference that the Russian T-3 tokamak was achieving electron temperatures of 100 eV with energy confinement times of $2 - 4$ ms, well ahead of its contemporary devices[4]. Today the tokamak is dominant device for advanced fusion concepts and is the configuration that has been chosen for the ITER project.

The presence of plasma current, while allowing the tokamak to achieve high temperatures and densities, is also a tremendous reserve of free energy that can drive a wide range of magnetohydrodynamic (MHD) instabilities. The most dangerous of these is an event known as a disruption in which there is a global reordering of the plasma and a complete loss of confinement. These disruptions can have a detrimental, even damaging effect on devices as hot dense plasma crashes into the vessel wall. One focus of current tokamak research is on the detection and mitigation of disruptions.

Typical methods of driving plasma currents involve a large central transformer. By ramping up the current in the transformer, a current is induced in the plasma. However, this limits the length of time plasma current can be sustained. This makes the tokamak an inherently pulsed device and to date there are no operating steady state tokamaks.

Stellarator

In contrast to tokamaks, the magnetic fields in a stellarator are generated completely from external magnetic coils. The degree of "twist" in stellarators is parameterized by the rotational

transform $\bar{\iota}$. This parameter is related to the safety factor in tokamaks as $\bar{\iota} = q^{-1}$. A mathematical definition of $\bar{\iota}$ will be provided in Appendix B.1.

In stellarators, there is no need to drive a high plasma current. This makes stellarators resistant to current driven instabilities and disruptions. The lack of a transformer to drive a plasma current means that the stellarator is inherently a steady state device. However, historically the stellarator suffered poor confinement brought about by a "rippled" magnetic field. Along a field line, the magnetic field strength varies on short length scales. This has the effect of producing small magnetic wells that a particle can become trapped in. If a particle becomes trapped in these magnetic wells the gradient and curvature drifts (equations 1.6 and 1.7) will cause the particles to eventually drift to the wall.

Modern stellarator research is focused on magnetic topologies that minimize these magnetic ripples. In order to achieve this, complex three-dimensional magnetic coils are required. However, the complexity of these coils needed to create the three-dimensional magnetic fields, presents a design challenge compared to the tokamak's simpler design. In order to achieve good confinement and nested stellarator magnetic surfaces, tight tolerances and minimization of external magnetic perturbations are necessary. This along with lack of a simple efficient heating mechanism has resulted in the stellarator not achieving the same level of performance as the tokamaks until the 1980's[4]. Still today the highest performing stellarators still fall short of the highest performing tokamaks[5].

As of 2012, the largest stellarator currently in operation is the Large Helical Device (LHD) in Japan. LHD is a non-optimized configuration with superconducting coils. In Germany, the Wendelstine 7-X (W7-X) stellarator is currently under construction[6]. W7-X is an optimized stellarator configuration with superconducting coils designed to study a fully optimized configuration, where magnetic fields have been carefully designed to minimize particle loses. In the United States, there are two operating stellarators. The Helically Symmetric eXperiment (HSX)[7] located at University of Wisconsin in Madison, Wisconsin. HSX is designed to demonstrate and study quasi-helical symmetry, where the trapping of particles due to the stellarator ripple is reduced. The

second operating stellarator, and focus of this dissertation, is the Compact Toroidal Hybrid (CTH) located at Auburn University in Auburn, Alabama.

1.3 The CTH Device

The CTH device is a five field period continuously wound stellarator. The *hybrid* nature comes from the inclusion of toroidal field (TF) coils and ohmic heating (OH) coils. The presence of these features allow the CTH device to be operated in a spectrum from stellarator-like with high vacuum rotational transforms $\bar{\iota}$, to a more tokamak-like low vacuum $\bar{\iota}$. The OH also has the added benefit of providing plasma heating. CTH was designed to allow the superposition of three-dimensional magnetic fields and current driven poloidal fields, for the purposes of understanding the limits where the traditional stability of the stellarator breaks down as it becomes more tokamak like.

1.3.1 Magnets

CTH's magnetic field is produced from seven sets of coils. Figure 1.3 shows a diagram of the major coil sets. The Helical Field (HF) coil provides the main toroidal and poloidal fields but does not provide the entire vertical field magnitude required for equilibrium. The HF coil is a continuously wound helical coil using a $l = 2$, $m = 5$ winding law. This means that this coil wraps the vacuum vessel five times poloidally and rejoins itself after traversing the vacuum vessel twice toroidally. The helical portion of the HF coils is connected in series to a set of vertical coils mounted above and below the helical winding. The rest of the vertical field is provided by the Trim Vertical Field (TVF) coils. Figure 1.4 shows various nested flux surface cross-sections produced by the HF and TVF coils.

The Ohmic Heating (OH) coils are a set of inductive coils, mounted in the center of the torus, used to drive a plasma current. A rapidly changing field in this coil set, induces a toroidal plasma current. This current heats the plasma and creates a poloidal magnetic fields like a tokamak. Since fields produces by this coil set are constantly changing, magnetic diagnostics will pick up its signal. To minimize this effect, this coil set is designed in such a way that it does not provide significant

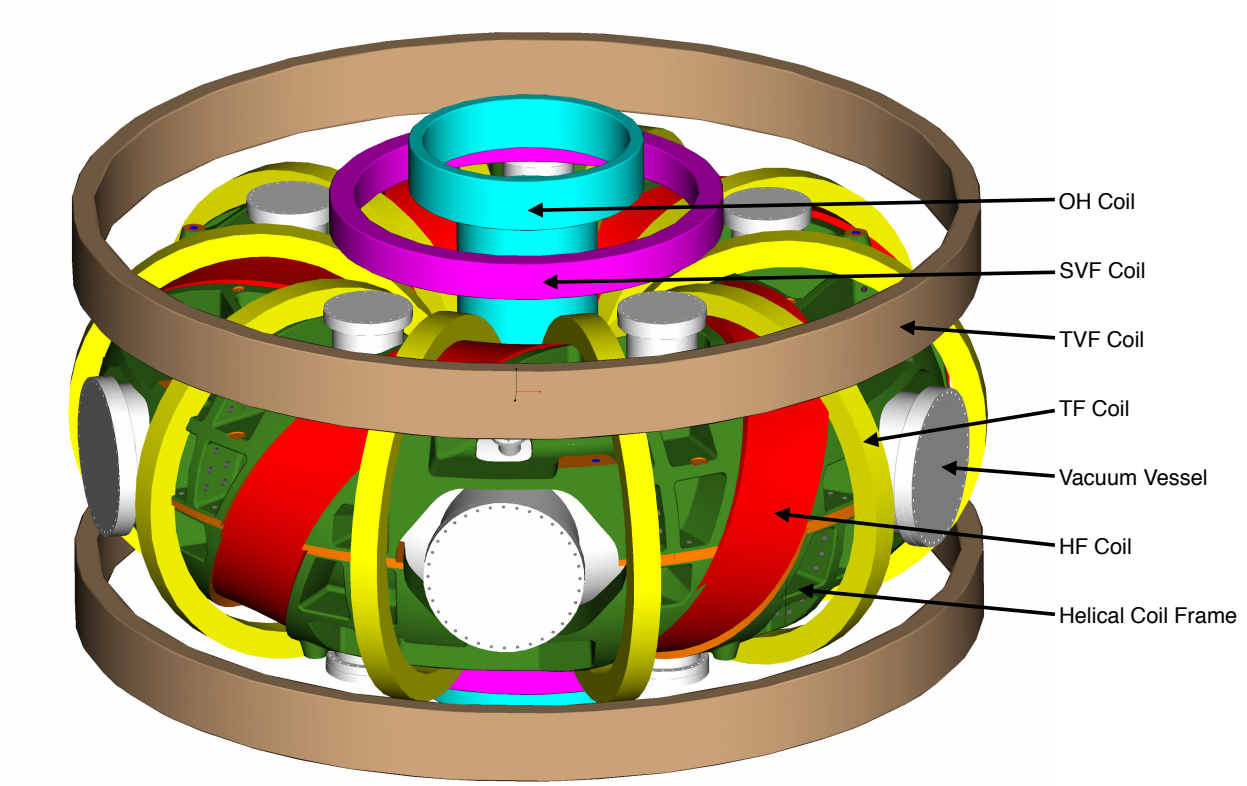

Figure 1.3: Schematic of the CTH device showing the Vacuum Vessel, Helical Coil Frame and various Coil sets.

field within the vacuum vessel. This coil set is powered by a capacitor bank. For this dissertation the OH system was not used. All results are presented in plasmas without plasma current.

The remaining coil sets are for varying the basic stellarator magnetic fields. The Toroidal Field (TF) coils are a set of ten coils that produce a toroidal field. On a tokamak, this coil set would produce the main magnetic field. These coils allow adjustment from stellarator like high $\bar{\iota}$ to a more tokamak like low $\bar{\iota}$ by adding or subtracting from the toroidal component of the HF coils.

The Shaping Vertical Field (SVF) coils provide a quadrupole field for controlling the vertical elongation of the plasmas. Radial Field (RF) coils shifts the vertical position of the plasma. Error Correction Coils (ECC) are a set of fifteen coils wrapped around horizontal and vertical ports. These coils provide a local radial field to correct for local asymmetries in the magnetic field.

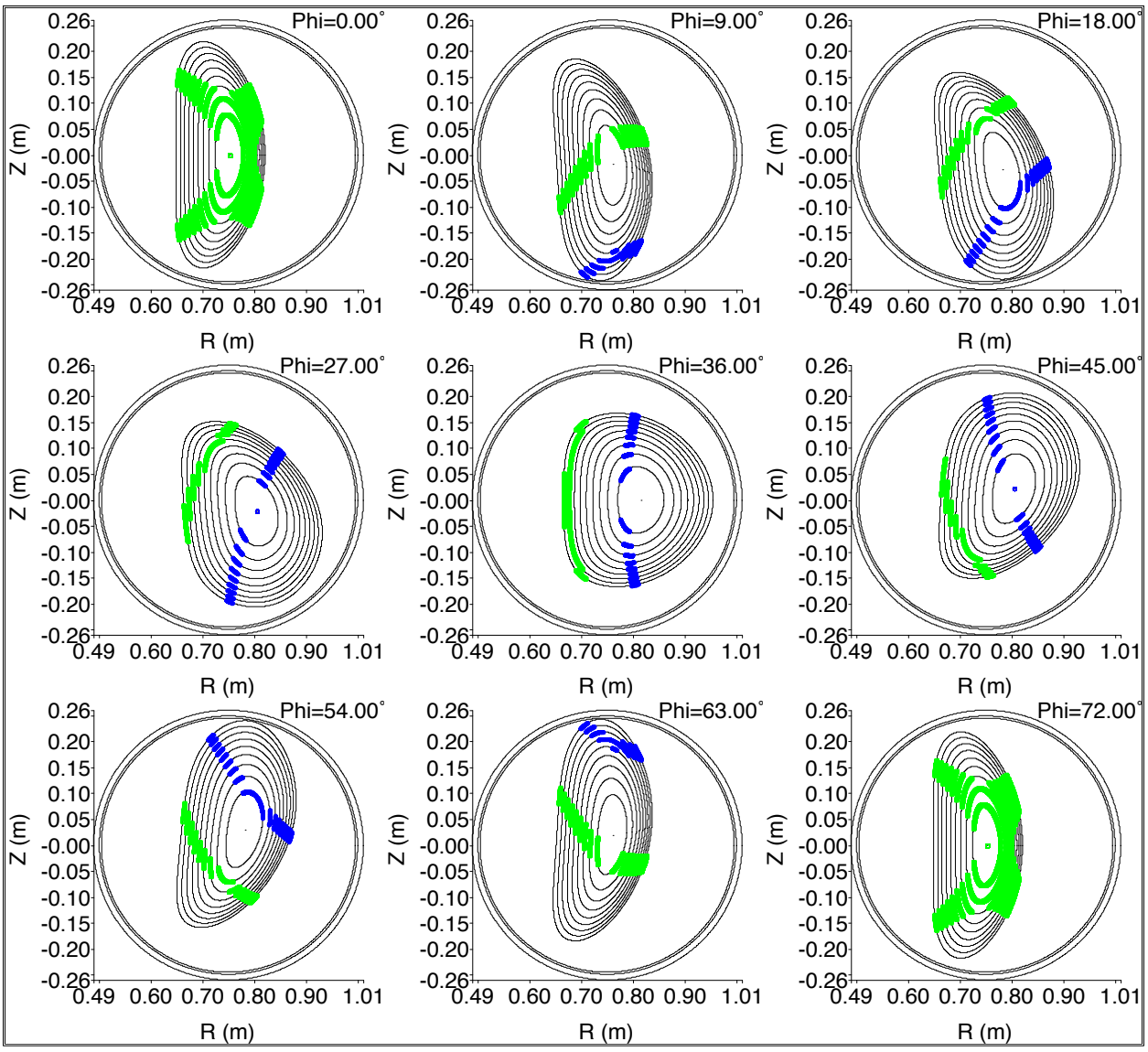

Figure 1.4: Various flux surfaces produced from the HF and TVF coils. Shaded regions shows magnetic field resonances for the various heating systems.

1.3.2 Mission of CTH

For all toroidal fusion devices, there remains a number of outstanding physics issues to be addressed before a true fusion power plant can be built. Among the critical issues are the interaction of the plasma with the surrounding walls, development of global, predictive models of the behaviors of thermonuclear "burning" plasma, and, of particular relevance to this dissertation, the control of particle transport and instabilities in the plasma.

Major projects completed and currently ongoing on CTH involve mapping and reconstructing the equilibrium magnetic fields. Mapping of the magnetic field performed by Peterson et al.[8], who developed a model of the magnetic field. It was show how the presence of magnetic errors can be enhanced or reduced through the use of external coils. Work modeling the magnetic fields was built upon by B.A. Stevenson for use in performing plasma equilibrium reconstructions from diagnostic measurements[9]. This dissertation builds upon this previous work for interpretation of probe measurements.

The ability to accurately model the magnetic field and reconstruct the plasma equilibrium, plays a vital role in the primary mission of CTH. The hybrid nature of CTH was produced to study the effects of plasma disruptions in stellarators with significant plasma current. The general shape and structure of CTH stellarator fields are varied to see the effects it has on current driven disruptions. The goal is to map out the boundaries where the stability of the stellarator design begins to break down as plasma current becomes the dominant effect. These studies are aimed at addressing the central questions of the CTH research program on disruption effects in stellarators.

1.4 Flows in Plasmas

Some 30 years ago, studies performed on the ASDEX tokamak in Germany discovered an enhanced confinement regime of a toroidal plasma[10]. This regime, referred to as the "High" confinement (H-Mode), was characterized by an increase in density and temperature accompanied by a decrease in transport to the walls[11]. This regime exists as a common mode achievable on most large tokamaks[12–16] and stellarators[17,18].

Extensive electric field measurements[11,19] of H-mode edge electric fields, show the generation of a radially inward (negative) electric field from the ambipolar diffusion of ions and electrons in the edge plasma. This negative electric field is consistent across various fusion devices that achieve H-mode. This negative electric field is sheared over a distance of ~ 3 cm in the plasma edge. Sheared electric fields drive a sheared perpendicular flow in the plasma[20–23]. This sheared flow is credited with the formation of a particle transport barrier[24–26] and can reduce the large scale turbulence[27–29] in the plasma. In general, sheared flows are thought to be stabilizing in fusion plasmas.

By contrast, in space and laboratory plasmas, sheared flows are a source of free energy that can drive a wide spectrum of plasma instabilities[30]. The instability mode that can be generated varies based the direction of flow shear and on the scale sizes of the system. Specifically, the size of the ion Larmor radius (ρ_i) to the size of the shear layer (L), plays an important condition on the instability generated. When $\rho_i \gg L$, instabilities with frequencies greater than the ion cyclotron frequency (Ω_{ci}) may be generated. When $\rho_i \sim L$, instabilities with frequencies on the order the ion cyclotron frequency may be generated. When $\rho_i \ll L$, instabilities with frequencies much less than the ion cyclotron frequency may be generated. Extensive experiments in the generation and suppression of these various instabilities has been performed extensively in laboratory plasmas[31,32]. In general, for space and laboratory plasmas, sheared flows are thought to be destabilizing.

While negative electric fields produce stabilizing flows in the edge of fusion plasmas, the generation of radially outward (positive) electric fields have been observed to produce destabilizing effects[33]. Reports range from the generation of a bifurcation of the plasma edge, to the complete loss in particle confinement. In order to achieve the goal of fusion as a viable power source, the optimal operation condition must be achieved. As such, extensive research in to operational mode that show a degradation in performance are not extensively explored.

While this project is in a broad sense connected to the study of H-Mode, it is not an investigation of enhanced confinement regimes. This work considers the plasma response to the generation of edge electric fields and is compared to instability regimes characterized by the size of the ion Larmor radius compared to the electric field scale length, and the instability frequency compared

to the size of the ion cyclotron frequency. Furthermore, building upon the previous work on equilibrium reconstruction in CTH, this project shows how it is possible to use a magnetic field based "Flux" coordinate system to understand diagnostic and flow measurements in highly shaped three-dimensional fields. As such, it extends the work on flows and edge biasing performed on the TEXTOR, CASTOR and T-10 tokamaks[33], and Compact Auburn Torsatron (CAT) and the TJ-II stellarators[34,35].

1.5 Outline of Dissertation

In Chapter 2, an overview of theoretical models necessary to interpret experimental results of this work is presented. Section 2.1 discusses zeroth order flows in the `VMEC` coordinate system. Section 2.2 presents a simulation code developed to interpret the complex particle and fluid behavior. Section 2.3 discusses the role sheared flows have in driving plasma instabilities.

In Chapter 3 a description and the theory of operation of all the experimental hardware is presented. Section 3.1 presents an overview of the CTH device with key emphasis on key systems utilized through out this dissertation. This section also provides the theory and design of diagnostic systems used for experimental measurements. Section 3.3.1 provides a description of the biasing probe used to modify the edge electric fields and induce a flow in the plasma.

In Chapter 4, the results of various edge biasing experiments will be discussed. The generation of edge electric fields through the use of edge biasing will be verified in the CTH device. Plasma flows parallel and perpendicular to the magnetic fields will be measured. Comparisons of measured flows will show good agreement with theoretical calculations of flows. An instability mode driven by the presence of edge flows will be identified.

Chapter 2

Theory

Electric fields and pressure gradients transverse to the magnetic field can drive plasma flows. In slab plasma geometries these drifts take the form[3]

$$\boldsymbol{v} = \frac{\boldsymbol{E} \times \boldsymbol{B}}{\boldsymbol{B} \cdot \boldsymbol{B}} \tag{2.1}$$

$$\boldsymbol{v} = -\frac{\nabla P \times \boldsymbol{B}}{qn\boldsymbol{B} \cdot \boldsymbol{B}} \tag{2.2}$$

for $\boldsymbol{E} \times \boldsymbol{B}$ and diamagnetic drifts, respectively, where n is the plasma density. When electric fields and density gradients are spatially inhomogeneous, a nonuniform or sheared flow layer in the plasma results.

However, a purely cartesian formulation of flows is complicated by the three-dimensional magnetic fields produced by stellarators. Figure 2.1 shows the three dimensional magnetic surfaces produced by the CTH device. Magnetic fields lines, shown in white, wrap around the torus lying on surfaces of constant magnetic flux. The cross-sectional shape of these surfaces varies by the toroidal angle, as show previously in Figure 1.4.

Electric field and pressure gradients, the primary drivers of perpendicular plasma flows, are assumed to point in the direction perpendicular to the magnetic surfaces assuming certain plasma quantities are constant on a flux surface. The validity of these assumptions will be demonstrated in Section 3.5.2. For this section, electric field will be assumed to point in the direction normal to a magnetic surface.

In Cartesian coordinates, magnetic and electric fields are fully three dimensional. To reduce the dimensionality of these components, a coordinate system based around magnetic surfaces is employed. In this coordinate system, the magnetic field lines become straight lines on surfaces

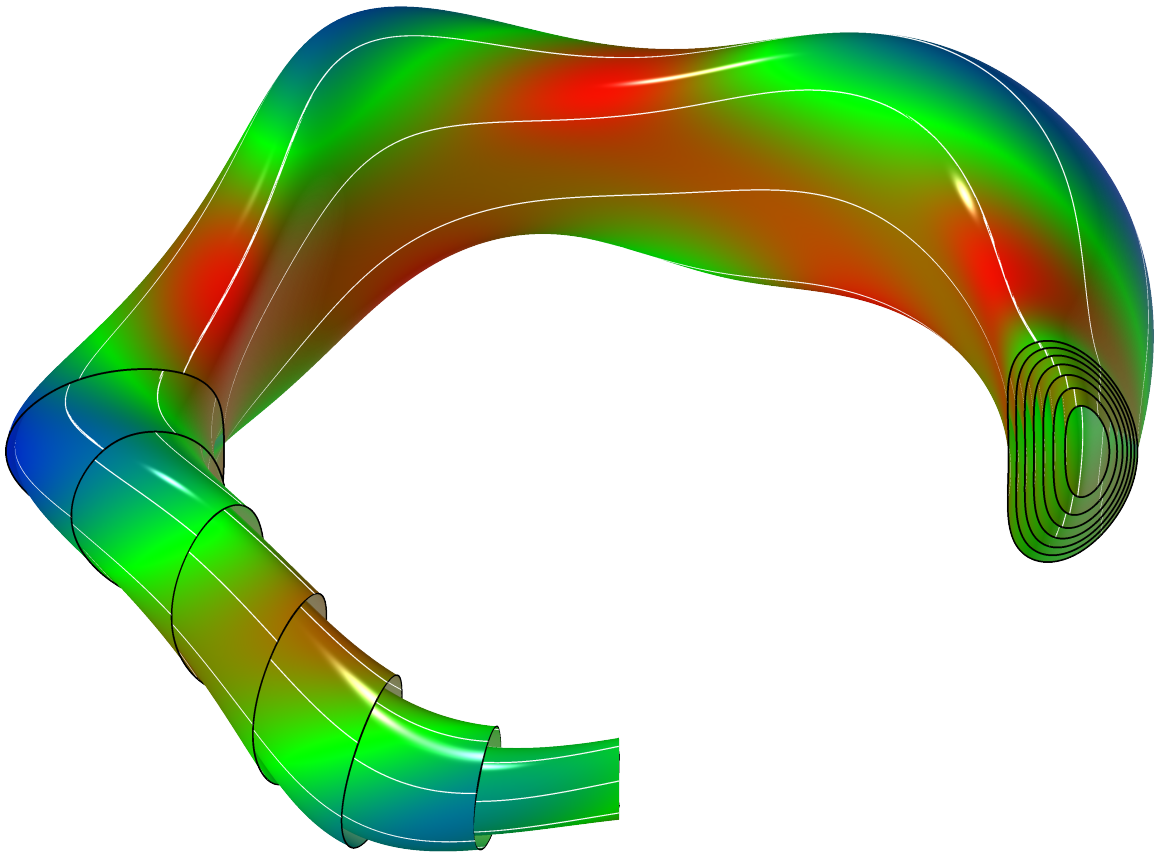

Figure 2.1: Diagram of nested flux surfaces produced from equilibrium reconstruction in the CTH device. Surface color represents $|\boldsymbol{B}|$ between 0.75 T (Red) and 0.25 T (Blue). White lines represent magnetic field lines.

forming concentric cylinders. Electric fields and pressure gradients point in a single radial direction normal to a magnetic surface. The resulting perpendicular flows are limited to these surfaces of constant magnetic flux as well.

While this coordinate system reduces the dimensionality of parameters relevant to plasma flows, it comes at the cost of being no longer orthonormal. A formulation of the mathematical concepts necessary for working in generalized coordinates is provided in Appendix A. One such magnetic coordinate system is the coordinate system used by the Variational Moments Equilibrium Code (`VMEC`)[36,37]. On CTH, `VMEC` is used by the `V3FIT`[38] code to reconstruct the equilibrium magnetic surfaces after each pulse. This coordinate system, overviewed in Appendix B, is used through out this dissertation.

2.1 Plasma Flows

As was discussed in Section 1.4, the presence of plasma flows is an important characteristic of enhanced confinement regimes. For the studies performed on CTH, the contributions of the electric field driven ($\boldsymbol{E} \times \boldsymbol{B}$) and pressure driven (e.g., diamagnetic, $-\nabla P \times \boldsymbol{B}$) drifts are considered as the main drivers of plasma flow. A simple Cartesian model of these drifts fails to take into account geometric corrections. Even simple cylindrical models require geometric corrections compared to Cartesian solutions. In order to account for geometric corrections to the plasma drifts, a fluid approach is employed in the flux coordinate frame.

The ion fluid momentum equation including pressure gradients is[39]

$$\left(\frac{\partial}{\partial t} + \boldsymbol{v} \cdot \nabla\right) \boldsymbol{v} = \frac{e}{m_i} \left(\boldsymbol{E} + \boldsymbol{v} \times \boldsymbol{B}\right) - \frac{\nabla P}{n_i} \tag{2.3}$$

Cross field transport will be assumed to be primarily diffusive in nature, and the velocity vector of a fluid element is assumed to take the form of

$$\boldsymbol{v} = v^u \left(s, u, v\right) \boldsymbol{e}_u + v^v \left(s, u, v\right) \boldsymbol{e}_v \tag{2.4}$$

The magnetic field $\boldsymbol{B}$ is defined using the covariant basis as

$$\boldsymbol{B} = B^u(s,u,v)\,\boldsymbol{e}_u + B^v(s,u,v)\,\boldsymbol{e}_v \tag{2.5}$$

Plasma potential and plasma pressure and assumed to be flux surface constant quantities. Taking the dot product of velocity with the gradient operator becomes

$$\boldsymbol{v}\cdot\nabla = v^u\frac{\partial}{\partial u} + v^u\frac{\partial}{\partial v} \tag{2.6}$$

As a reminder, in generalized coordinates, basis vector can be function of their coordinates. When taking the derivative of a vector quantity, the change in basis vector must also be accounted for. Substituting in all components using the generalized definition of the cross product, the momentum equation becomes

$$\begin{aligned} &g_{su}v^u\frac{\partial v^u}{\partial u} + g_{sv}v^u\frac{\partial v^v}{\partial u} + (v^u)^2\frac{\partial \boldsymbol{e}_u}{\partial u}\cdot\boldsymbol{e}_s + v^uv^v\frac{\partial \boldsymbol{e}_v}{\partial u}\cdot\boldsymbol{e}_s \\ &+g_{su}v^v\frac{\partial v^u}{\partial v} + g_{sv}v^v\frac{\partial v^v}{\partial v} + v^uv^v\frac{\partial \boldsymbol{e}_u}{\partial v}\cdot\boldsymbol{e}_s + (v^v)^2\frac{\partial \boldsymbol{e}_v}{\partial v}\cdot\boldsymbol{e}_s \\ &= \frac{e}{m_i}\left[-\frac{\partial}{\partial s}\Phi_p + J\left(v^uB^v - v^vB^u\right)\right] - \frac{1}{n_i}\frac{\partial}{\partial s}P \end{aligned} \tag{2.7a}$$

$$\begin{aligned} &g_{uu}v^u\frac{\partial v^u}{\partial u} + g_{uv}v^u\frac{\partial v^v}{\partial u} + (v^u)^2\frac{\partial \boldsymbol{e}_u}{\partial u}\cdot\boldsymbol{e}_u + v^uv^v\frac{\partial \boldsymbol{e}_v}{\partial u}\cdot\boldsymbol{e}_u \\ &+g_{uu}v^v\frac{\partial v^u}{\partial v} + g_{uv}v^v\frac{\partial v^v}{\partial v} + v^uv^v\frac{\partial \boldsymbol{e}_u}{\partial v}\cdot\boldsymbol{e}_u + (v^v)^2\frac{\partial \boldsymbol{e}_v}{\partial v}\cdot\boldsymbol{e}_u = 0 \end{aligned} \tag{2.7b}$$

$$\begin{aligned} &g_{uv}v^u\frac{\partial v^u}{\partial u} + g_{vv}v^u\frac{\partial v^v}{\partial u} + (v^u)^2\frac{\partial \boldsymbol{e}_u}{\partial u}\cdot\boldsymbol{e}_v + v^uv^v\frac{\partial \boldsymbol{e}_v}{\partial u}\cdot\boldsymbol{e}_v \\ &+g_{uv}v^v\frac{\partial v^u}{\partial v} + g_{vv}v^v\frac{\partial v^v}{\partial v} + v^uv^v\frac{\partial \boldsymbol{e}_u}{\partial v}\cdot\boldsymbol{e}_v + (v^v)^2\frac{\partial \boldsymbol{e}_v}{\partial v}\cdot\boldsymbol{e}_v = 0 \end{aligned} \tag{2.7c}$$

for the $\boldsymbol{e}^s$, $\boldsymbol{e}^u$ and $\boldsymbol{e}^v$ basis vectors respectively. In Equation 2.7a, J is the Jacobian, Φ_p is the plasma potential, P is the fluid pressure. Components containing elements of the form $\frac{\partial v^{u^i}}{\partial u^j}$ represent the contribution to drift due to magnetic field gradients. Components containing elements of the form $\frac{\partial \boldsymbol{e}_{u^i}}{\partial u^j}$ represent the contribution to the drift due to field line curvature. These elements represent changes in the direction of the basis vectors and can be found in simpler coordinate systems such

as cylindrical coordinates. The remaining terms represent the combined $\boldsymbol{E} \times \boldsymbol{B}$ and $-\nabla P \times \boldsymbol{B}$ drifts.

However, these coupled differential equations are too complex to solve analytically. If we expand the major and minor radii of our toroidal system to infinity, the coordinates become Cartesian as the terms $\frac{\partial \boldsymbol{e}_{u^i}}{\partial u^j} \rightarrow 0$. By ignoring magnetic field gradient and curvature effects, $\frac{\partial v^{u^i}}{\partial u^j} = 0$ and $\frac{\partial \boldsymbol{e}_{u^i}}{\partial u^j} = 0$, equation 2.7 reduces to a simplified form.

$$0 = \frac{e}{m_i}\left[-\frac{\partial}{\partial s}\Phi_p + J\left(v^u B^v - v^v B^u\right)\right] - \frac{1}{n_i}\frac{\partial}{\partial s}P \tag{2.8}$$

These components represent the $\boldsymbol{E} \times \boldsymbol{B}$ and $-\nabla P \times \boldsymbol{B}$. The solution to this equation is the same as the Cartesian solution.

$$\boldsymbol{v} = \frac{\boldsymbol{E} \times \boldsymbol{B}}{\boldsymbol{B} \cdot \boldsymbol{B}} - \frac{\nabla P_i \times \boldsymbol{B}}{e n_i \boldsymbol{B} \cdot \boldsymbol{B}} \tag{2.9}$$

This does not represent a complete solution but is an appropriate approximation for systems where $\boldsymbol{E} \times \boldsymbol{B}$ and $-\nabla P \times \boldsymbol{B}$ are large compared to curvature and gradient drifts. In Section 4.3, this will be shown to be a justifiable assumption for plasmas produced in CTH.

2.2 Particle Trajectory Code

As a need to understand the fluid and single particle motion of the plasma, a single particle code has been developed. The goal of this code is to understand the full motion of the particles incorporating all guiding center drift motions. With the advent of high performance computing and highly parallel processors it is possible to examine large numbers of single particle motions in a reasonable computational time. The source code is available on the CTH archive server.

The simplest method to perform a single particle motion calculation is in Cartesian coordinates. The trajectory code algorithm follows the following basic sequence at each time step. The particle position is converted from (x, y, z) coordinates to (s, u, v) coordinates. The magnetic fields, electric fields and any other parameters that are a function of (s, u, v) are computed. Those parameters are used to calculate the total force acting on a particle in Cartesian coordinates. Using the computed

force model, the particles position and velocity are modified, time is advanced and the algorithm repeats. It should be noted that since all forces acting on the particles are conservative, there are no collisional effects taken into account. This means that time can be advanced forward as well as reversed.

2.2.1 Transformation of Coordinate Systems

This code and the dissertation as a whole, makes extensive use of two coordinate systems. A laboratory space cylindrical (r, ϕ, z) coordinate system and a flux surface space (s, u, v) coordinate system. It is important to understand how positions and vectors are transformed between the two spaces. Moving from a flux surface space position to lab space is performed analytically. Formulas for the transformation of vector quantities and $R(s, u, v)$ and $Z(s, u, v)$ are provided in Appendices A and B. However, in order convert from (r, ϕ, z) coordinates to (s, u, v) coordinates, a two-dimensional root finding must be performed. The flux surface positions of s and u are found at the minimum of the following function

$$f(s, u) = (R(s, u) - R_0)^2 + (Z(s, u) - Z_0)^2 \tag{2.10}$$

where $R(s, u)$ and $Z(s, u)$ have the $v = \phi$ coordinate fixed. R_0 and Z_0 are the laboratory frame coordinates that the (s, u, v) coordinates are being converted from. Once in cylindrical coordinates, the position is converted to Cartesian coordinates using analytical means.

2.2.2 Newton's Method In Optimization

To convert from (r, ϕ, z) space to (s, u, v) space efficiently, equation 2.10 is minimized using Newton's Method[40]. This method expands upon normal gradient descent methods by taking into account second derivatives to aid in faster convergence. Gradient descent methods work to find the minimum of a function by continuously moving parameters "downhill". That is, at each step the gradient of a function $f(\boldsymbol{x}_i)$ is determined to find a direction of decreasing slope such that

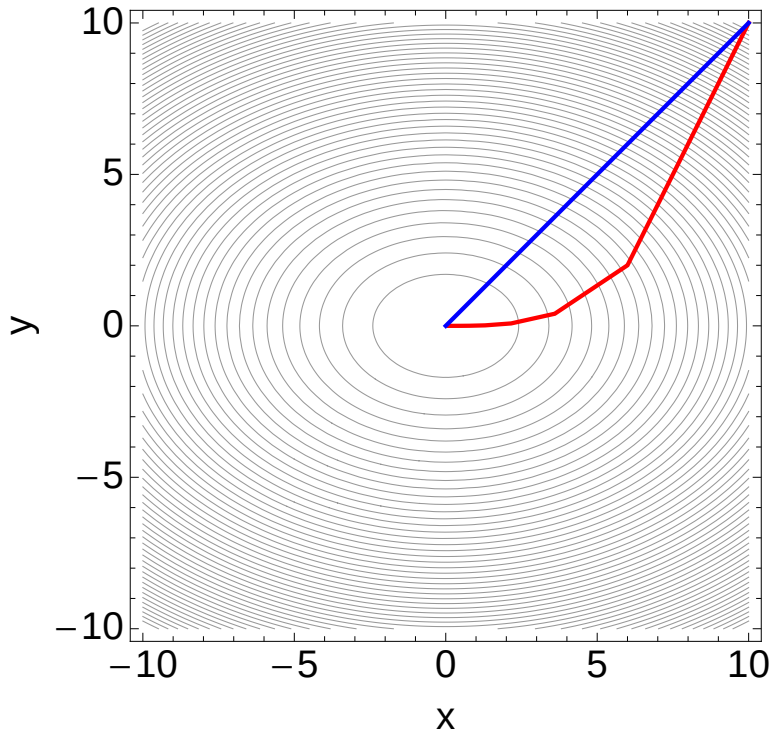

Figure 2.2: Plots showing the path of convergence for both gradient descent (Red) and Newton's method (Blue) for the function $f\left(x,y\right)=x^2+2y^2$.

$f(\boldsymbol{x}_{i+1}) < f(\boldsymbol{x}_i)$. Newton's method refines this approach to find a "steeper" path to follow for quicker convergence. Figure 2.2 shows the path taken by the gradient descent (Red Line) and Newton's method (Blue Line) for the function $f\left(x,y\right)=x^2+2y^2$. Newton's method takes one step while the gradient descent took ten.

Starting at an initial point $\boldsymbol{x}_0$ the function 2.10 can be minimized iteratively until the function is below a given threshold value. At each iteration $\boldsymbol{x}_i$, the next value is found by

$$\boldsymbol{x}_{i+1}=\boldsymbol{x}_i-\gamma\left[Hf\left(\boldsymbol{x}_i\right)\right]^{-1}\nabla f\left(\boldsymbol{x}_i\right) \tag{2.11}$$

where $[Hf(\boldsymbol{x})]^{-1}$ is the inverse of the Hessian matrix. The Hessian matrix is a matrix of second derivatives of the objective function. For this system the Hessian matrix becomes

$$Hf(\boldsymbol{x}_i) = \begin{pmatrix} \frac{\partial^2}{\partial s^2} f(s,u) & \frac{\partial}{\partial s}\frac{\partial}{\partial u} f(s,u) \\ \frac{\partial}{\partial s}\frac{\partial}{\partial u} f(s,u) & \frac{\partial^2}{\partial u^2} f(s,u) \end{pmatrix} \tag{2.12}$$

where $f(s,u)$ is the function to be minimized. The value of γ is initially chosen to be one, but subject to the Wolfe conditions[40] which means that at each iteration, γ is chosen so that $f(\boldsymbol{x}_{i+1}) < f(\boldsymbol{x}_i)$. If a value of γ cannot be found to meet this condition, the function has failed to converge. In Figure 2.2, $\gamma = 1$ for Newton's method and $\gamma = 0.2$ for the gradient descent to insure convergence. Once the function 2.10 has dropped close to machine precision, a good enough convergence has been achieved.

Newton's method requires the computation of both the first and second derivatives of $R(s,u)$ and $Z(s,u)$. Partial derivatives of $R(s,u)$ and $Z(s,u)$ with respect to u can be performed analytically. However, partial derivatives with respect to the s coordinate must be interpolated. As such, a cubic spline interpolation[40] was chosen. This type of interpolation provides continuous and smooth function and first derivative and a continuous second derivative. Interpolated points are mirrored about the $s = 0$ point to ensure that the first derivatives are zero at that point.

2.2.3 Runge-Kutta

The equations of motion of the particles can be defined as,

$$\dot{\boldsymbol{v}} = \boldsymbol{F}(\boldsymbol{x}, \boldsymbol{v}, t) \tag{2.13}$$

$$\dot{\boldsymbol{x}} = \boldsymbol{v} \tag{2.14}$$

where $\boldsymbol{v}$ is the velocity and $\boldsymbol{F}(\boldsymbol{x}, \boldsymbol{v}, t)$ is the net force acting on a particle. To solve this system of differential equations, the particle code uses a fourth order Runge-Kutta[40] (RK4) method. At each

time step

$$\boldsymbol{v}_{i+1} = \boldsymbol{v}_i + \frac{1}{6}\left(\boldsymbol{k}_1 + 2\left(\boldsymbol{k}_2 + \boldsymbol{k}_3\right) + \boldsymbol{k}_4\right) \tag{2.15}$$

$$\boldsymbol{x}_{i+1} = \boldsymbol{x}_i + \frac{1}{6}\left(\boldsymbol{l}_1 + 2\left(\boldsymbol{l}_2 + \boldsymbol{l}_3\right) + \boldsymbol{l}_4\right) \tag{2.16}$$

where the coefficients are defined by

$$\boldsymbol{k}_1 = \frac{1}{m}\boldsymbol{F}\left(\boldsymbol{x}_i, \boldsymbol{v}_i, t\right) dt \tag{2.17a}$$

$$\boldsymbol{k}_2 = \frac{1}{m}\boldsymbol{F}\left(\boldsymbol{x}_i + \frac{1}{2}\boldsymbol{l}_1, \boldsymbol{v}_i + \frac{1}{2}\boldsymbol{k}_1, t + \frac{1}{2}dt\right) dt \tag{2.17b}$$

$$\boldsymbol{k}_3 = \frac{1}{m}\boldsymbol{F}\left(\boldsymbol{x}_i + \frac{1}{2}\boldsymbol{l}_2, \boldsymbol{v}_i + \frac{1}{2}\boldsymbol{k}_2, t + \frac{1}{2}dt\right) dt \tag{2.17c}$$

$$\boldsymbol{k}_4 = \frac{1}{m}\boldsymbol{F}\left(\boldsymbol{x}_i + \boldsymbol{l}_3, \boldsymbol{v}_i + \boldsymbol{k}_3, t + dt\right) dt \tag{2.17d}$$

$$\boldsymbol{l}_1 = \boldsymbol{v}_i dt \tag{2.18a}$$

$$\boldsymbol{l}_2 = \left(\boldsymbol{v}_i + \frac{1}{2}\boldsymbol{k}_1\right) dt \tag{2.18b}$$

$$\boldsymbol{l}_3 = \left(\boldsymbol{v}_i + \frac{1}{2}\boldsymbol{k}_2\right) dt \tag{2.18c}$$

$$\boldsymbol{l}_4 = \left(\boldsymbol{v}_i + \boldsymbol{k}_3\right) dt \tag{2.18d}$$

and m is the particle mass. These coefficients act as sub steps at each time step dt and help correct for computational errors. The time step is adapted at each calculation step to be $\frac{1}{10}$ the gyro period of the particle. This allows accurate modeling of the full gyromotion at all places within the magnetic field.

2.2.4 Forces

This code has been architected using the same modular force model as the Auburn University DEMON code[41]. This modularity allows the creation of new forces without altering the underlying

solvers. The modularity is achieved by using object oriented programing techniques. A generic force class defines an interface that all forces conform to. The RK4 algorithm, acts on this generic force interface so the specifics of a particular force are hidden.

Each force is created as a subclass of the force class. Each specific force is responsible for adding its contribution to the total force acting on a particle for a particular RK4 sub step. Extra code associated with a particular force maybe add however that will have no affect or will be hidden from the RK4 solver. Various forces acting on the particles in CTH are, the Lorentz force contribution of the magnetic field and the force contribution of the electric field. Density gradient effects cannot be modeled because, diamagnetic drifts are not guiding center drifts.

Magnetic Force

The magnetic force acting on a charged particle is defined as

$$\boldsymbol{F}_m(\boldsymbol{v}) = q\boldsymbol{v} \times \boldsymbol{B} \tag{2.19}$$

where q is the net charge of a particle. The magnetic field vector is obtained at a specified (s, u, v) position in the form of equation 2.5 and transformed into the laboratory frame. This force provides the primary mechanism of gyromotion of the particle.

As shown in Section 1.2.1, the toroidal geometry of the device contributes to vertical drifts of particles. In addition the magnetic field structure in CTH is highly nonuniform. The helical winding of the magnet coils leads to troughs and peaks in the magnetic field strength. These localized magnetic wells can trap particles as they mirror back and forth between the peaks. This trapping along with a previously mentioned particle drifts will cause the particles to eventually drift out of the core plasma.

In Figure 2.3, the trajectory of a single particle started from $s = 0.5, u = 0, v = \pi$ (mid-plane of a side port on the CTH device) is plotted. The particle is launched with an initial velocity of $\boldsymbol{v} = 1000\hat{\boldsymbol{z}}\frac{\mathrm{m}}{\mathrm{s}}$. The $s = 0.5$ flux surface is also plotted with the colors representing the magnitude

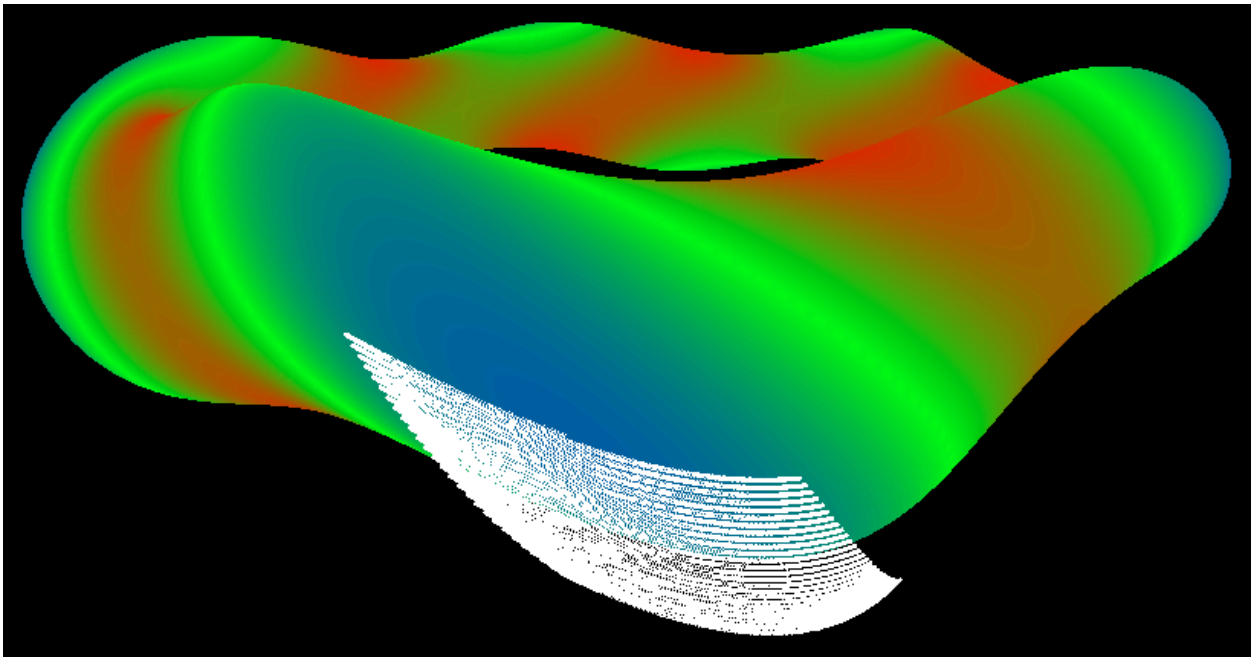

Figure 2.3: Single particle trajectory magnetic field only. Red: $|\boldsymbol{B}| = 0.75$ T, Green: $|\boldsymbol{B}| = 0.5$ T, Blue: $|\boldsymbol{B}| = 0.25$ T. Initial particle position $s = 0.5, u = 0, v = \pi$. $\boldsymbol{v}_0 = 1000\frac{\text{m}}{\text{s}}\hat{\boldsymbol{z}}$. The flux surface plotted is the $s = 0.5$ surface.

of the magnetic field strength $|\boldsymbol{B}|$. Blue represents weak magnetic field strengths $|\boldsymbol{B}| = 0.25$ T. Red represents strong magnetic field strengths $|\boldsymbol{B}| = 0.75$ T with green in between. Figure 2.3 shows the particle trapped in one of the mirror fields of CTH. The curvature and gradient drifts cause the particle to leave the $s = 0.5$ surface and eventually drift beyond the LCFS.

Electric Forces

At the beginning of this chapter, plasma potential was assumed to be constant on a surface of magnetic flux. Using this assumption, electric field forces are defined to be

$$\boldsymbol{F}_E = qE_s(s)\,\boldsymbol{e}^s = -q\frac{\partial}{\partial s}\Phi_p(s)\,\boldsymbol{e}^s \tag{2.20}$$

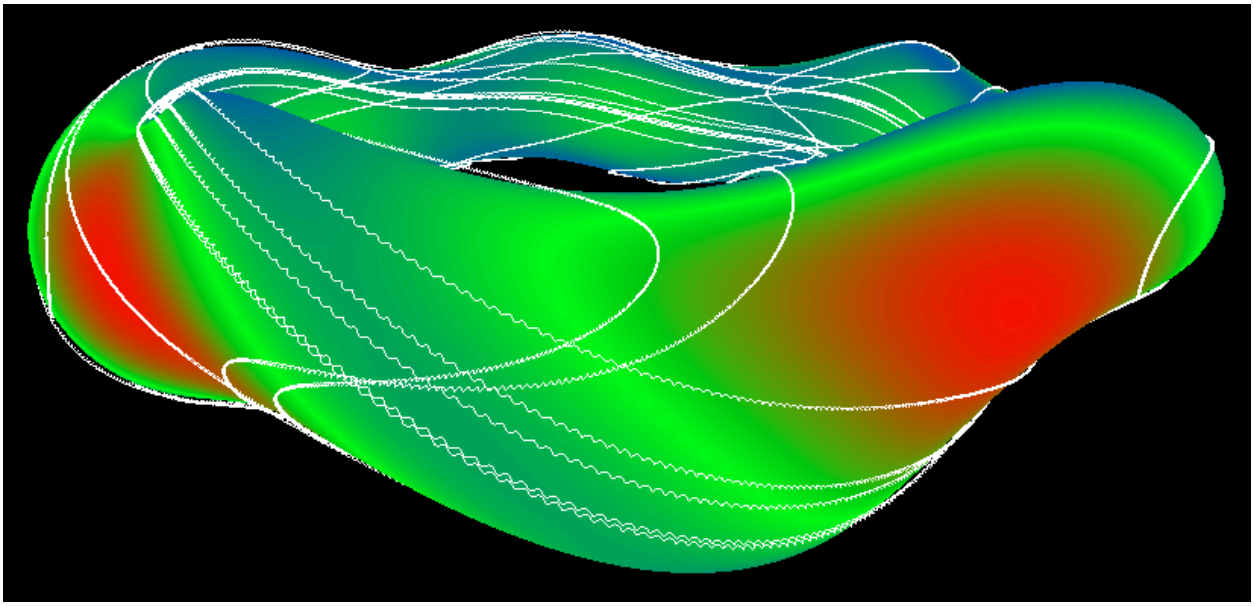

Figure 2.4: Single particle trajectory with $E_s = 10$. Red: $|\boldsymbol{E}| = 200\frac{\mathrm{V}}{\mathrm{m}}$, Green: $|\boldsymbol{E}| = 112.5\frac{\mathrm{V}}{\mathrm{m}}$, Blue: $|\boldsymbol{E}| = 25\frac{\mathrm{V}}{\mathrm{m}}$. Initial particle position $s = 0.5, u = 0, v = \pi$. $\boldsymbol{v}_0 = 1000\frac{\mathrm{m}}{\mathrm{s}}\hat{\boldsymbol{z}}$. The flux surface plotted is the $s = 0.5$ surface.

where q is the particle charge. Electric forces are defined either by defining a functional form of $E_s(s)$ directly or by spline interpolating Φ_p profiles from probe measurements. While pressure gradients were also assumed to be constant on a surface of magnetic flux, drifts arising from pressure gradients cannot be simulated in a single particle code as these are fluid drifts and do not change the guiding center motion.

In Figure 2.4, the trajectory of a single particle started from $s = 0.5, u = 0, v = \pi$ is plotted in the same manner as Figure 2.3 with the addition of a uniform $E_s\boldsymbol{e}^s$. Again the particle is launched with an initial velocity of $\boldsymbol{v} = 1000\hat{\boldsymbol{z}}\frac{\mathrm{m}}{\mathrm{s}}$. The $s = 0.5$ flux surface is also plotted with colors representing the $|\boldsymbol{E}|$. Blue represents weak electric field strengths $|\boldsymbol{E}| = 25\frac{\mathrm{V}}{\mathrm{m}}$. Red represents strong electric field strengths $|\boldsymbol{E}| = 200\frac{\mathrm{V}}{\mathrm{m}}$ with green in between. Figure 2.4 shows that the particle remains confined to a particular flux surface. Also the particle is no longer trapped in the mirror fields.

Plasma parameter profile measurements may also be used to define the electric field. From measured profiles of Φ_p or Φ_f, data positions are transformed into (s, u, v) coordinates. Again

assuming that a flux surface is an electric equipotential, a spline interpolation is used to fit the data points as a function of s. The profile is constrained to be symmetric about the magnetic axis. This insures that the electric field drops to zero at the magnetic axis. Electric fields can be transformed back into the laboratory frame at any position within the last closed flux surface. By measuring the potential profiles at any place, the electric field structure can be determined everywhere.

Simulation Results

The effect that electric fields and induced poloidal drifts is immediately apparent. In the pure magnetic field only simulations, particles remained trapped within the magnetic wells. These trapped particles eventually drift out of the plasma by a combination of gradient and curvature drifts (Equations 1.6 and 1.7).

Under the influence of an electric field, the induced poloidal drift moves the particle to the inboard side of the magnetic field where the gradient and curvature drifts push the particle back onto a magnetic surface. As a result, the particle remains confined within the plasma. The electric field also allows the particle to escape from the mirror traps between the high field regions.

These simulations can only provide a single particle view of the plasma. Collective fluid effects such as viscosity, diamagnetic drifts and plasma fluctuations, cannot be modeled in a single particle code. However this code is useful for providing insights into the complex motions of particles in the three dimensional fields.

2.3 Fluctuating Flows

When electric fields and pressure gradients are spatially inhomogeneous, a nonuniform or sheared flows can arise. In Section 1.4, sheared flows were discussed as having different effects on the stability of the plasma depending on the plasma environment. In fusion plasmas, radially inward (negative) electric fields produce sheared flows that reduce particle losses and damp large scale plasma fluctuations. In space plasmas, the presence of sheared flows is a source of free energy that can drive a wide range of plasma instabilities.

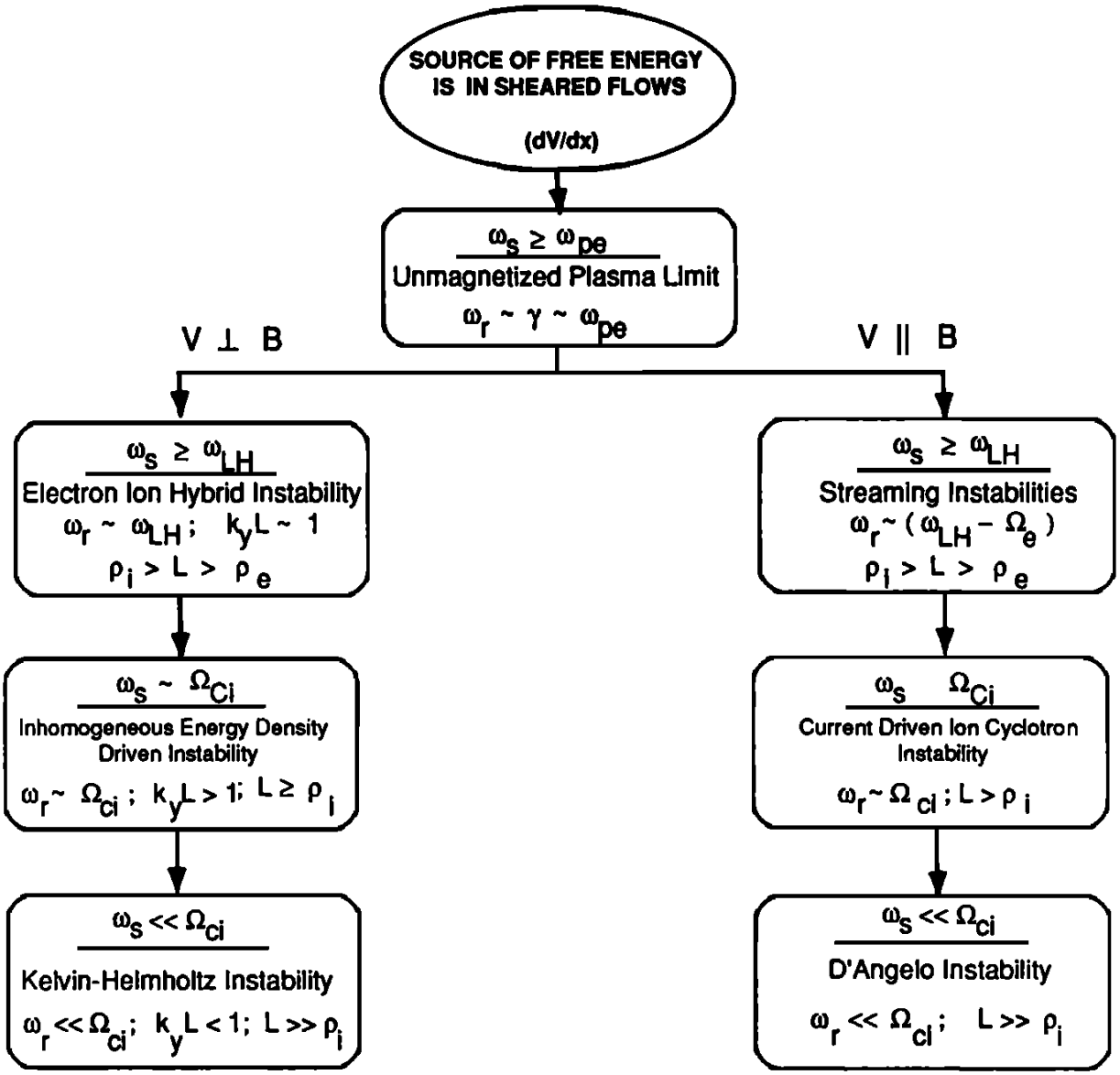

Figure 2.5: Hierarchy of plasma instabilities driven by sheared flows[30].

Studying the effects of sheared flows in plasmas is a multifaceted problem. Figure 2.5, taken from Ganguli et. al.[30], shows a hierarchy of plasma instabilities that can be driven by sheared flows. This hierarchy is divided into two main branches, shear in flows parallel to magnetic field lines and shear in flows perpendicular to magnetic field lines. These two branches can further be subdivided up based on the size of shear layer.

An exhaustive study of all possible instability regimes is beyond the scope of this dissertation. However, as a demonstration of the effects sheared flows play in the stability or instability of the plasma, an instability in a regime relevant to CTH plasma conditions will be discussed. For CTH magnetic field strengths and ion species, the ion Larmor radius (Equation 1.5) is sub-millimeter sized. Measurements of plasma potential gradients in Section 4.2, will show that CTH electric field are on the order of a few centimeters. This places the CTH relevant conditions at the bottom of both branches of Figure 2.5, where $L \gg \rho_i$.

In Sections 2.1 and 2.2.4, electric fields were assumed to point normal to the magnetic surfaces. In Section 2.1, it was shown how this transverse electric field can drive a perpendicular flow. Assuming that electric fields are normal to a magnetic flux surface and that induced flows are perpendicular to a field line, it is assumed sheared flows arising in the CTH plasma will be perpendicular to magnetic field. Derivations of electric field based on the constancy of plasma potential on a flux surface to be discussed in Section 3.5.2 verifies the validity of the first assumption. Furthermore, measurements of perpendicular flow which will be presented in Section 4.3 show the presence of perpendicular shear in the CTH plasma.

Exploring the CTH relevant scales sizes reduces the hierarchy of CTH relevant plasma instabilities to the Kelvin-Helmholtz region of Figure 2.5. Therefore, to proceed, it will be assumed that Kelvin-Helmholtz instabilities may arise in CTH plasmas. The dispersion relation of this instability will be derived and solved for various shear flow profiles. Due to nonlinear effects of the toroidal geometry, derivations of plasma instabilities will be carried out in Cartesian coordinates for simplicity.

2.3.1 Kelvin-Helmholtz

The derivation of the Kelvin-Helmholtz dispersion relation presented here follows the work presented in Guzdar et. al.[57]. The derivation will be begin by assuming a uniform magnetic field pointing in the $\boldsymbol{B} = B_0\hat{\boldsymbol{z}}$ direction. The zeroth order electric field is assumed to be a function of x pointing in the $\boldsymbol{E}_0(x) = E_0(x)\,\hat{\boldsymbol{x}}$ direction. From the E-cross-B drift (Equation 2.1), a flow perpendicular to the magnetic field is produced.

$$\boldsymbol{V}_0(x) = -\frac{E_0(x)}{B_0}\hat{\boldsymbol{y}} \tag{2.21}$$

Fluctuating quantities are assumed to take the form of a zeroth order component and a fluctuating component $p = p_0 + p_1(x)\exp[i(ky - \omega t)]$. Parallel wave propagation is assumed to be large wavelength and neglected ($k_\parallel = 0$). Zeroth order plasma density will be assumed to uniform and quasi-neutral such that $n_e \cong n_i = n$. With these assumption the ion momentum equation is

$$\left(\frac{\partial}{\partial t} + \boldsymbol{V}_i \cdot \nabla\right)\boldsymbol{V}_i = \frac{e}{m_i}\left(\boldsymbol{E} + \boldsymbol{V}_i \times \boldsymbol{B}\right) \tag{2.22}$$

assuming the following forms

$$\boldsymbol{B} = B_0\hat{\boldsymbol{z}} \tag{2.23a}$$

$$\boldsymbol{E} = E_0(x)\,\hat{\boldsymbol{x}} - \nabla\Phi(x)\exp[i(ky - \omega t)] \tag{2.23b}$$

$$\boldsymbol{V} = V_0(x)\,\hat{\boldsymbol{y}} + \boldsymbol{V}_1(x)\exp[i(ky - \omega t)] \tag{2.23c}$$

$$n = n_0 + n_1(x)\exp[i(ky - \omega t)] \tag{2.23d}$$

Substituting the zeroth order solutions and the form given in Equation 2.23 into Equation 2.22 and keeping only the first order terms, the first order ion flows can be solved for assuming $\omega \ll \Omega_{ci}$.

$$V_{i1x}(x) = -i\frac{k\Phi_1(x) - \omega'\frac{\partial}{\partial x}\Phi_1(x)}{B_0\left[1 + \frac{\frac{\partial}{\partial x}V_0(x)}{\Omega_{ci}}\right]} \tag{2.24a}$$

$$V_{i1y}(x) = \frac{\left[\left(1 + \frac{\frac{\partial}{\partial x}V_0(x)}{\Omega_{ci}}\right)\frac{\partial}{\partial x}\Phi_1(x) - \frac{\omega'}{\Omega_{ci}}k\Phi_1(x)\right]}{B_0\left[1 + \frac{\frac{\partial}{\partial x}V_0(x)}{\Omega_{ci}}\right]} \tag{2.24b}$$

In these equations, ω' is the Doppler shifted frequency defined to be $\omega' = \omega - kV_0(x)$.

For the electrons, inertial terms are ignored and relevant equations for the fluctuating electron drift are given by,

$$V_{e1x}(x) = -ik\frac{\Phi_1(x)}{B_0} \tag{2.25a}$$

$$V_{e1y}(x) = \frac{1}{B_0}\frac{\partial}{\partial x}\Phi_1(x) \tag{2.25b}$$

These equations are combined using the density continuity equation for each species α.

$$\frac{\partial n_\alpha}{\partial t} + \nabla \cdot n_\alpha \boldsymbol{V} = 0 \tag{2.26}$$

Keeping up to only first order terms, solving for the density gives

$$i\omega'\frac{n_{\alpha 1}(x)}{n_{\alpha 0}} = \frac{\partial}{\partial x}V_{\alpha 1x}(x) + ikV_{\alpha 1y}(x) \tag{2.27}$$

Equations 2.24 and 2.25 are substituted into Equation 2.27 for each species. These equations are combined assuming quasi-neutrality. Combining terms of $\Phi_1(x)$, and assuming that the shearing rate is small compared to the ion cyclotron frequency, $\frac{\partial}{\partial x}V_0(x) \ll \Omega_{ci}$, the differential form of the Kelvin-Helmholtz instability is obtained.

$$\frac{\partial^2}{\partial x^2}\Phi_1(x) - \left[k^2 - \frac{k\frac{\partial^2}{\partial x^2}V_0(x)}{\omega - kV_0(x)}\right]\Phi_1(x) = 0 \tag{2.28}$$

To explore the effects of plasma stability under the effects of sheared flows, flow profiles will be assumed to take a functional form of

$$V_0(x) = V_0 \cdot f\left(\frac{x}{L}\right) \tag{2.29}$$

where L is the scale size of the shear layer. Defining the dimensionless quantities, $\tilde{\omega} = \frac{\omega}{kV_0}$, $\tilde{x} = \frac{x}{L}$ and $\tilde{k} = kL$, Equation 2.28 becomes

$$\frac{\partial^2}{\partial \tilde{x}^2}\Phi_1(\tilde{x}) - \left[\tilde{k}^2 - \frac{\frac{\partial^2}{\partial \tilde{x}^2}f(\tilde{x})}{\tilde{\omega} - f(\tilde{x})}\right]\Phi_1(\tilde{x}) = 0 \tag{2.30}$$

This dispersion relation can solved by means of a numerical shooting code for various flow profile shapes.

Shooting Code

Consider the second order differential equation of the form;

$$\frac{\partial^2}{\partial x^2}\Phi(x) - A(\omega, \boldsymbol{k}, x)\frac{\partial}{\partial x}\Phi(x) - B(\omega, \boldsymbol{k}, x)\Phi(x) = 0 \tag{2.31}$$

This differential equation is solved numerically by guessing a solution, at large values of x. The solution is assumed to be approximated at large values of x by;

$$\Phi(x) = C_1 \exp(kx) + C_2 \exp(-kx) \tag{2.32}$$

The numerical solution of the wave function is started at a position x_{low} such that this position is well outside the wave region. In this region, the $+$ solution is asymptotically approaching zero whereas the $-$ solution approaches infinity making it unphysical. As such, the amplitude C_2 is set to be zero. The remaining amplitude, C_1, is arbitrary. Using these assumptions, the boundary conditions at x_{low} become

$$\Phi(x_{low}) = 0.1 \tag{2.33a}$$

$$\Phi'(x_{low}) = 0.1k \tag{2.33b}$$

At x_{high}, this is an unphysical, growing solution. However, for certain values of ω, the coefficient of the growing solution C_1 is zero. The exponential part of the solution is eliminated and the roots

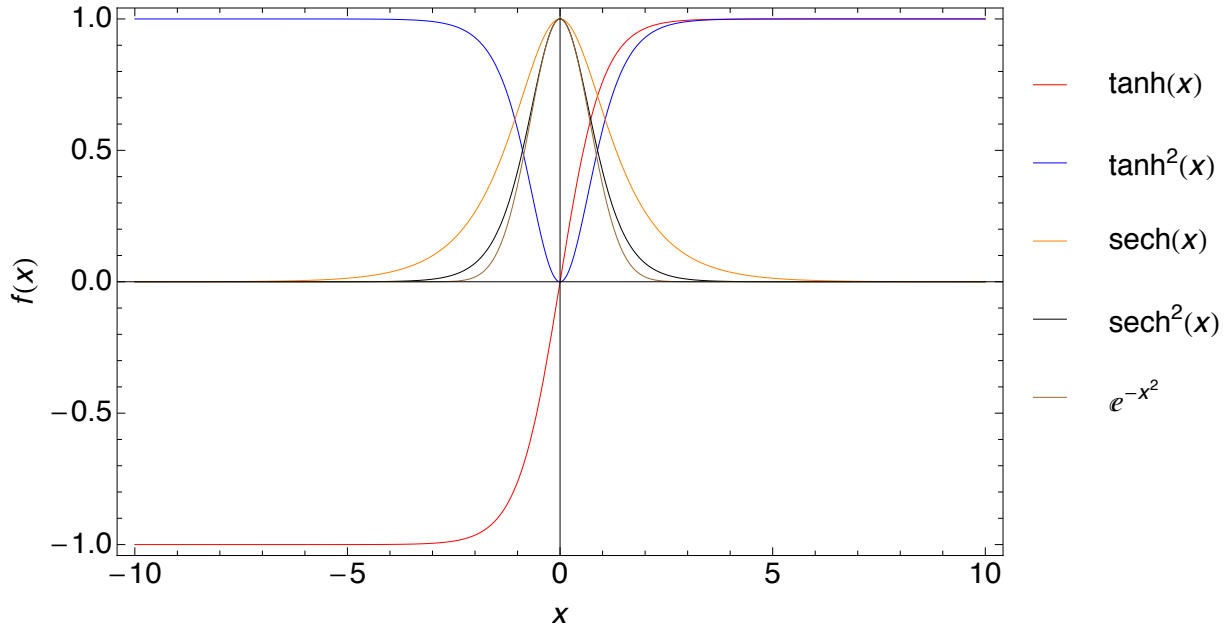

Figure 2.6: Plot of the flow profile functions.

of the equation are found from;

$$\frac{\Phi\left(x_{high}\right)}{\exp\left(kx_{high}\right)} = 0 \tag{2.34}$$

The roots of this equation are the frequency and corresponding growth rate of the instability mode. By solving this equation for ω at various values of k, the dispersion relation can be mapped out. The *Mathematica* code implementing the shooting method is found in Appendix C.1.

Numerical Results

Figure 2.6 shows the functional forms that will be used to examine the effects that flow shear has on the Kelvin-Helmholtz instability. All functional forms asymptotically approach a constant at the boundaries to ensure the shear layer is isolated in space. The $tanh$ form has the profile of two flows moving past each other. The $tanh^2$ form has the form of a stationary layer in a bulk plasma flow. By contrast, the $sech$, $sech^2$ and exp forms have a moving layer in a stationary bulk. Since the curves of these three profiles are similar, it is expected that each profile will produce a similar

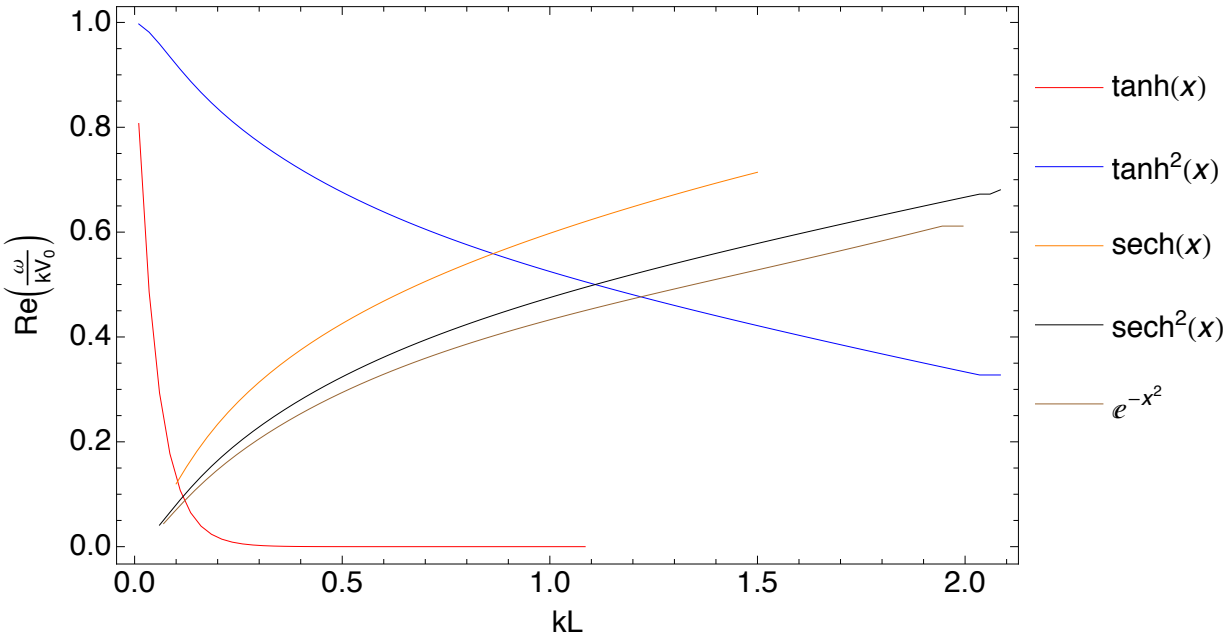

Figure 2.7: Plot of the frequency of the dispersion relation.

dispersion curve. By comparing these three similar profiles it is hoped to examine how the width of hear layer affects the mode frequency and growth rate.

Figures 2.7 and 2.8 show the frequency and growth rate dispersion relations. For all flow profiles, there is a region of instability growth. The shape and size of the shear layer determines the width of the instability region. As expected, the growth rate and frequency curves for the $sech$, $sech^2$ and exp forms take a similar shape. For these three profile forms, the wider the shear layer, the smaller the instability growth. The flow profiles for the $tanh^2$ and $sech^2$ are inverted with respect to each other yet their growth rate curves are the exact same. This suggests that it is the scale size of the shear layer that determines the growth of the Kelvin-Helmholtz instability. However, the frequency curves, of two cases, are vastly different. For the $tanh^2$ profile, there is a bulk flow with the shear produced by a stationary region in the center. For this shear profile, high frequencies are associated with long wavelengths. By contrast, for the $sech^2$ profile, the opposite is produces. The bulk is stationary and the with the shear produced by a flowing region in the center. For this profile, high frequencies are associated with short wavelengths.

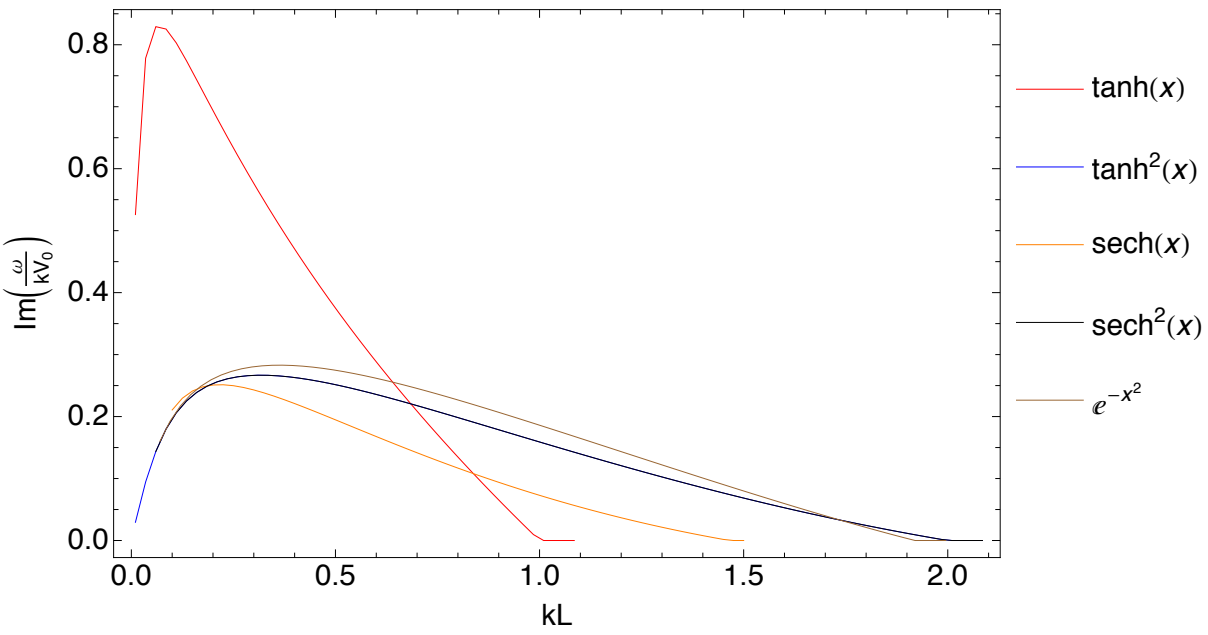

Figure 2.8: Plot of the growth rate of the dispersion relation.

This demonstrates some of the effects that sheared flows have on the stability of the plasma. However, this is only a small corner in the vast region of plasma instabilities. Other shear driven instabilities may have different responses to the various scale lengths and shear profiles. Furthermore non-linear effect of the three dimensional plasma shape, may change the response of the plasma.

Chapter 3

Experimental Device

This chapter will provide an overview of the hardware and diagnostics used in this dissertation. An overview of the CTH device design is provided. The theory, design and operation of all major diagnostic systems used in the project will be discussed.

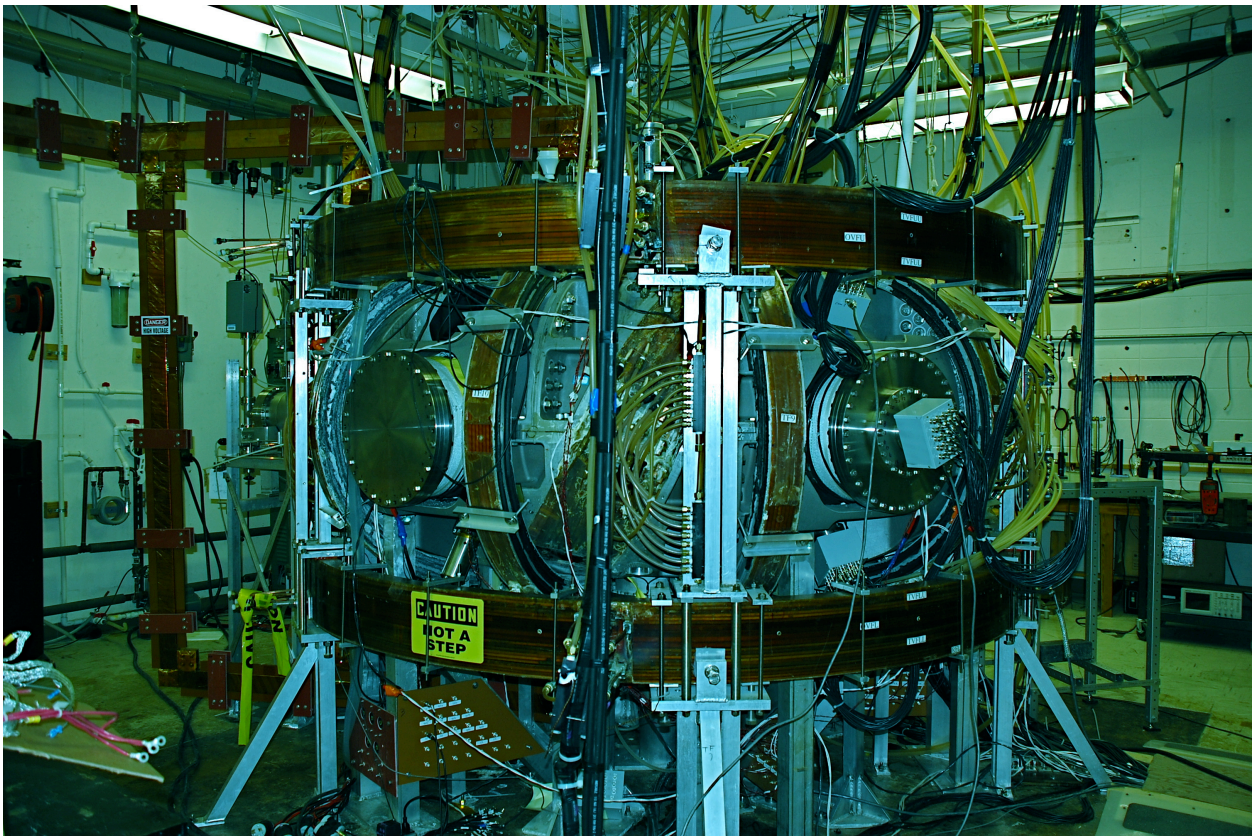

Figure 3.1: Photograph of the CTH device. The large horizontal port shown on the left side of the photo is at a toroidal angle of $\phi = 180°$. The right horizontal port is at a toroidal angle of $\phi = 252°$.

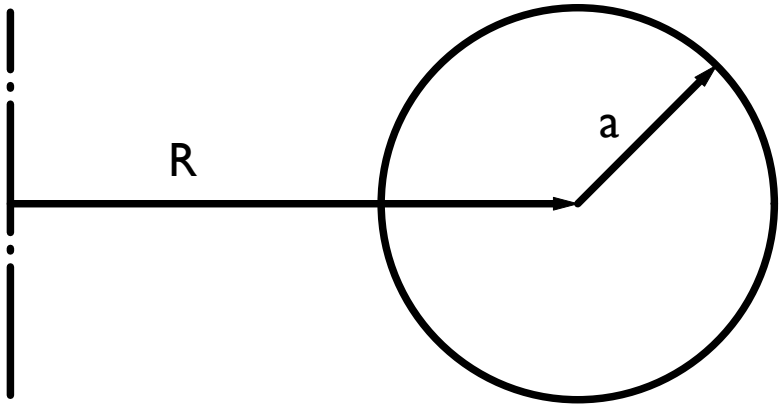

Figure 3.2: Scaled diagram of the CTH vacuum vessel cross-section of the major and minor radii.

3.1 The Compact Toroidal Hybrid

Experiments presented in this dissertation, are performed in the purely stellarator configuration of CTH; i.e., without the presence of driven plasma currents. As a result, this project made use of a subset of the CTH coil set discussed in Section 1.3.1. Specifically, only the Helical Field (HF) and Trim Vertical Field (TVF) coil sets are used; the Shaping Vertical Field (SVF), Radial Field (RF) and Error Correction Coils (ECC) were not used for this work. For each experiment discussed, the current setting for the active coils will be given.

3.1.1 Vacuum Vessel

The CTH vacuum vessel is a torus with a circular cross-section. CTH has major radius of $R = 0.75$ m and minor radius of $a = 0.26$ m. Figure 3.2 shows a scaled diagram of the CTH vacuum vessel cross-section. A feature of the magnetic field structure is the symmetry planes. These are toroidal cross-section where the magnetic flux surfaces are vertically (up-down) symmetric. Port placement on CTH is centered on these symmetry planes.

There are five, 18"-diameter ConFlat flanges mounted horizontally on the outboard side at 36° and repeating every 72° around the machine. Above and below the horizontal ports, are a pair of $4\frac{1}{2}$" ConFlat ports mounted at a 45° angle with respect to the horizontal. Five pairs of 10" ConFlat

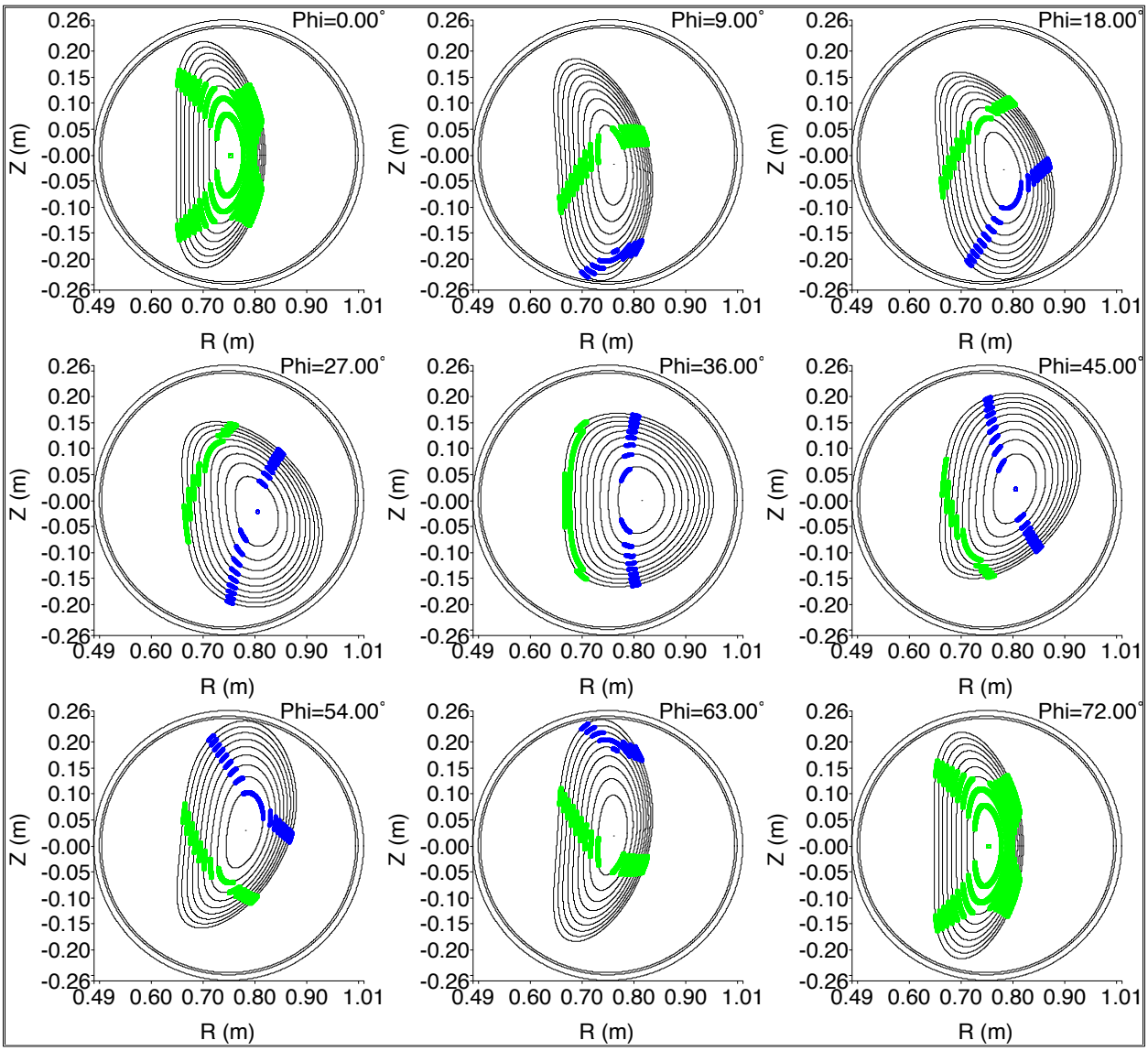

Figure 3.3: Various flux surfaces produced from the HF and TVF coils for a single field period. Symmetry planes are located at the $\phi = 0°$, $\phi = 36°$ and $\phi = 72°$. Shaded areas show the magnetic fields resonate with the ECRH heating (Green: 17.67 GHz, Blue: 14 GHz).

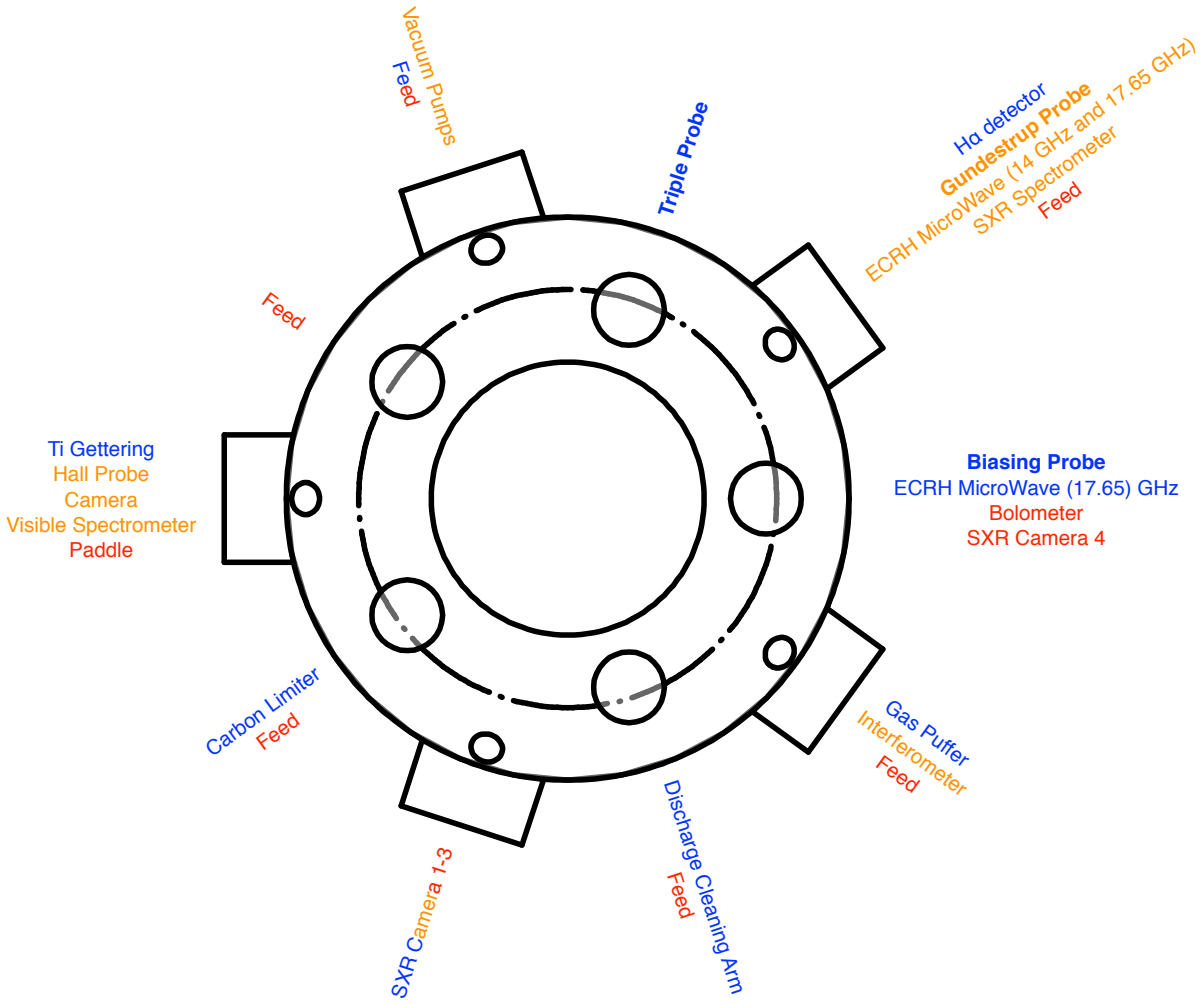

Figure 3.4: Diagram of various diagnostic and equipment locations on CTH. Blue marks the top port mounting locations. Orange marks the side port mounting locations. Blue marks the bottom port mounting locations. Diagnostics relevant to this dissertation are highlighted in bold. Diagnostics marked "Feed" are feedthrough locations for the magnetic diagnostics.

Vacuum Vessel	
Major Radius	$R_0 = 0.75$ m
Minor Radius	$a = 0.26$ m
Plasma Parameters	
Electron Temperature†	$T_e \sim 5 - 20$ eV
Electron Density†	$n_e \sim 10^{18}$ m^{-3}
Ion Cyclotron Frequency	$f_{ci} \sim 10$ MHz
Ion Plasma Frequency	$f_{pi} \sim 150$ MHz
Ion Larmor Radius†	$\rho_i \sim 0.2$ mm
Ion Species	Hydrogen
Plasma Beta†	$\beta \sim 10^{-5}$
Magnetic Field Strength	$\lvert \boldsymbol{B} \rvert \leq 0.75$ T

Table 3.1: CTH Operational Parameters

† ECRH only

vertical ports are mounted, on the top and bottom of the vacuum vessel, at a major radius of 0.71 m at $0°$ and repeating every $\Delta\phi = 72°$. Figure 3.4 shows the mounting locations of various diagnostic systems and vacuum infrastructure on CTH. The CTH vacuum vessel is a continuously conducting shell made of Inconel 625 alloy with a low toroidal resistance. For this work, since, plasmas were operated without induced plasma current, vacuum vessel currents and induced plasma current will be assumed to be negligible.

3.1.2 Plasma Heating

The plasma is generated using three Electron Cyclotron Resonance Heating (ECRH) microwave sources providing up to 10 kW each. Two sources provide heating power at 14 GHz resonant with 0.5 T magnetic fields. One source provides power at 17.67 GHz resonant with 0.64 T. Figure 3.3 shows the resonant fields at various cross-sections around CTH. The green areas represent the 17.67 GHz resonance and the blue areas represent the 14 GHz resonance. ECRH plasmas have a maximum cutoff density $\sim 4 \times 10^{18}$ m^{-3}. Table 3.1 shows various plasma parameters under ECRH heating.

3.2 Data Acquisition and Analysis

CTH data is acquired on one of two systems. The slower speed (8 kilo-samples per second) SCXI and the higher speed (100 kilo-samples per second) DTAC systems. All of the raw data from the diagnostics is stored in an `mdsplus`[42] data base, a standard fusion data storage system developed at MIT and used through out the fusion community. The raw data is stored in 16 bits and is covered to mV by a conversion factor of 0.305185. CTH run parameters are also stored such as timing for the ECRH supplies and the timing information for each of the data acquisition boards. In this dissertation, ECRH drive times are used to crop acquired data down to a time interval when the plasma is present in the CTH device.

For the majority of the experiments described in this work, measurements are made by moving the diagnostic probes, typically in 1 cm intervals, across the plasmas, as described in Chapter 2. Each position corresponds to a single plasma discharge or "shot". Shots on CTH are repeated with a repetition rate of approximate one shot every $5-6$ min. A full data set typically consists of about 16 spatial positions.

During a single shot, a time series of voltage and current measurements are made. Depending on the particular experiment being performed, the time series data is divided into subsections and averaged. In this dissertation, time intervals chosen are typically specified by the ECRH drive or a chosen biasing interval. Error in measurements is accounted for by calculating the standard deviation[43] of the data within the chosen time interval.

$$\sigma^2 = \frac{1}{n}\sum_{i}^{n}(x_i - \mu) \tag{3.1}$$

Here μ is the mean of the collected data. After each shot, the probe is moved and this procedure is repeated until the desired depth is reached.

3.3 Limiters

The edge of the CTH plasma is defined by a various limiters throughout the vacuum vessel. These limiters define the boundary between the open field lines and the scrape off layer known as the last closed flux surface (LCFS). The other function they serve is to protect the vacuum vessel and prevent damage to any equipment inside the vacuum vessel. Each limiter is electrically connected to the vacuum vessel. During normal operation, the vacuum vessel is grounded.

CTH has four permanent limiters. Two limiters have a minor radius of 0.26 m. One is made of molybdenum mounted at $\phi = 144°$ while the other is made of stainless steel mounted at $\phi = 184°$. Two molybdenum limiter blocks with a minor radius of 0.245 m are mounted at $\phi = 300°$ and $\phi = 358°$ respectively. A moveable carbon limiter mounted at the $\phi = 216°$ can be used to adjust the size of the plasma. For this dissertation only the fixed limiters are used. The LCFS is determined from the `V3FIT` equilibrium by calculating where the innermost flux surface intersects any of the limiters.

3.3.1 Biasing Probe

In order to study the effects of edge electric fields and plasma rotation in the edge, it is necessary to control the internal electric fields of the plasma. A typical way of modifying electric fields involves either drawing current from or injecting current into the plasma. The CTH edge electric fields are modified by inserting a biased electrode past the last closed flux surface and drawing current when a bias is applied.

Design

The biasing tip is constructed of a $\frac{3}{4}''$ diameter, $1''$ long 316 alloy stainless steel cylinder welded to a $\frac{3}{8}''$ diameter shaft. A cylindrical Alumina ceramic tube placed over the shaft, insures that the probe tip is electrically isolated past the LCFS. The tip is coupled to a $\frac{1}{2}''$ diameter probe shaft mounted on a 10 cm vacuum positioner. A photograph of the assembled probe tip is shown in

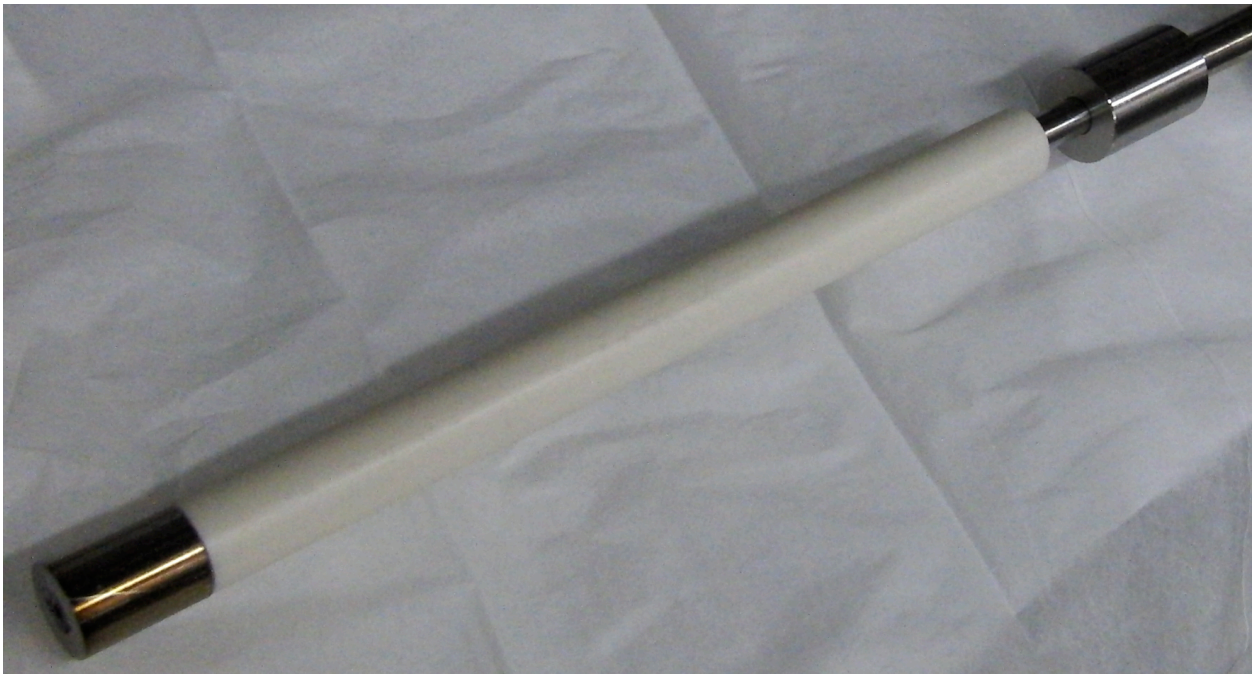

Figure 3.5: Photograph of biasing probe tip.

Figure 3.5. The probe is mounted on a vertical port just off the symmetry plane at $\phi = -3.01°$. Figure 3.6 shows a cross-sectional diagram of the mounted probe.

When not in use, the entire probe assembly is retracted from the plasma and remains behind the limiter. When operational, the conducting part of the biasing probe is extended past the last closed flux surface. The insulating ceramic portion remains behind the CTH limiters. This insures that plasma does not become electrically shorted out to the limiter. Earlier versions of the biasing probe, that used a single conducting rod, were unsuccessful at modifying the edge electric fields. The entire plasma would float up or down to the bias applied while potential profiles would remain unaltered.

Bias Circuitry

The entire biasing probe assembly is biased with respect to ground using a ± 100 V, ± 10 A Kepco bipolar power supply with a built in function generator. Figure 3.7 shows a circuit diagram of the biasing setup. The probe is electrically isolated from the vacuum vessel using a ceramic

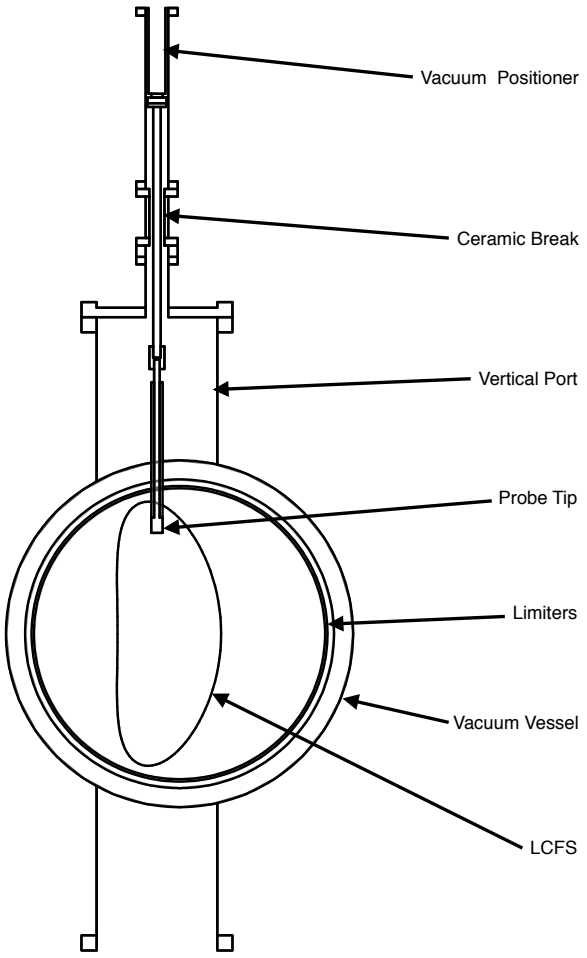

Figure 3.6: CTH cross-section of the biasing probe mounted at $\phi = -3.01°$. The probe is drawn at the full travel position.

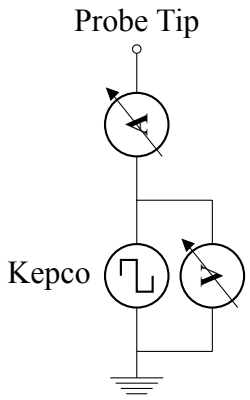

Figure 3.7: Circuit diagram for the biasing probe.

Channel	Name	Plate Designation
`ACQ1962:INPUT_47`	ED PB 1	Measured Bias Voltage
`ACQ1962:INPUT_49`	ED PB 3	Measured Bias Current

Table 3.2: The CTH `mdsplus` channels for the Biasing Probe.

break. The actual voltage applied and the current drawn by the probe are measured during the shot. Current is determined from a ± 10 V output signal from the Kepco. The voltage is determined using a fractional gain differential amplifier circuit.

In typical biasing experiments, the initial bias is held at 0 V with respect to ground. During the course of the 100 ms long shot, a pre-programmed set of voltages, in the range of ± 100 V, can be applied to the probe. Analysis of the experimental data is often performed as a comparison between the 0 V and non-zero biasing regions. A typical biasing scheme will start with a 0 V bias for 25 ms. During this time period the initial plasma is still forming. As a result, the plasma parameters are generally unstable and make a poor choice for the 0 V reference. The bias is then increased to 100 V for the next 25 ms, and decreased back down 0 V for 25 ms. Unlike the initial 0 V bias, in this time period, the plasma conditions remain relatively steady. Finally the bias is decreased to -100 V. A typical biasing waveform is shown in Figure 3.8.

Data Analysis

Raw measured voltage and current data is collected throughout the entire CTH shot on the DTAC system. Table 3.2 shows the `mdsplus` database entries for the Biasing Probe. Raw data is converted to voltage and currents by

$$V_{real} = Raw \frac{0.305185}{1000 \frac{\text{mV}}{\text{V}}} 36.66 \text{ V} + 0.61\text{V} \tag{3.2a}$$

$$I_{real} = Raw \frac{0.305185}{1000 \frac{\text{mV}}{\text{V}}} 1.3 \frac{\text{A}}{\text{V}} \tag{3.2b}$$

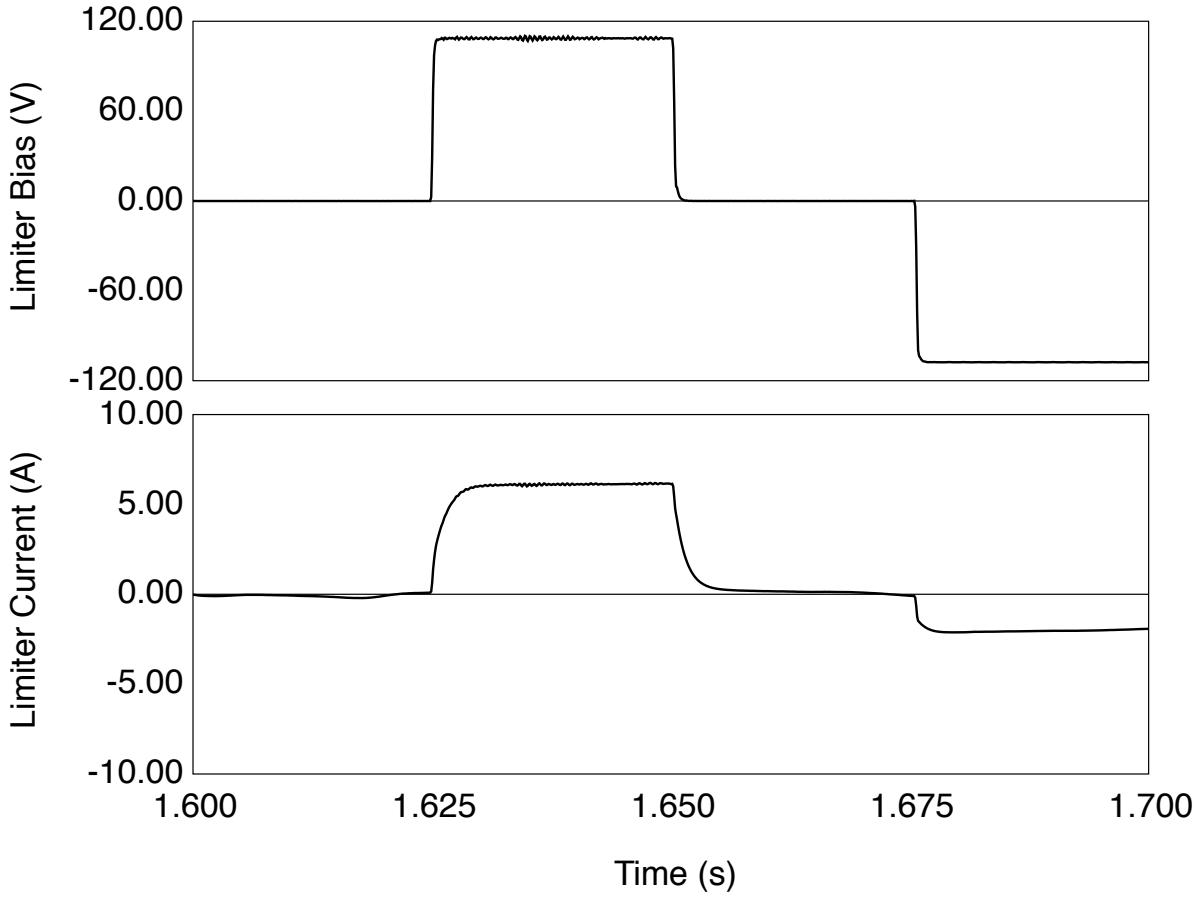

Figure 3.8: Raw voltage and current data for the biasing probe for a single shot.

It is unnecessary to zero out data on this probe because voltage offsets of the circuit are measured a priori and taken into account in Equation 3.2a. Figure 3.8 shows processed biasing probe data for a typical biasing process.

3.4 Diagnostics

CTH has an extensive array of plasma diagnostics. Figure 3.4 shows the mounting locations of various plasma diagnostics. The majority of CTH diagnostics are magnetic diagnostics. There are a wide variety of magnetic pickup coils located throughout the inside and outside of the vacuum vessel. These diagnostics detect fluctuations in the magnetic field particularly magnetohydrodynamic instabilities in the presence of plasma current. A Hall effect probe allows in-situ measurements of the non-fluctuating magnetic field. All of the magnetic diagnostic systems are discussed extensively in work by Stevenson[9]. The line averaged density is measured through the use of an interferometer. CTH also contains various hard and soft X-ray diagnostics. However in the absence of plasma current, and the low value of plasma $\beta \sim 10^{-5}$, the usefulness of these diagnostics is diminished. This dissertation will focus on measurements primarily from two, in-situ probe systems that will measure the plasma parameters and detect flows in the plasma.

Because this work relies on probe measurements taken at different locations within the CTH vacuum vessel, it is essential to have a good reconstruction of the evolution of the magnetic surfaces during each shot. This is accomplished by using the `V3FIT` equilibrium reconstruction code[38]. `V3FIT` uses the three-dimensional equilibrium code `VMEC` to reconstruct the plasma equilibrium. The calculated equilibrium is compared to plasma diagnostics and input parameters are adjusted. This procedure is repeated until the equilibrium reconstruction and plasma diagnostics agree. Reconstructed equilibria are plotted to show the size, shape and position of the plasma. This dissertation makes extensive use of reconstructed equilibrium attained from `V3FIT` to facilitate comparison of probe measurements in different areas of the plasma. A description of how this comparison is made is given in Section 3.5. As part of this research project, I was responsible for interfacing the CTH data acquisition system with the `V3FIT` code. This was achieved by building a client server system that has been successfully operating for over three years. A copy of the server source code and LabVIEW client interface is available on the CTH archive server.

3.4.1 Triple Probe

General plasma parameters are obtained by means of the instantaneous triple probe based upon the Chen and Sekiguchi design[39]. A triple probe is a three tipped Langmuir probe that uses a fixed bias. The nature of the fixed bias allows a simplified analysis, and a fast time response. In essence, this Langmuir probe technique allows real time in-situ measurements of electron temperature T_e, electron density n_e and floating potential Φ_f, and an estimation of plasma potential Φ_p. Electric fields can be estimated by taking the gradient of either the Φ_f or Φ_p profiles.

Theory

The current flowing through any biased Langmuir probe can be written as the sum of the electron and ion current as follows:[39]

$$I_n = I_e \exp\left[\frac{e}{k_b T_e}\left(\Phi_n - \Phi_p\right)\right] - I_{sat} \tag{3.3}$$

where k_b is Boltzmann's constant, T_e is the electron temperature and Φ_p is the plasma space potential or plasma potential. The total current flowing through a probe tip n is the combined current contribution from the electrons I_e, scaled by the probe tip bias potential Φ_n, and the contribution from the ion saturation current I_{sat}. Unbiased, each probe tip, when isolated from ground, will charge to the floating potential Φ_f and no net current will be collected by the probe.

The triple probe is arranged such that one tip (probe tip 2) remains electrically floating. Therefor, Equation 3.3 as applied to probe tip 2 becomes

$$I_e \exp\left(-\frac{e}{k_b T_e}\Phi_p\right) = I_{sat} \exp\left(-\frac{e}{k_b T_e}\Phi_f\right) \tag{3.4}$$

A fixed bias is applied between probe tips 1 and 3 such that probe tip 1 is based positively with respect to probe tip 3. Probe tip 1 will reach some potential above Φ_f, labeled Φ_1, and starts drawing current. Since probe tip 1 is biased with respect to probe tip 3, the current entering probe tip 1 must

equal the current exiting probe tip 3. Probe tip 3 will acquire a potential lower than Φ_f, labeled Φ_3. The key criterion of the instantaneous triple probe is that the potential applied between probe tips 1 and 3 is sufficiently large to force tip 3 to remain in ion saturation. Combining Equations 3.3 and 3.4, the current flowing through probe tips 1 and 3 respectively is

$$I_1 = -I = I_{sat} \exp\left[\frac{e}{k_b T_e}\left(\Phi_1 - \Phi_f\right)\right] - I_{sat} \tag{3.5}$$

$$I_3 = I = -I_{sat} \tag{3.6}$$

where $I = -I_1 = I_3$.

Having obtained expression for the current flowing through each probe tip the various plasma parameters can be solved for. Combining Equations 3.5 and 3.6, T_e can be solved for.

$$\frac{k_b T_e}{e} = \frac{\Phi_1 - \Phi_f}{\ln(2)} \tag{3.7}$$

It should be noted that this expression is only valid when bias between probe tips 1 and 3 is sufficiently large that probe tip 3 reaches ion saturation. Placing Equation 3.7 into 3.5 and combining it with Equation 3.6, the electron density can be solved for:

$$I_{sat} = e n_e \sqrt{\frac{k_b T_e}{m_i}} \tag{3.8}$$

$$n_e = \frac{I}{eA}\sqrt{\frac{m_i}{k_b T_e}} \exp\left(\frac{1}{2}\right) \tag{3.9}$$

Here, I, is the net current flowing through probe tips 1 and 3, A is the probe tip area, and m_i is the ion mass. Combining all of these results, Equation 3.4 can be used to estimate Φ_p.

$$\Phi_p = \frac{k_b T_e}{2e}\left[\ln\left(\frac{m_i}{2\pi m_e}\right) + 1\right] + \Phi_f \tag{3.10}$$

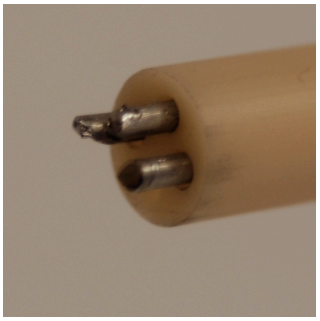

Figure 3.9: Photograph of triple probe tip.

Design

The probe tip is constructed from three, 1 mm diameter tungsten wires inserted through a four bore alumina ceramic tube. A photograph of the probe tip is shown in Figure 3.9. The ceramic tube is long enough such that the probe tips can reach to the mid-plane with any metal pieces left in the shadow of the limiter. Each probe tip is exposed $2-3$ mm. triple probe theory assumes all probe tip have equal areas so each tip is exposed the same length. The ceramic tip is coupled to a $\frac{1}{2}''$ diameter 316 alloy stainless steel probe shaft ending to an expanded $1\frac{1}{2}''$ tube with $2\frac{3}{4}''$ ConFlat vacuum flanges. Three Kapton coated ultra high vacuum (UHV) wires are connected to the tungsten wires and feed through the probe shaft. Wires connected to tips 1 and 3 are a twisted pair to avoid induced current pickup. All probe wires are connected to a three BNC vacuum feed through.

The triple probe is mounted on the center of a top vertical port at $\phi = 72°$. Figure 3.10 shows a cross-sectional diagram of the mounted probe. A $1'$ extension holds a welded bellows and probe drive away from the vacuum vessel to avoid magnetic perturbations by the electric stepper motor. A welded bellows, with a $\frac{3}{4}''$ inner diameter and a $14''$ throw, is mounted to a $20''$ travel probe drive. A stepper motor and fine threaded worm drive allows precise probe positioning within 0.005 mm. The flange that mounts the probe shaft to the bellows is rotatable allowing the probe tips to be adjusted so that no tips are shadowed in the toroidal direction. A photograph of the assembled probe drive system with probe mounted is shown in Figure 3.11. When fully retracted, the probe

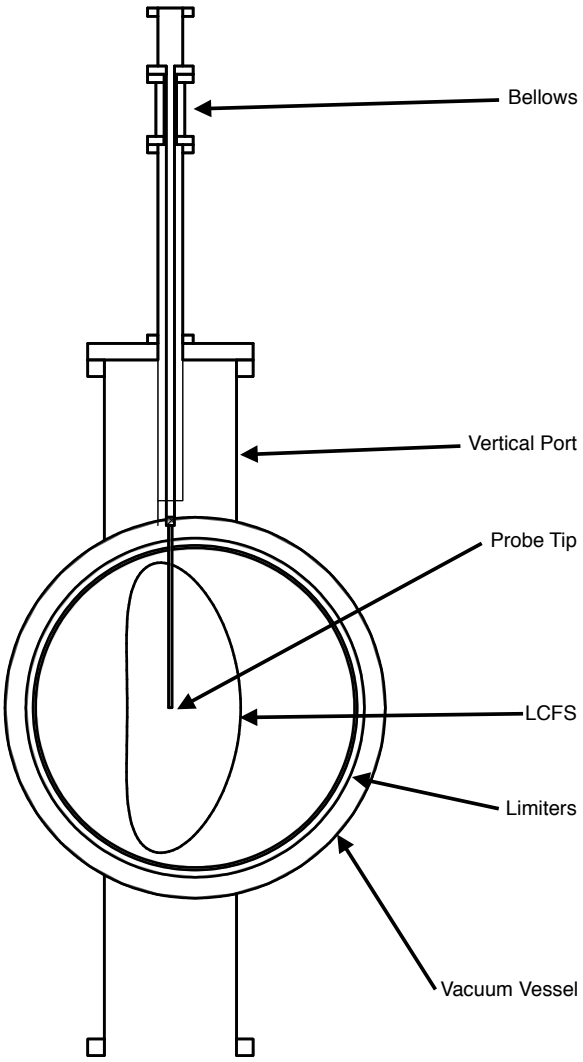

Figure 3.10: CTH cross-section of the triple probe mounted at 72°. The probe is drawn at the full travel position.

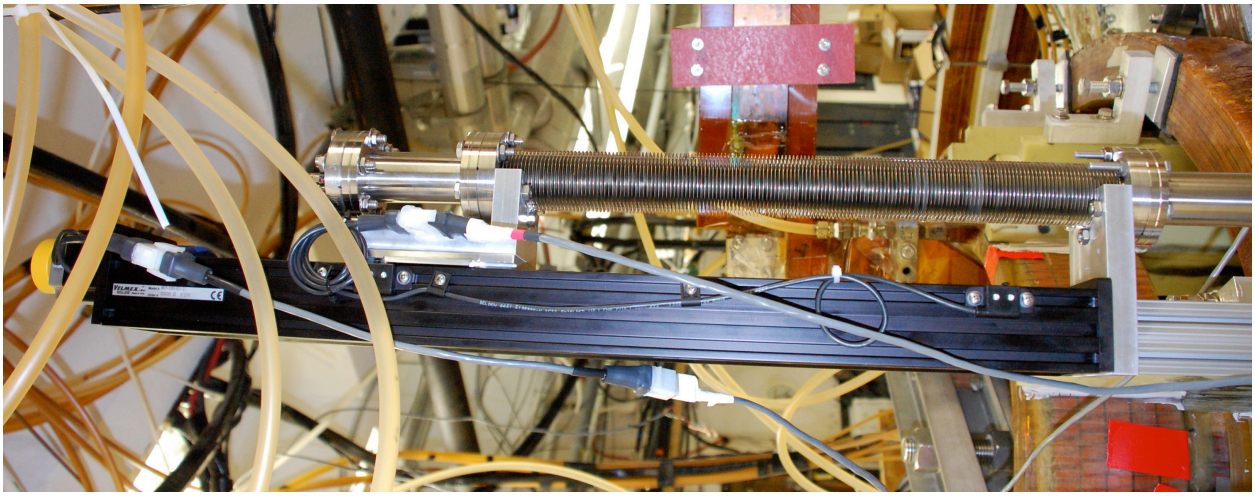

Figure 3.11: Photograph of probe drive system and bellows.

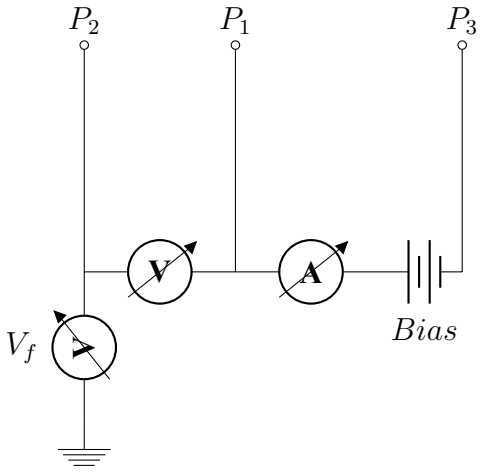

Figure 3.12: Simplified triple probe circuit diagram.

is contained within a 316 alloy stainless steel shell to prevent contamination of the tips during discharge cleaning and titanium gettering.

Measurement Circuitry

In its simplest form, all of the triple probe parameters can be obtained from three measurements. Figure 3.12 shows a simple circuit diagram for the triple probe. The potential difference

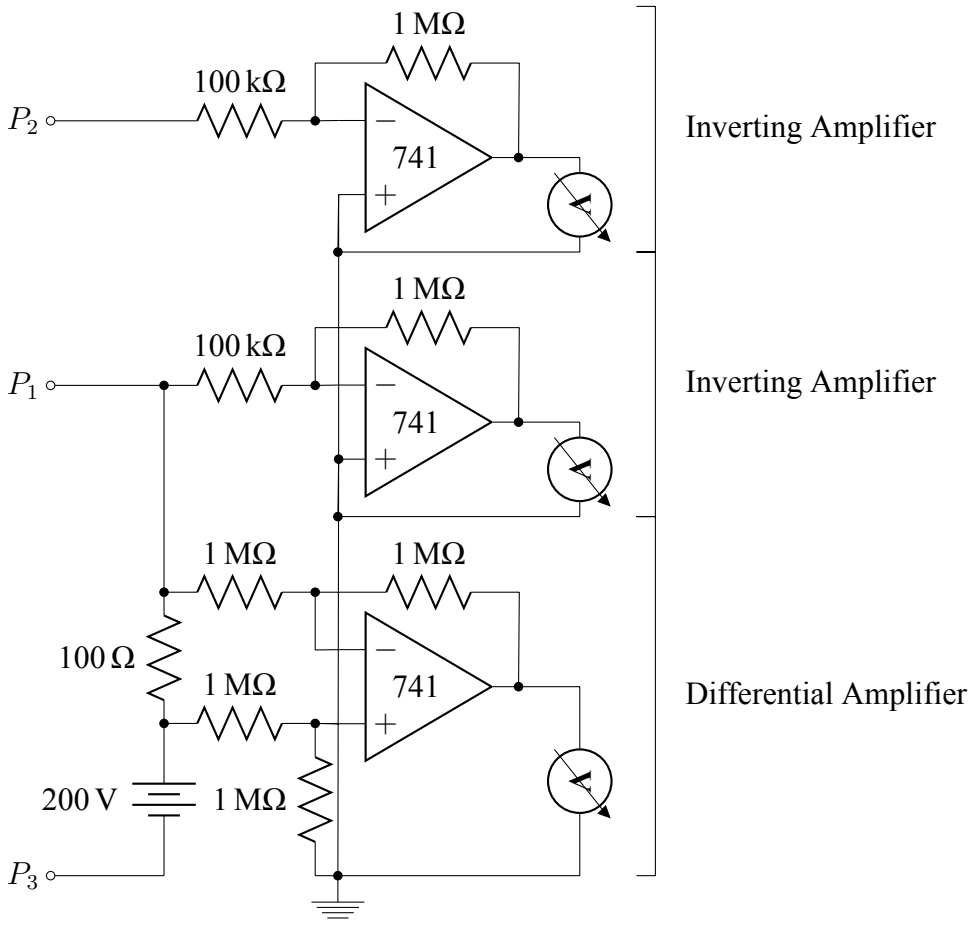

Figure 3.13: First op amp circuit for Triple Probe. This consists of two inverting amplifiers to measure potential differences, and a unity gain differential amplifier measuring the voltage drop across a shunt resistor to measure current. All op amps are powered by a ± 12 V power supply.

between probe tip P_2 and ground measures the floating potential Φ_f directly. The potential difference measured between probes tips P_1 and P_2 is related to the electron temperature T_e by Equation 3.7. The electron plasma density n_e, is determined from the current (I) flowing through probe tips P_1 and P_3 using Equation 3.9. It is important to note that this circuit does not provide a current path to ground. All three tips must remain electrically floating in order for the triple probe analysis to be performed.

To prevent a current path to ground and to provide a scaled and buffered ± 10 V signal for the DTAC cards, two op amp circuits are built. Figure 3.13 shows the circuit diagram for the first of the probe circuits. The Φ_f and the potential between P_1 and ground (Φ_1) are measured by means of a

Channel	Name	Description
`ACQ1962:INPUT_44`	MK PB 1	Φ_1
`ACQ1962:INPUT_45`	MK PB 2	Φ_f
`ACQ1962:INPUT_46`	MK PB 3	I_{sat}

Table 3.3: The CTH `mdsplus` channels for the Triple Probe.

fractional gain inverting amplifier[44]. Resistor values are chosen to provide a divide by ten scaling. The potential difference between P_2 and P_1 ($\Phi_f - \Phi_1$) is subtracted in software. Current flowing through the circuit is measured by unity gain differential amplifier[44] across a shunt resistor. A $100\ \Omega$, $75\ \Omega$ or $50\ \Omega$ shunt is used depending on plasma conditions. Differential amplifier resistors are chosen to be 1 MΩ 1% resistors. All op amps are powered by a ± 12 V power supply and are generic 741 models. While the triple probe was able to make measurements of plasma parameters during positive biasing, during negative biasing, the circuit shown in Figure 3.13 suffered from common mode rejection[44] problems.

Data Analysis

Raw potential and current data is collected throughout the entire CTH data shot on the DTAC systems. Table 3.3 shows a table of the `mdsplus` database entries for the Triple Probe. Raw data is converted to voltages and currents by

$$V_{real} = Raw * 0.305185 \frac{-Gain}{1000 \frac{\text{mV}}{\text{V}}} \tag{3.11a}$$

$$I_{real} = Raw * 0.305185 \frac{1 \times 10^7 \frac{\mu\text{A}}{\text{A}}}{1000 \frac{\text{mV}}{\text{V}} * R} \tag{3.11b}$$

where $Gain$ is the value of the signal divider and R is the value of the shunt resistor. Channels 1 and 2 are converted using Equation 3.11a. Channel 3 is converted using Equation 3.11b. Since the probe tips are electrically floating, it cannot be predetermined what values channels 1 and 2 should have when there is no plasma present. However the probe should not be drawing current when there is no plasma. In the absence of short circuits, any current offsets in the signal, when there is

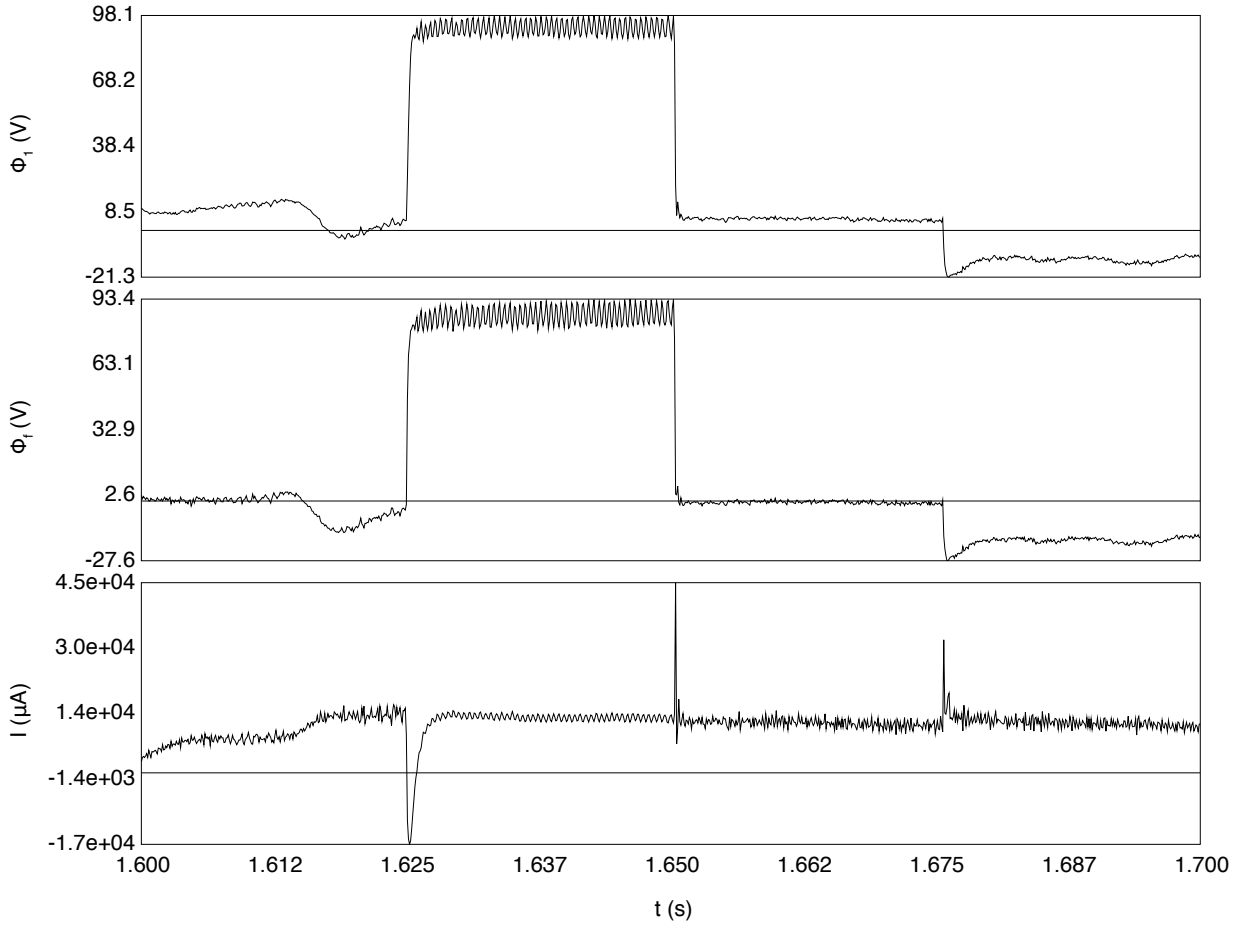

Figure 3.14: Raw voltage and current data for the triple probe for a single shot.

no plasma, should be the result potential offsets in the measurement circuits. The initial value of the current signal is measured and used to offset the total signal in software.

Figure 3.14 shows the raw voltage and current data for a single shot. The Φ_f and Φ_1 are used to calculate T_e at each data point using Equation 3.7. Data points where Φ_f is measured as a higher potential than Φ_1 calculate as a negative temperature. This can occur when the difference between Φ_f and Φ_1 are within the noise signal or when plasma parameters are rapidly changing such as during the transition between biasing regions. This occurs relatively infrequently in the regions of interest of this dissertation. As such these data points are considered invalid and removed from the analysis.

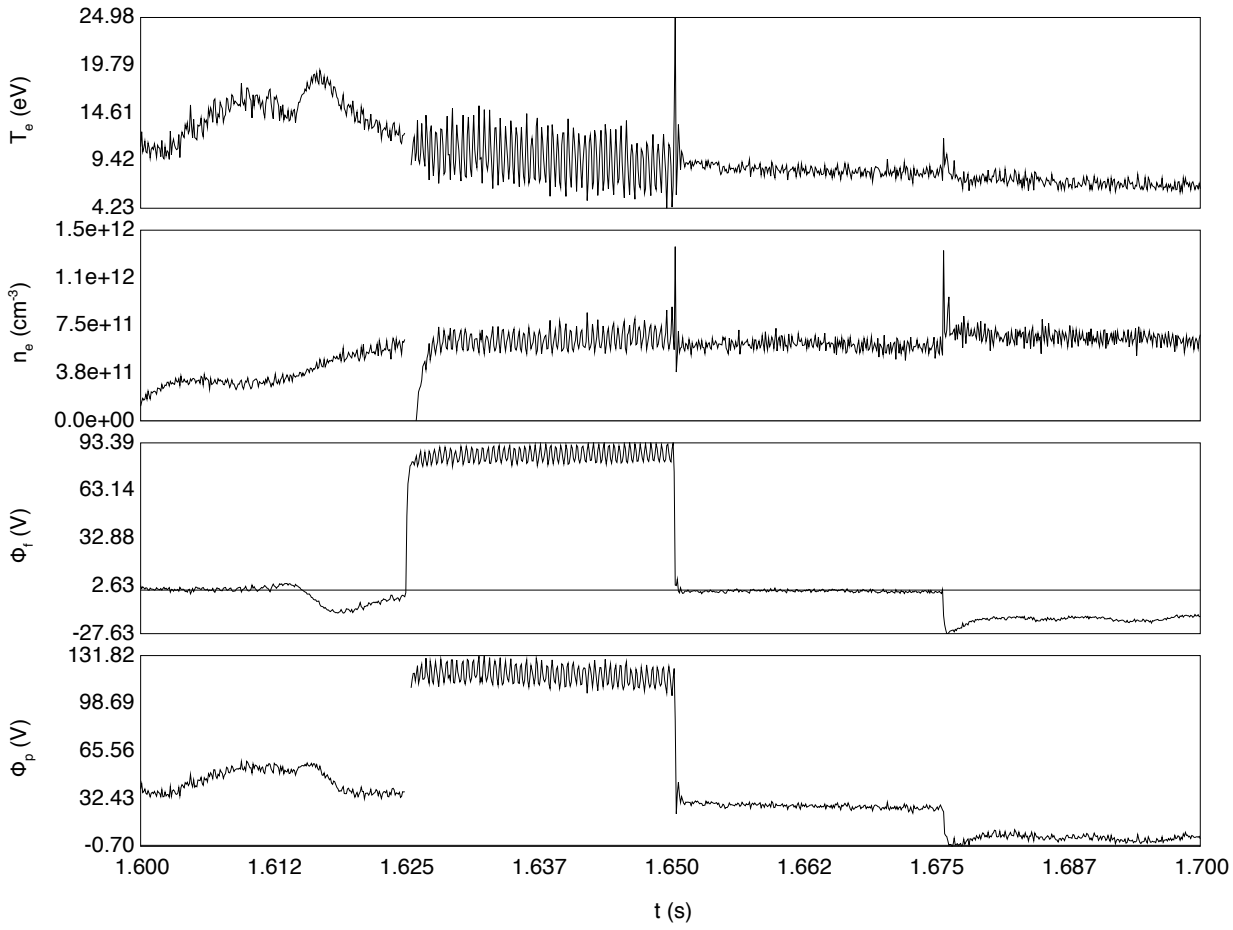

Figure 3.15: Analyzed triple probe data for a single shot.

Once T_e is calculated, it is combined into Equation 3.9 along with the measured current to measure n_e. Current should only ever flow in one direction. Areas that display negative current are indicative of local electron density being too small for the circuit to detect. Finally electron temperature and floating potential are combined to calculate the plasma potential at each data point using Equation 3.10. Figure 3.15 shows the analyzed time data. Profiles of plasma parameters are acquired by the method outlined in Section 3.2.

From the triple probe data, electric fields and density gradients can be calculated. Electric fields can be calculated from the average Φ_p in one of two ways. The first way involves taking a finite difference of the s coordinate in (s, u, v) space using triple probe positions. The second

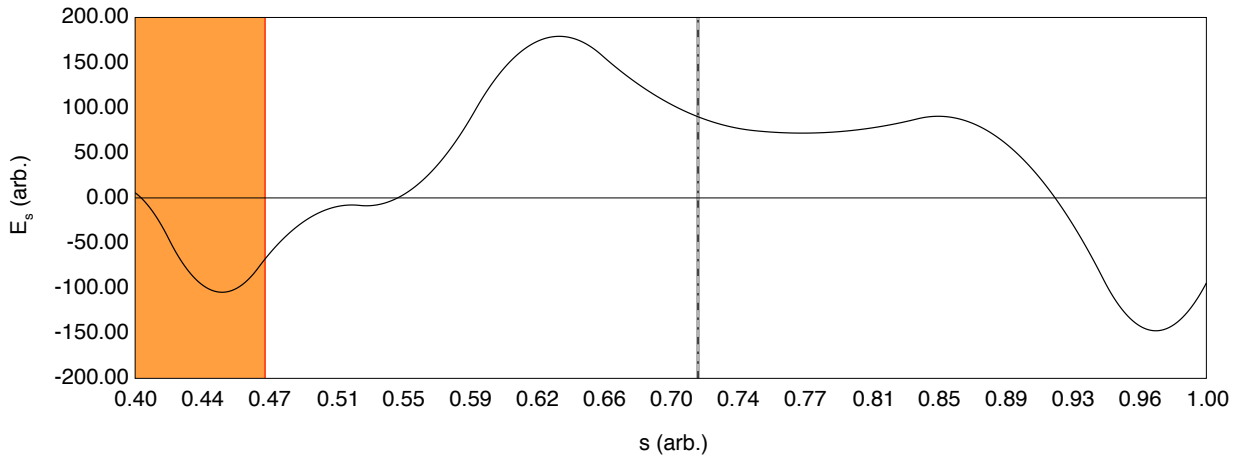

Figure 3.16: $\boldsymbol{E}_s$ calculated from triple probe Φ_p data in Flux surface space between the biasing probe (orange) and LCFS (vertical dashed line).

method involves taking a spline interpolation[40] in flux surface space assuming that data is axisymmetric. In other words, the spline is interpolated across the entire plasma column in flux surface space to ensure that first derivative is zero at $s = 0$. The electric field is then calculated taking the first derivative of the resulting spline function. In either case, $\boldsymbol{E}_s$ is calculated from Equation 3.23. The vector is transformed back into lab space (r, ϕ, z) to find $\boldsymbol{E}$. Electron pressure gradients are calculated from T_e and n_e in the same manner. For ion pressure gradients, quasi-neutrality is invoked, $n_e = n_i$, and the ion temperature is assumed to be cold $T_i \leq 1$ eV. Figure 3.16 shows a measured $\boldsymbol{E}_s$ profile in CTH.

3.4.2 Gundestrup Probe

In order to study the effects of edge flows on plasma stability, a localized measurement of the plasma flow is required. A Gundestrup probe is a multidirectional variant of a Mach probe. Mach Probes are used to measure plasma flows. A Mach probe consists of two tips, one faces upstream and the other faces downstream. Since the upstream tip leaves a wake downstream, the two tips collect unequal ion saturation currents. The ratio of the upstream to the downstream currents will be shown to be related to the Mach number of the plasma flow. Here, the Mach number, $M = \frac{v}{c_s}$, is defined as the ratio of the plasma flow velocity, v, to the plasma sound speed, c_s. The sound

speed is defined as[45]:

$$c_s = \sqrt{\frac{Zk_bT_e + k_bT_i}{m_i}} \tag{3.12}$$

where Z is the ionization state of the plasma. For these experiments on CTH, the plasma is made from hydrogen and therefore $Z = 1$.

The Gundestrup probe can resolve not only speed but also the general direction of plasma flow in a two dimensional plane. Sheared flows can be studied by moving the probe to different spatial locations and measuring changes in speed and/or direction. The primary objective of this work is to measure the changes in flow induced by modifying the edge electric field over the course of a plasma shot.

Theory

Strong electric fields or sharp density gradients, such as the edges of stellarators and tokamaks, induce a poloidal flow perpendicular to a magnetic field line. In order to understand the Mach probe theory in these conditions it is necessary to look beyond the diffusion as a primary mechanism. A purely convective treatment is more appropriate. From both isothermal fluid and kinetic solutions[45,46] the ratio of ion flux to opposing plates in a plasma is given for subsonic flows by

$$R = \frac{I_{up}}{I_{down}} = \exp\left[\frac{\left(M_{\|} - M_{\perp}\cot\eta\right)}{M_c}\right] \tag{3.13}$$

where R is the ratio of the upstream to downstream collected currents. The angle between the magnetic field vector and the tangent of a plate surface is η and $M_{\|}$ and $M_{\perp}$ are the parallel and perpendicular Mach numbers respectively. For cold ion plasmas, the calibration factor, $M_c \sim \frac{1}{2}$, will be the value assumed in this dissertation[45].

To extend this formulation from a single pair of plates to a Gundestrup Probe, the values of $M_{\|}$ and $M_{\perp}$ are solved for using a χ^2 minimization technique.

$$\chi^2 = \sum \left[R_M\left(M_{\|}, M_{\perp}, \eta\right) - R_E\right]^2 \tag{3.14}$$

The modeled current ratio R_M is taken from the right hand side of Equation 3.13. To aid the minimization algorithm and prevent numerical instabilities, Equations 3.13 and 3.14 are combined and rewritten into the equivalent form

$$\chi^2 = \sum_n \left(M_{\parallel} \sin \eta_n - M_{\perp} \cos \eta_n - M_c \sin \eta_n \ln R_n \right)^2 \tag{3.15}$$

and summed over each plate pair.

The value η is determined by

$$\eta = \theta_{probe} - \theta_B + \frac{\pi}{2} \tag{3.16}$$

where θ_{probe} is the angle between the plate normal and the horizontal. The angle, θ_B, is the angle between the magnetic field vector and the horizontal in the plane of the probe. This angle is determined by

$$\theta_B = \tan^{-1} \frac{\boldsymbol{B} \cdot \hat{\boldsymbol{\phi}} \times \hat{\boldsymbol{n}}}{\boldsymbol{B} \cdot \hat{\boldsymbol{\phi}}} \tag{3.17}$$

where $\hat{\boldsymbol{\phi}}$ is the unit vector in the toroidal direction and $\hat{\boldsymbol{n}}$ is the unit vector pointing in the direction of the probe shaft.

Design

The Gundestrup probe in this work consists of six tips biased into ion saturation I_{sat}. Each probe tip has a corresponding tip mounted on the opposite side of the probe arranged in such away that its collection area only faces one area of the plasma and shadowed from plasma flows on the opposite side. Six identical probe tips are mounted on an AX05 grade boron nitride core. Each probe tip is created from a single 1" diameter, 2" long, 316 alloy stainless steel rod. A $\frac{3}{4}$" diameter step is cut $\frac{1}{8}$ of an inch down from the top. A $\frac{1}{2}$" diameter bore is drilled through the center. This piece is then cut lengthwise every 60° producing six identical probe tips with an electrical gap the width of a saw blade between the tips.

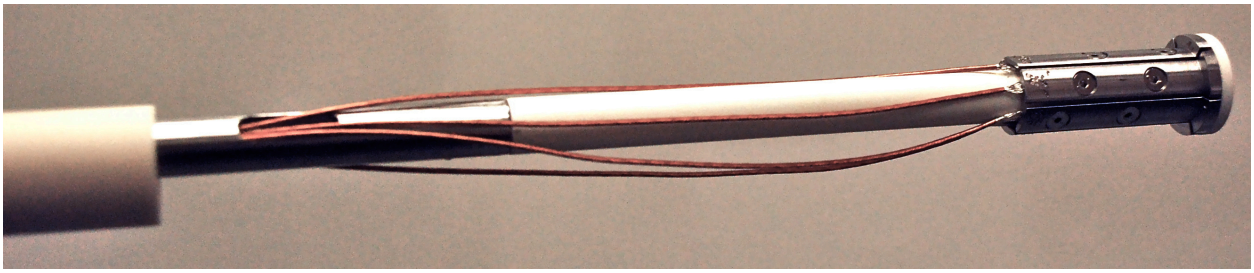

Figure 3.17: Photograph of the Gundestrup probe with the Alumina shield pulled back.

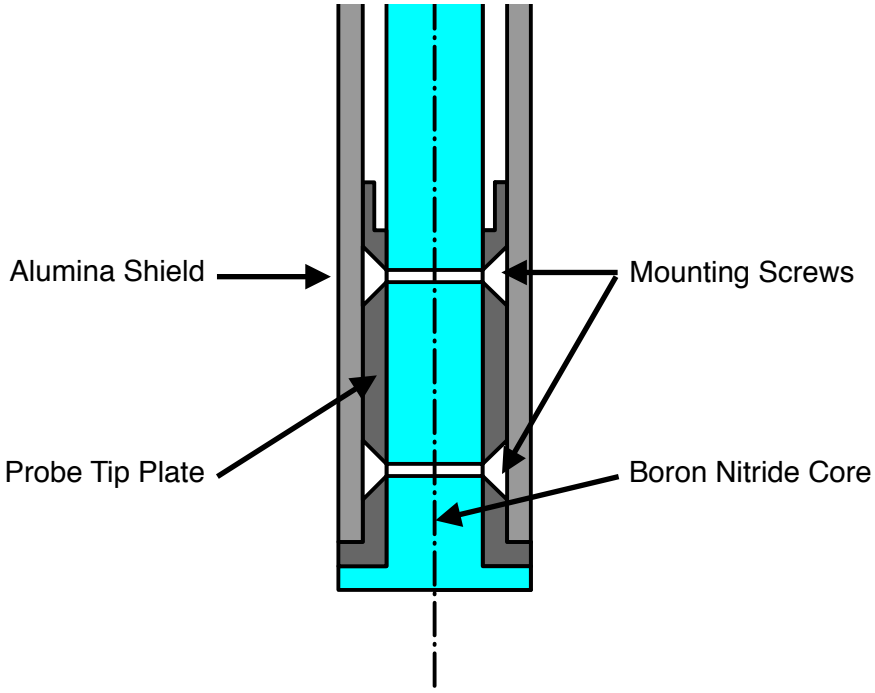

Figure 3.18: Scale diagram of the assembled Gundestrup probe tip.

The boron nitride core is turned down from a 1" diameter stock billet. A $\frac{1}{8}$" long, 1" diameter cap is left in place at one end with the rest of core turned down to a $\frac{1}{2}$" diameter. This cap confines signal pickup to just the poloidal and toroidal directions. A 1" long section is turned down to mate with the similar probe shaft used for the Triple Probe. The six probe tips screwed into the boron nitride core using $4-40$ $\frac{1}{4}$" inch flat head screws. This screw size sets the constraint on the number of possible probe tips for a given probe diameter. Six kapton insulated UHV wires are spot welded to a notch cut out of the bottom of the probe tips. A 1" OD, $\frac{3}{4}$" ID Alumina tube is placed over the probe tips so that only a $\frac{1}{8}$" section of the probe tip is left exposed. Total exposed area for each tip is $A \sim 84.5$ mm^2. A photograph of the assembled probe tip with the Alumina shield pulled back is shown in Figure 3.17.

Two $\sim$ 1" long slots are milled into opposite sides of the probe shaft. This allows venting of the probe shaft and a hole to feed through wires. The six wires are run down the length of the probe shaft to a six pin feed through. The boron nitride core is held in place with a setscrew. A 1" long, 1" diameter coupler 316 alloy stainless steel coupler hold the alumina tube press fit against the boron nitride core and probe tips. There is a $\frac{1}{2}$" long section turned down to a $\frac{3}{4}$" diameter to mate with the center of the alumina tube. Four holes drilled lengthwise allow venting and the collar is held in place with two set screws.

The Gundestrup probe is mounted on 36° horizontal port. Figure 3.19 shows a cross-sectional diagram of the mounted probe. The center of this port lies along a symmetry plane. The probe is mounted above the mid plane at a $\theta = 14.04^\circ$ angle above the mid-plane such that, when fully extended, the probe tip reaches the center of the vacuum vessel. Like the Triple Probe, the probe shaft is mounted onto a bellows. The bellows are mounted to a $1'$ long extension from plasma chamber in the same manner as the Triple Probe. A $4\frac{1}{2}$" to $2\frac{3}{4}$" zero length reducing flange adapts the probe system to the CTH port. Inside the chamber, a $1\frac{1}{2}$" diameter 316 alloy stainless steel tube with a flapped door prevents contamination of the electrodes during discharge cleaning. A teflon collar around the probe shaft inside the $1'$ long extension, prevents the probe from sagging. The

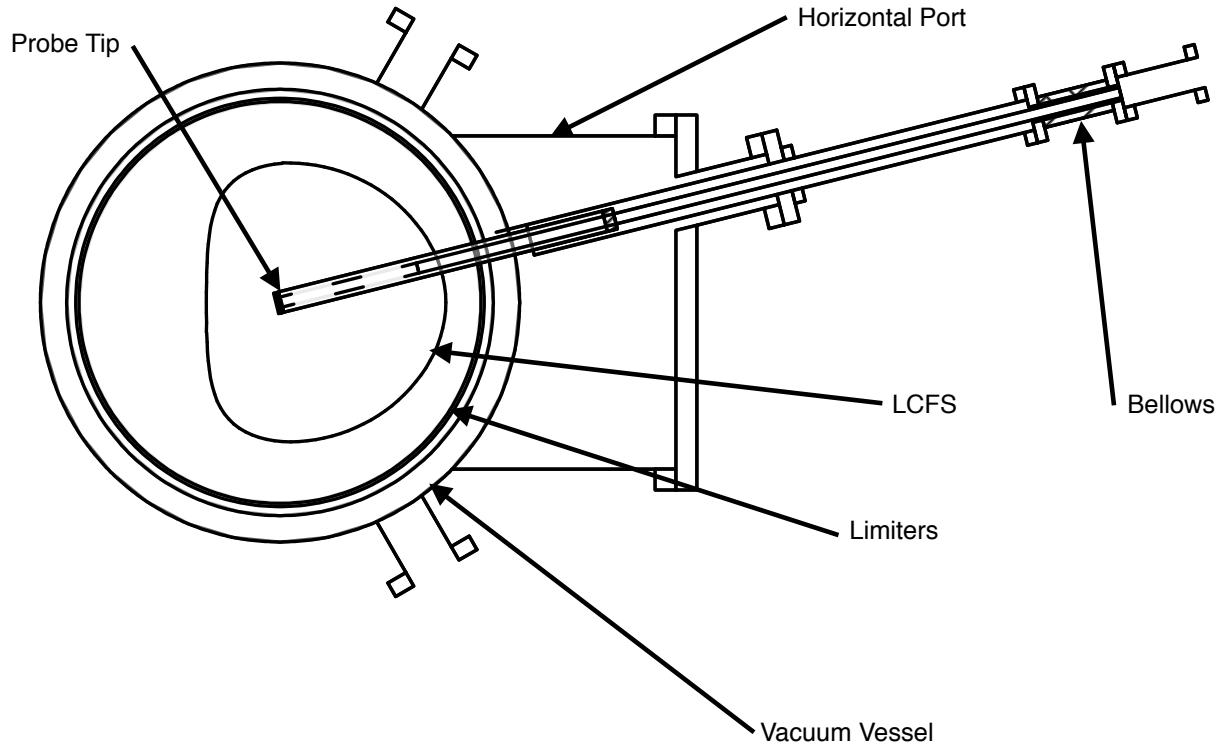

Figure 3.19: CTH cross-section of the Gundestrup probe mounted at $36°$. The probe is drawn at the full travel position.

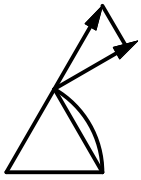

Figure 3.20: Scale diagram overlaying the deviation of a curved tip to a flat tip.

bellows are mounted to a 20" stepper motor driven probe drive in the same manner as the Triple Probe.

As built, each probe plate has a curved surface. The Gundestrup probe theory presented in this Section assumes flat plates. To quantify the applicability of this theory to the "as built" probe, the ratio of probe areas and the ratio of the surface normals will be examined. Figure 3.20 shows

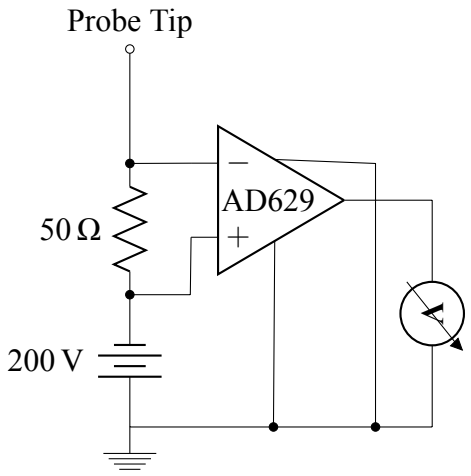

Figure 3.21: Op amp circuit diagram for a single Gundestrup probe tip. A complete Gundestrup probe circuit contains six identical circuits.

a scale diagram overlapping a flat plate to an as built curved plate. Taking the ratio of a flat plate surface area to a curved plate surface area

$$\frac{wr}{wr\frac{\pi}{3}} = \frac{3}{\pi} \sim 95\% \tag{3.18}$$

where w is the probe plate width and r is the probe radius. On a curved probe, the normal unit vector will deviate from the direction of the normal on a flat plate. Taking the component of the curved plate normal in the direction of flat plate normal at the point of highest deviation is

$$\hat{\boldsymbol{n}}_c \cdot \hat{\boldsymbol{n}}_f = \cos\frac{\pi}{6} \sim 87\% \tag{3.19}$$

where $\hat{\boldsymbol{n}}_c$ and $\hat{\boldsymbol{n}}_f$ are the unit vectors in the normal direction of the curves and flat plates respectively. These results suggest that modeling the as built plates as flat is reasonable for this Gundestrup Probe.

Channel	Name	Plate Designation
ACQ1962:INPUT_77	Probe 1	A
ACQ1962:INPUT_78	Probe 2	B
ACQ1962:INPUT_79	Probe 3	C
ACQ1962:INPUT_91	Probe 4	D
ACQ1962:INPUT_81	Probe 5	E
ACQ1962:INPUT_82	Probe 6	F

Table 3.4: The CTH mdsplus channels for the Gundestrup Probe.

Measurement Circuitry

Current drawn from each Gundestrup probe plate is measured through a unity gain differential amplifier circuit across a shunt resistor. Figure 3.21 shows a diagram of a measurement circuit for a single tip. Each probe circuit contains six identical circuits. Each probe tip is biased 200 V negatively with respect to ground to place each probe tip into ion saturation. Because each circuit is biased to -200 V, normal op amps cannot be used. The Analog Devices AD629 is used to avoid problems with common mode rejection[44]. For conditions in CTH, it is found that a shunt resistor of $50\ \Omega$ is works best for keeping signals within a ± 10 V range. All op amps are powered with a ± 12 V power supply with $0.1\ \mu$F filtering capacitors.

Data Analysis

The raw measured current data is collected throughout the entire CTH data shot on the DTAC system. Table 3.4 shows a table of the mdsplus database entries for the Gundestrup Probe. Raw data is converted to current using

$$I_{real} = Raw * 0.305185 \frac{1 \times 10^7 \frac{\mu\text{A}}{\text{A}}}{1000 \frac{\text{mV}}{\text{V}} * R} \tag{3.20}$$

where R is the value of the shunt resistor. For measurements presented in this dissertation, shunt resistors of $50\ \Omega$ are used. Since the Gundestrup probe is based on ratios of the collected currents, it is not strictly necessary to convert the raw signal to the actual current. None of the probe tips

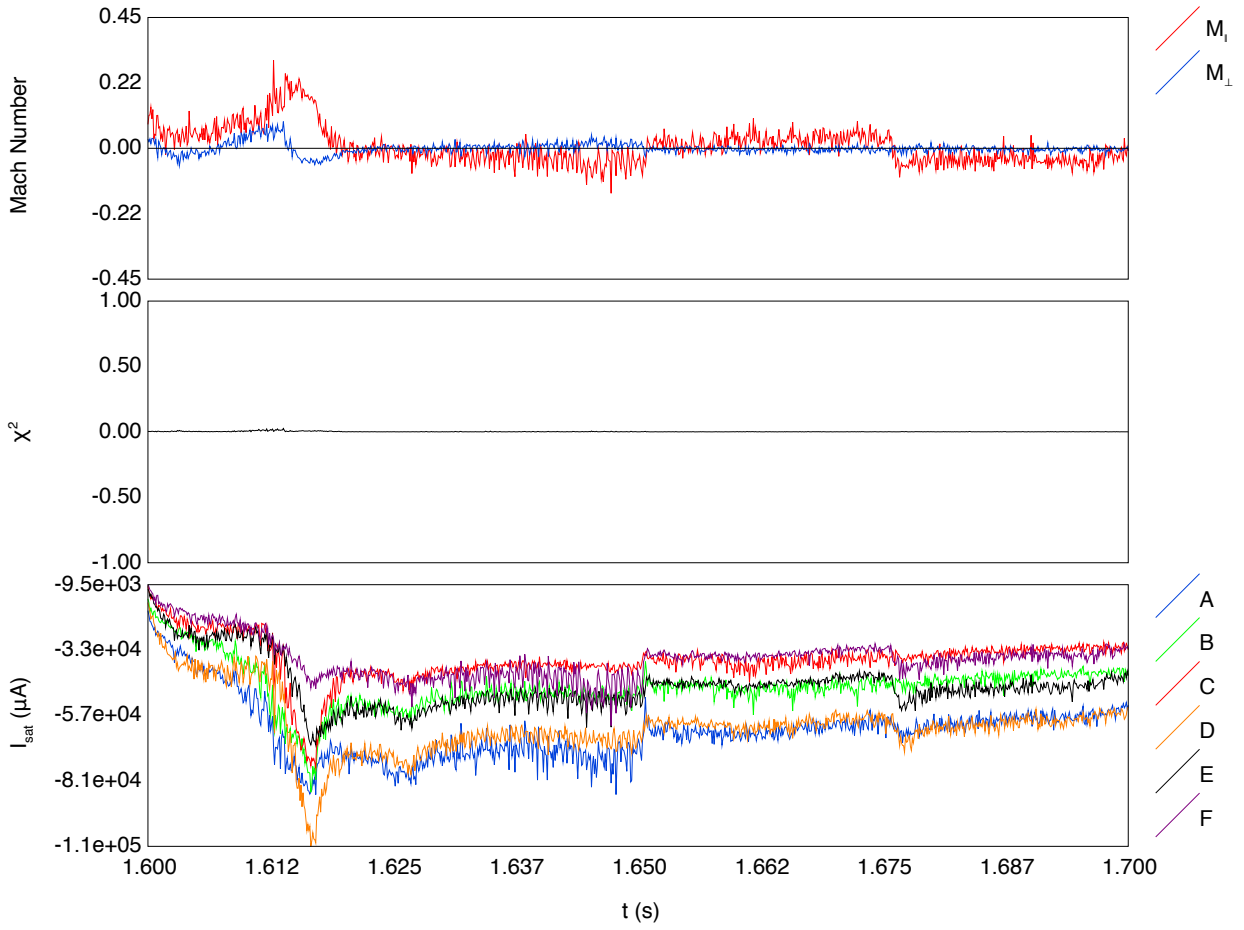

Figure 3.22: Parallel and Perpendicular Mach numbers, χ^2 values, and the raw currents measured from the Gundestrup probe for a single shot.

should be drawing current when there is no plasma present. In the absence of short circuits, any current offsets in the signal when there is no plasma should be the result of potential offsets in the measurement circuits. The initial value of the current signal is measured and used to offset the total signal in software for each channel.

Figure 3.22 shows the raw current data for a single shot, the measured parallel ($M_{\parallel}$) and perpendicular ($M_{\perp}$) Mach numbers and the χ^2 for signifying how close to the exact value fitted data reached. The ratios of currents collected on channels $A : D$, $B : E$ and $C : F$ are used to find $M_{\parallel}$ and $M_{\perp}$ by minimizing Equation 3.15 for each data point. For each shot, a `V3FIT` reconstruction

is performed from values averaged over the shot length. The magnetic field vector at each Gundestrup probe position is used to calculate the pitch angle between the magnetic field vector and the Gundestrup probe plate normal vector. Profiles of $M_{\parallel}$ and $M_{\perp}$ are obtained from the method outlined in Section 3.2.

3.5 Probe Measurements

To compare probe measurements from different areas of the plasma, a common framework must be employed. In fusion plasmas with closed magnetic surfaces, various plasma parameters are assumed to be constant over a magnetic flux surface. This makes the s coordinate, as discussed in appendix B, a natural value for normalizing probe positions. Each probe position is converted from lab space (r, ϕ, z) position to `VMEC` flux surface space (s, u, v) position using an average `V3FIT` reconstructed equilibrium for each time interval using the method discussed in Section 2.2.1. In this dissertation all profile data is presented as a function of the `VMEC` coordinate s position.

The coils necessary to create stellarator magnetic field topologies, place constraints on the shape of vacuum vessels and the placement of diagnostic access ports. This, along with space constraints and competition for port access with other diagnostic and vacuum infrastructure, can lead to mounting plasma diagnostics in locations where interpretation of measurements is challenging.

To illustrate this, the measurement positions of two probe systems are overlaid on top of the CTH magnetic surfaces in Figure 3.23. At the toroidal angle of $36°$, the Gundestrup probe is mounted on a horizontal port pitched at a downward angle of $14°$. At the toroidal angle of $72°$, the triple probe is mounted on a vertical port offset from the center of the vacuum vessel by 4 cm. Both probes have a maximum travel extent of 26 cm. However, because of their mounting locations, movement directions and differences in the shape of the magnetic flux surfaces, these probes sample different regions of the plasma.

When changing the positions of both probes by an equal distance in laboratory space, an unequal number of flux surfaces are traversed. Consider the triple probe path of the right side of Figure 3.23, for the first portion of probe travel defined from $z = 0.26$ m to $z = 0.15$ m (Region 1,

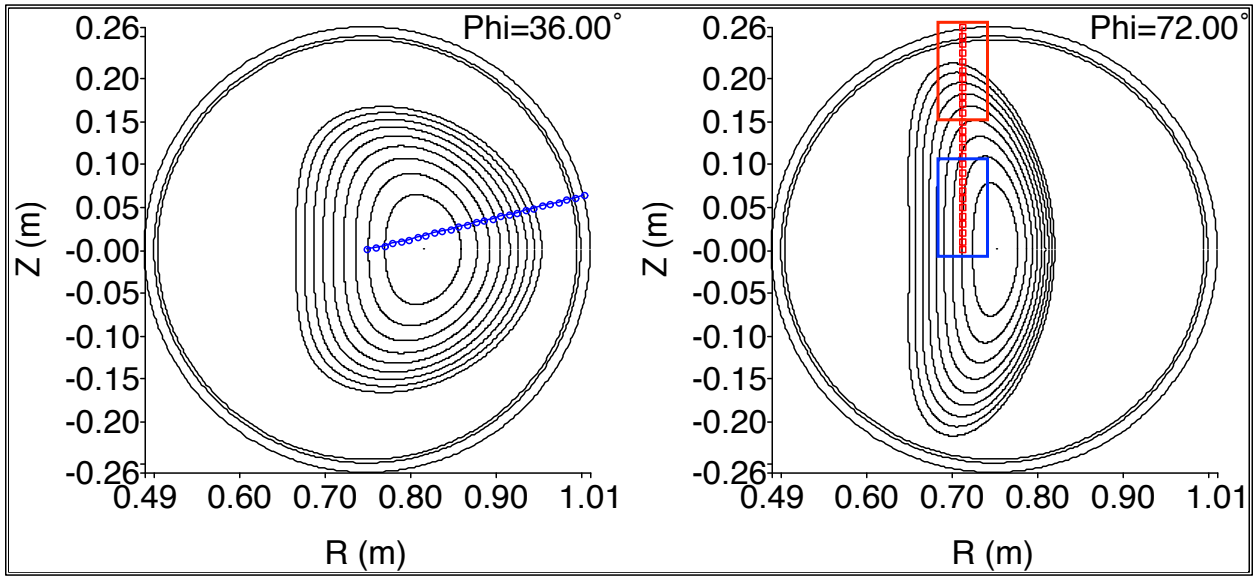

Figure 3.23: Probe path for the CTH Gundestrup (Left) and Triple (Right) probes. The red box marks the region where the probe travel is perpendicular to the magnetic surfaces (Region 1). The blue box marks the region where the probe travel is parallel to the magnetic surfaces (Region 2).

red box), the probe moves mainly perpendicular to the magnetic surfaces. However, for the second portion of probe travel defined by $z = 0.1$ m to $z = 0$ m (Region 2, blue box), the probe moves mainly parallel to the magnetic surfaces. That is, a 1 cm change in probe position in Region 1 crosses a greater number of magnetic surfaces than a 1 cm change in position of Region 2. Moreover, spatial features in the measured profiles by these two probes will not line up correctly when plotted solely as a function of probe position.

Moreover, when trying to determine vector quantities such as the electric field in laboratory space, only the component of that quantity in the direction of the diagnostic travel can be determined from one dimensional measurements. On CTH, the only possible location where a diagnostic could be mounted in a position allowing for diagnostic travel perpendicular to the magnetic flux surfaces is at the $\phi = 36°$ symmetry plane along the mid-plane and subsequent symmetry planes ever $\Delta\phi = 72°$. The lack of poloidal or toroidal symmetry in the stellarator magnetic surfaces, means that measurements obtained from a region where the direction of probe travel is orthogonal to the magnetic surfaces, are only valid for that specific location and at matching locations in each

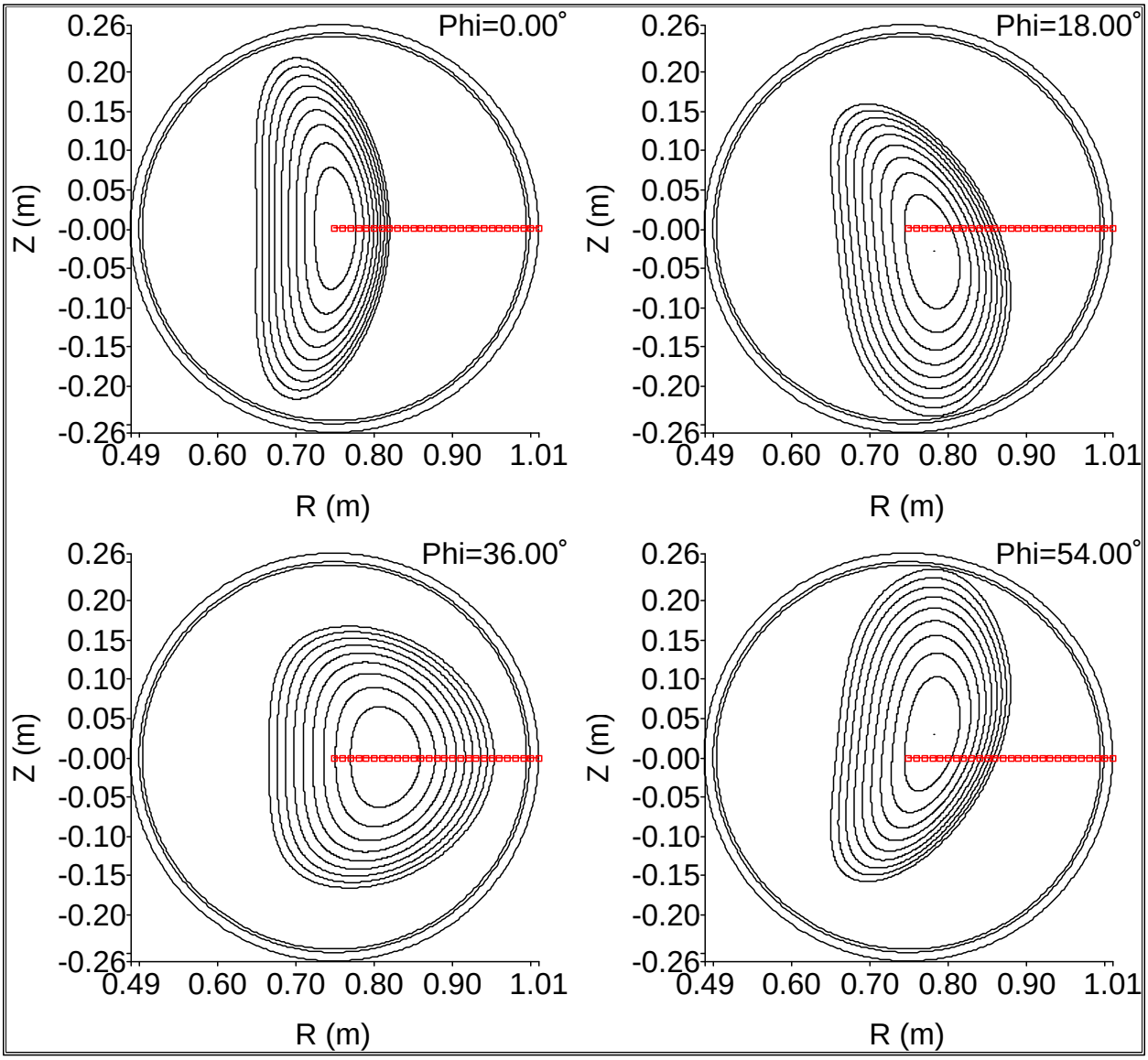

Figure 3.24: Simulated probe positions along the mid-plane.

field period. At different locations within the plasma, the magnetic surfaces expand and compress altering the electric field structure.

3.5.1 Simulated Diagnostics

The position of an in-situ measurement can be transformed into flux surface space. To compare plasma profiles, it is natural to use the most radial-like flux coordinate s as many plasma parameters can be assumed to be constant along a magnetic field line. To demonstrate the use of transforming

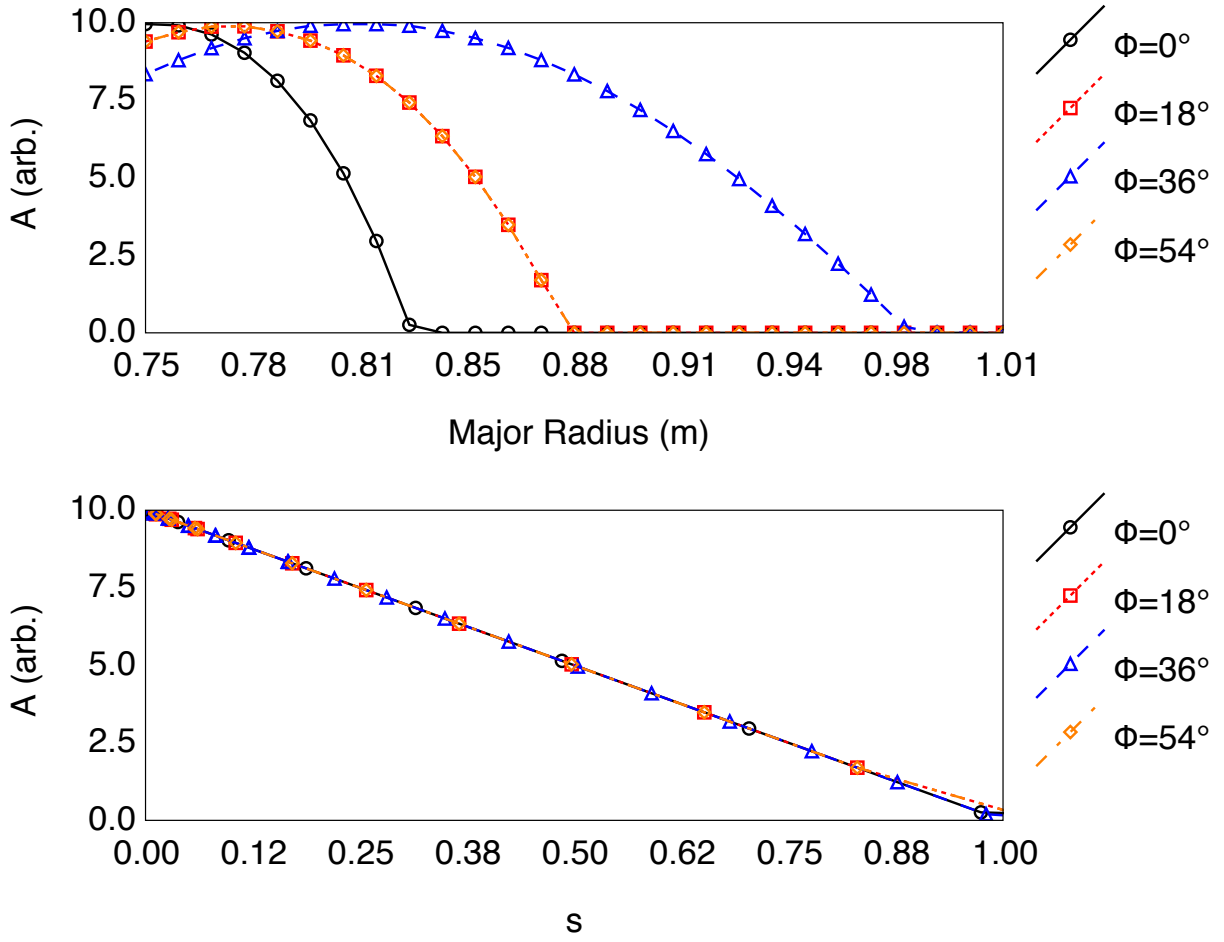

Figure 3.25: An arbitrary flux surface constant quantity plotted as a function of both major radius and flux surface s position. In laboratory space flux surface constant quantities do not align with probe positions.

laboratory space (r, ϕ, z) measurement positions to flux surface space (s, u, v) space for data analysis, Figure 3.24 shows four measurement paths all utilizing the same (r, z) coordinates at different toroidal angles. These toroidal cross-sections are chosen for uniform spacing within a field period and do not represent real diagnostic positions.

A simulated flux surface constant quantity takes the form of;

$$A(s) = \begin{cases} A_0 (1 - |s|) & |s| < 1 \\ 0 & |s| > 1 \end{cases} \tag{3.21}$$

Figure 3.25 shows a plot of the simulated flux surface constant quantity in both laboratory space (r, ϕ, z) and flux surface space (s, u, v) coordinates for a typical ECRH pulse on CTH for each of the four probe paths. The laboratory space (r, ϕ, z) position of each probe position is converted into flux surface space (s, u, v) position by the method outlined in Section 2.2.1 using spline interpolated `VMEC` quantities.

Since the quantity is constant on a flux surface, when plotted as function of s, all probes measure the same profile even though the flux surface probe s positions do not align. When plotted as a function of measurement position however, measured profiles show deviations. The location of the last closed flux surface ($s = 1$) in laboratory space, shown where the quantity A becomes zero, does not align. The toroidal angles of ($\phi = 18°$ and $\phi = 52°$) are antisymmetric about the mid-plane on either side of the symmetry planes of ($\phi = 0°$ and $\phi = 36°$). The probe positions of ($\phi = 18°$ and $\phi = 54°$) represent a special case where laboratory space measurements align.

3.5.2 Extrapolating Global Parameters

In fusion devices, nested flux surfaces are defined as surfaces of constant pressure where the magnetic pressure balances the plasma pressure. Figure 2.1 shows the nested magnetic surfaces in the CTH device. It is further assumed that a flux surface is a surface of constant electric potential. This implies that the plasma pressure P and plasma potential Φ_p are only functions of the s coordinate. While this is clearly true for the pressure (because it is the inherent assumption for computing the equilibrium), it remains to be verified for the electric potential.

A test of this assumption cane done by considering the path taken by the triple probe. As noted in Region 2 of Figure 3.24, the motion of the triple probe is mostly parallel to the magnetic surfaces. This means that the u position of the probe is changing, while the s position nearly constant. If plasma potential is a flux surface constant quality, the triple probe should measure the same value regardless of u position.

Figure 3.26, shows a plot of the plasma potential as a function of the real space position of the probe. The last four positions correspond to the movement of the probe at approximately a

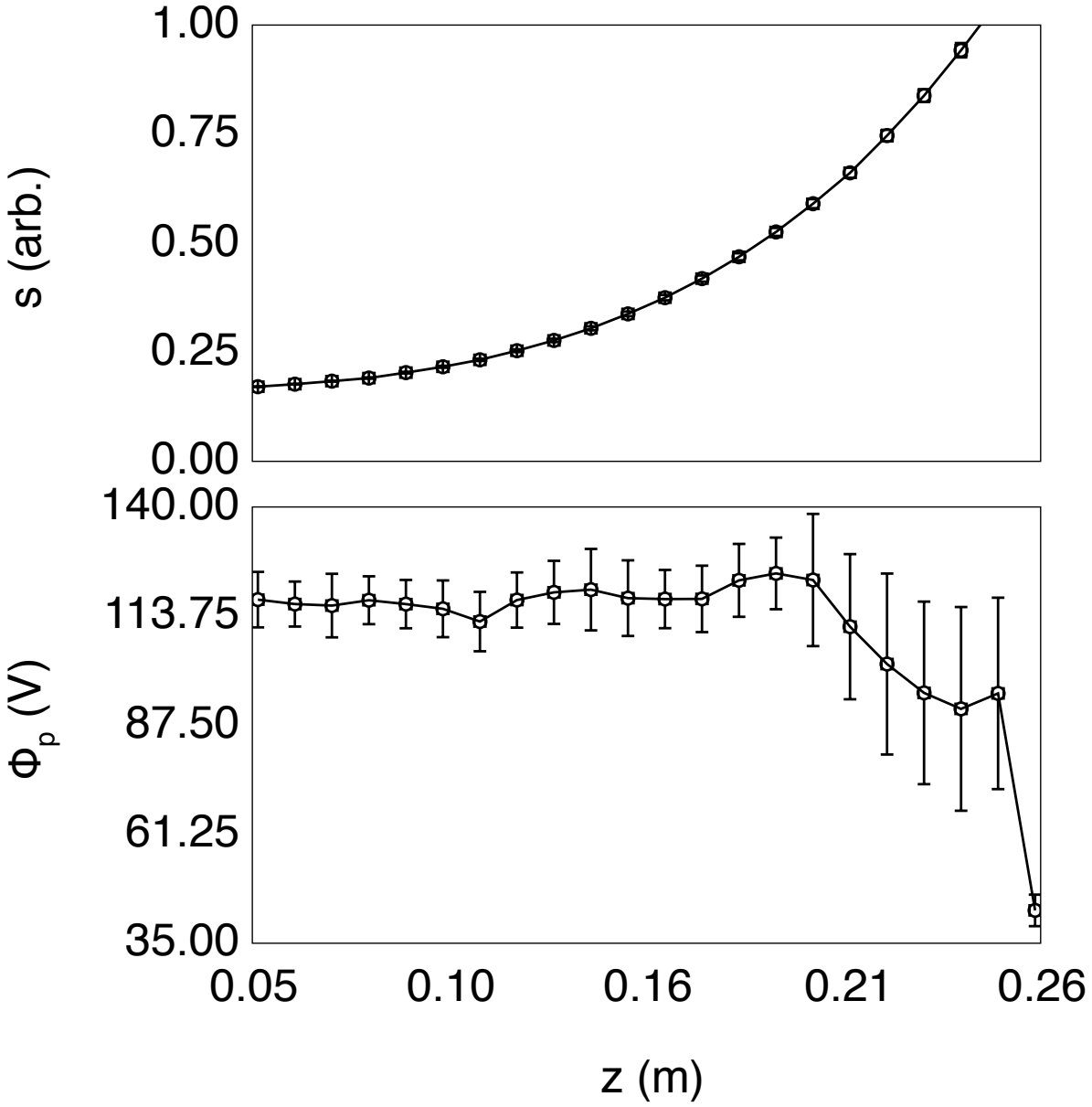

Figure 3.26: Plot comparing the change in plasma potential (Φ_p) to the change in flux surface space s position as a function of position. This shows Φ_p is a flux surface constant quantity.

constant value of s. In this region, the variation of $\frac{\delta\Phi_p}{\langle\Phi_p\rangle} = 1.2\%$, while $\frac{\delta s}{\langle s\rangle} = 10.9\%$. From this, it is concluded that modeling the flux surfaces as equipotential surfaces is a reasonable approximation. This implies that the plasma pressure P and the plasma potential Φ_p are only functions of the s coordinate. This section will focus on deriving the electric field. However, all methods discussed apply equally to gradients in the plasma fluid pressure.

The generalized gradient operator is defined to be

$$\nabla\Phi = \frac{\partial\Phi}{\partial u^i}\boldsymbol{e}^i \tag{3.22}$$

using the contravariant basis vectors. The electric field can now be defined as

$$\boldsymbol{E} = -\nabla\Phi_p\left(s\right) = -\boldsymbol{e}^s\frac{\partial}{\partial s}\Phi\left(s\right) = E_s\left(s\right)\boldsymbol{e}^s \tag{3.23}$$

The contravariant basis vector of the electric field and related to the covariant basis vectors of the magnetic field (Equation 2.5) by

$$\boldsymbol{e}_i \cdot \boldsymbol{e}^j = \delta_i^j \tag{3.24}$$

This means that $\boldsymbol{E}$ points in a direction normal to a magnetic surface and is orthogonal to $\boldsymbol{B}$. Since Φ_p is constant on a flux surface, the covariant electric field components (E_s) is also constant on a flux surface. As a consequence, by measuring a profile of Φ_p at any arbitrary position in any arbitrary direction, the total $\boldsymbol{E}$ can be determined everywhere within the s extent of the measured profile. Derivatives of flux surface constant quantities can be obtained by taking a finite difference in s or through a cubic spline interpolation. Both methods will be used throughout this dissertation. The method used will be identified for each measurement presented.

As a simple example of calculating the electric field, consider a modeled electric potential of the form in Equation 3.21. From the definition of the electric field (Equation 3.23), the value of $\frac{\partial}{\partial s}\Phi\left(s\right)$ is also only a function of the s coordinate and thus constant on a flux surface. Figure 3.27 shows the progression from a flux surface space potential to a laboratory space electric field. As a

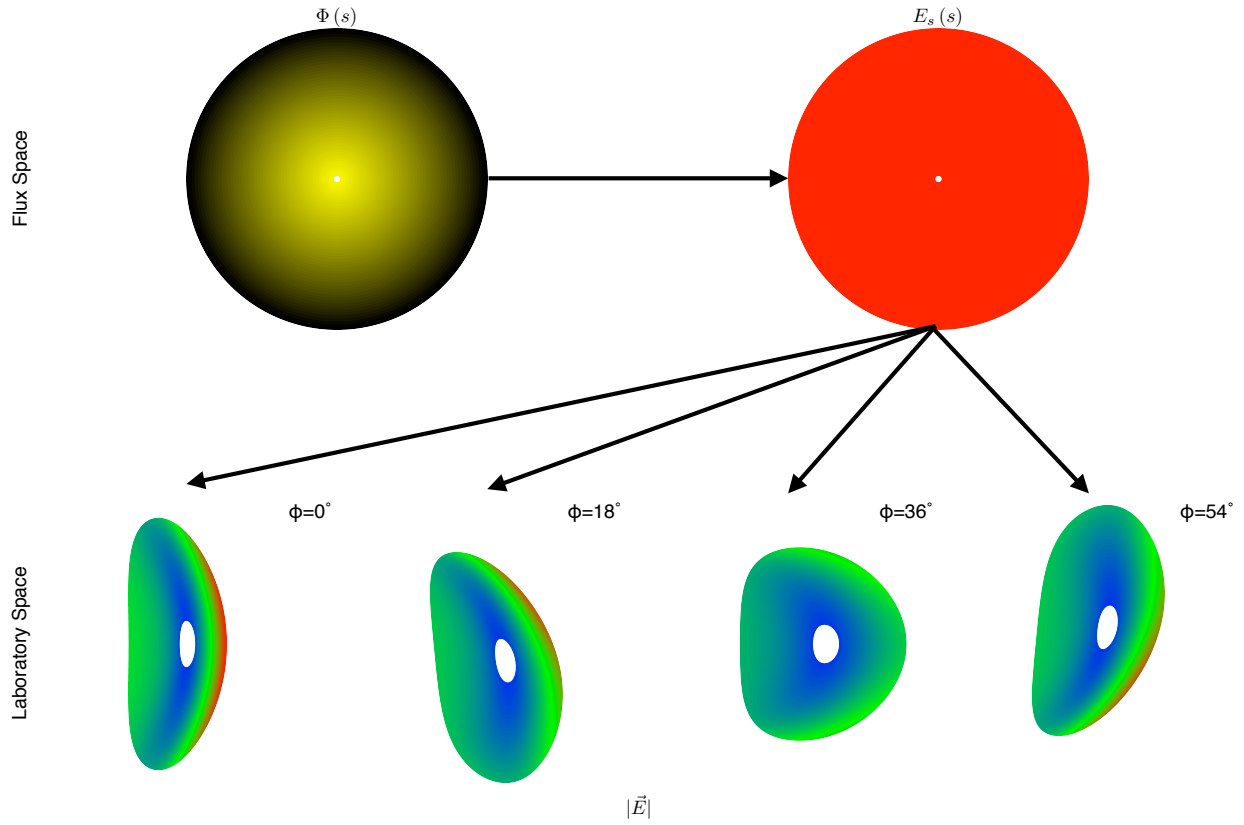

Figure 3.27: Starting from a potential profile (black $\Phi(s) = 0$ V, yellow $\Phi(s) = 10$ V), the flux surface space E_s (red $E_s(s) = 10arb.$) can be obtained. $|\boldsymbol{E}|$ (blue $|\boldsymbol{E}| = 0\frac{\mathrm{V}}{m}$, red = $|\boldsymbol{E}| = 240\frac{\mathrm{V}}{m}$) is obtained by converting E_s to laboratory space using the contravariant basis vectors at any (s, u, v) position. All cross sections are plotted from $s = 0.02$ to $s = 1$.

reminder, the flux surface space vector components do not carry the same units as the laboratory space counterparts.

Figure 3.28 shows various plots of electric field quantities measured at the probe positions in Fig 3.24 for a potential of the form of Equation 3.21. Figure 3.28a shows the magnitude of the gradient of potential in flux surface space (E_s). The quantity E_s represents a flux surface constant quantity. In Figure 3.28b E_s is transformed back into laboratory space providing the complete electric field vector at each probe position. Figure 3.28c shows the difference between calculating the total electric field from the flux surface constant E_s quantity and measuring the electric field directly from finite difference in probe position at the $\phi = 18°$ probe path. The deviation in these two methods arises from the fact that probe travel is not in the direction of the electric field.

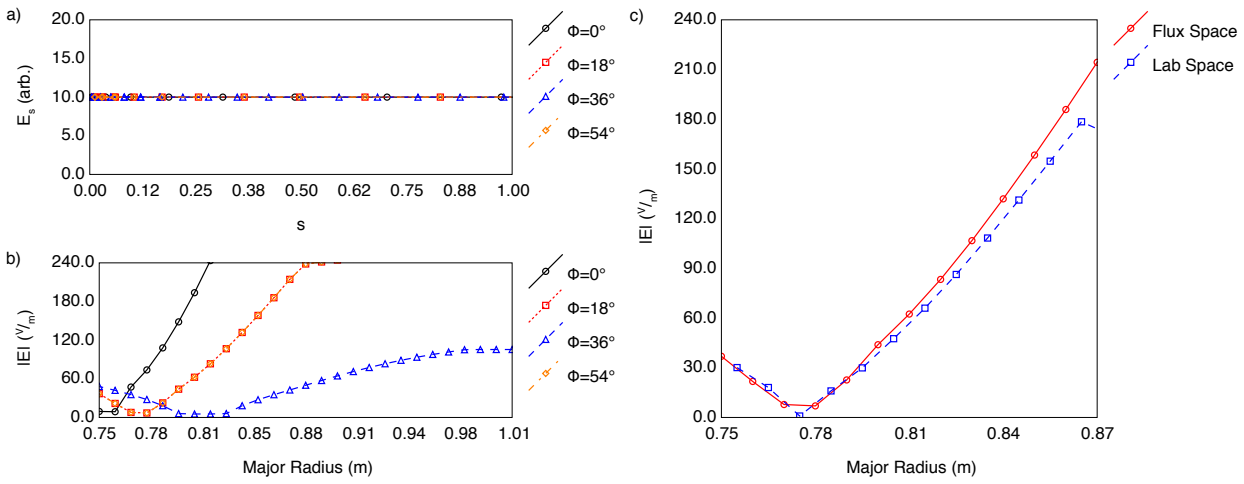

Figure 3.28: a) Plot of E_s measured at each probe position. b) Plot of $|\boldsymbol{E}|$ calculated from E_s. c) Difference between electric field calculated from E_s quantity and the taking a finite difference of direct probe data at $\phi = 18°$.

Direct probe measurements can only measure the component of the electric field in the direction of the probe travel. However, by transforming potential profiles into flux surface space, the flux surface constant quantity E_s can be obtained. As a consequence, by measuring a potential profile anywhere, the full electric field vector can now be determined everywhere in the plasma. Figure 3.27 shows the magnitude of the electric field at the toroidal cross-sections shown in Figure 3.24. The red shaded areas shown represent regions of strong electric field. The blue shaded regions represent areas of weak electric field. On right side (CTH outboard), the magnetic surfaces become highly compressed and resultant electric fields become strong. Toward the magnetic axis, the surfaces expand and electric fields become weak.

The methods developed here will be used for determination of the full electric field and pressure gradient vectors. It has been shown how these vectors are orthogonal to the magnetic fields. The presence of electric fields and pressure gradients transverse to a magnetic field will induce a flow perpendicular to both. Understanding the electric fields and pressure gradients is important for understanding plasma flow.

Chapter 4

Results

To study the effect of driven plasma rotation on plasma stability, edge biasing experiments have been performed on the CTH device. The goals of edge biasing experiments are to: modify the edge electric field, measure an induced perpendicular flow, demonstrate the role electric field plays inducing flows and measure the enhancement or suppression of plasma instabilities associated with these flows. This chapter will discuss various edge bias experiments performed in ECRH only plasmas in the CTH device.

4.1 Edge Biasing Experiments

All edge biasing experiments are performed by inserting the Biasing probe described in Section 3.3.1 past the last closed flux surface. Various biasing schemes are employed over the course of a shot. In each case, when the bias voltage is set to 0 V, this condition will be considered the reference or baseline against which all other biasing conditions are compared to.

For each shot, data is collected from the triple probe and Gundestrup Probe. Between shots, the probes are moved in 1 cm steps into the plasma as described in Sections 3.4.1 and 3.4.2. The triple probe data is used to determine the plasma parameters. Electric fields will be measured from the Φ_p by taking the gradient in flux surface space as described in Section A.1.4 and transformed back into the laboratory frame. The pressure gradient is determined from T_e and n_e in the same manner. Parallel and perpendicular flows are measured by scanning the Gundestrup Probe, as described in Section 3.4.2.

Two main experiments are described in this study. The first, Experiment A, is a high input heating power run in which all three ECRH power supplies are used to generate the plasma. The second, Experiment B, is a lower power run in which only one of the ECRH power supplies is used.

Shot Numbers	$11081821 - 11081837$
HF Current	4500 A
TVF Current	750 A
RF 1 Power	4 kW
RF 2 Power	4 kW
RF 3 Power	6 kW

Table 4.1: CTH run parameters for biasing experiment A.

Shot Numbers	$11090828 - 11090832, 11090834 - 11090850$
HF Current	4600 A
TVF Current	650 A
RF 2 Power	6 kW

Table 4.2: CTH run parameters for biasing experiment B.

The overall operating parameters foreach of these cases are given is Table 4.1, for Experiment A, Table 4.2, for Experiment B.

4.1.1 Data Analysis

Each shot is divided into a number of time slices, typically 4 or 5. At each time slice, the magnet coil currents are averaged over this time interval and `V3FIT` is run to produce a `wout` file for that shot number and time interval. `V3FIT` is configured to calculate the plasma equilibrium on 100 flux surface s positions. This is done to minimize errors in interpolated values between calculated flux surfaces. Appendix B details the various quantities that can be calculated from the `V3FIT` reconstruction. The reconstruction is used to obtain a model of the magnetic field structure. This model is used to transform probe positions using the procedures outlined in Chapter 3 and Appendices A and B, and to determine flows in the plasma.

Probe Data

Triple probe and Gundestrup probe data are analyzed and averaged for each shot number and time slice. The method of finding time slice averaged data error analysis is outlined in Section 3.2. Triple probe and Gundestrup analyses are outlined in Sections 3.4.1 and 3.4.2 respectively.

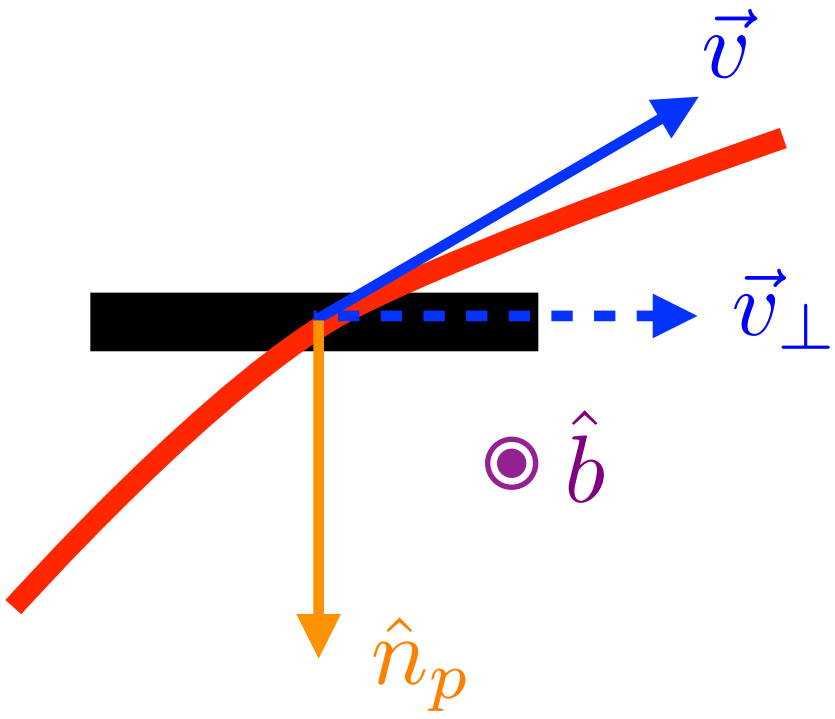

Figure 4.1: An exaggerated view of the intersection of the Gundestrup probe tip (black bar) with the curved flux surface (red line). The magnetic field direction (purple) is pointing into the paper and the orange line shows the direction of the probe shaft. The Gundestrup probe only measures the projection of the flow (blue line) in the plane of the probe tips (dashed blue line).

The error in the flux surface space probe position (s), is estimated by converting the maximum extents of the probe tips from laboratory space to flux surface space. For the triple probe, the probe tip is ~ 3 mm long. The maximum and minimum s values are calculated by taking the ± 1.5 mm of the probe position and converting that into flux surface space. The complete measurement tip of the Gundestrup probe is a 1" diameter cylinder $\frac{1}{8}$" in length. To estimate the error, eight positions on the inward and outward face of the tip are sampled and converted into flux surface space. The maximum and minimum s extent in flux surface space of these sampled positions are used to estimate the resulting spatial error. Since the Gundestrup probe tip is physically bigger than the triple probe tip, it is expected that Gundestrup probe position error will be greater than the corresponding triple probe error.

Electric field and pressure gradients are determined from the triple probe using the procedure outlined in Section 3.4.1. The resulting profiles values of the flux surface space electric field ($\boldsymbol{E}_s$)

and pressure gradient (∇P) are interpolated to the Gundestrup probe s positions. The contributions to the plasma flows by the E-cross-B ($\boldsymbol{E} \times \boldsymbol{B}$) and diamagnetic ($-\nabla P \times \boldsymbol{B}$) drift are estimated from Equation 2.9. However, these flows cannot be directly compared to Gundestrup probe measurements.

The component of the total drift representing the perpendicular flow in the plane of the Gunderstrup Probe is estimated using

$$v_\perp = \boldsymbol{v} \cdot \hat{\boldsymbol{b}} \times \hat{\boldsymbol{n}}_p \tag{4.1}$$

where $\hat{\boldsymbol{b}}$ is the unit vector in the direction of the magnetic field and $\hat{\boldsymbol{n}}_p$ is the unit vector pointing in the direction of the Gundestrup probe shaft. The local sound speed is calculated from Equation 3.12, at each Gundestrup probe s position, using either a linear interpolation or spline interpolation of T_e and assuming a T_i value of $\sim$ 1 eV. Since T_i is on the order of $\sim$ 10% of T_e it is expected that, errors in T_i estimation will produce errors in c_s on the order of $\sim$ 10%. Normalizing the perpendicular flow to the sound speed allows a direct comparison to $M_\perp$.

Biasing Probe and LCFS Positions

In order to interpret the profile measurements, the positions of the LCFS and the biasing probe must be converted in the flux surface s coordinate as well. Under normal `V3FIT` operation the limiter positions are provided as a fitting input parameter. This makes the $s = 1$ surface the LCFS. However to allow probe measurements to extend into the scrape off layer, the CTH limiter input is artificially expanded beyond the wavelength limiters. In ECRH only plasmas, the low values of plasma β makes it reasonable to assume that vacuum surfaces and plasma surfaces are the same.

To interpret the probe positions, it becomes necessary to determine the location of the physical limiters which determine the location of the LCFS. This is achieved by performing a search for where the innermost flux surface intersects any of the wavelength limiters. This search is performed for each time slice of all CTH shots. These positions are averaged together. The standard deviation is calculated to account for any error caused by shifts in the plasma position between shots.

The biasing probe position is directly transformed into flux surface space. The transformation is performed for each probe position for each time slice. The bottom center ($r = 0.712$ m, $\phi = -3.07°, z = 0.165$ m) and 1" ($r = 0.712$ m, $\phi = -3.07°, z = 0.187$ m) above that position of the bias probe tip are used as the lab space positions of the biasing probe. The transformed s positions are averaged together. Errors in the position arising from shifts in the plasma position shot to shot are accounted by calculating the standard deviation of the biasing probe s positions.

4.2 Plasma Parameters During Biasing

In this section, the measurements from the two experimental configurations described in tables 4.1 (Experiment A) and 4.2 (Experiment B) are presented. Figures 4.2 to Figures 4.4 present the results from experiment A. Figures 4.5 to Figures 4.7 present the results from experiment B. In each figure, three plots are given. As discussed throughout this dissertation, it is essential to be able to make a direct comparison between the different systems. As such, all probe spatial data is presented as a function of the `VMEC` flux coordinate s.

Plot (a) in each figure summarizes the measurements from the triple probe and Gundestrup Probe. The top plot presents the parallel ($M_{\|}$) and perpendicular ($M_{\perp}$) Mach number measured from the Gundestrup Probe. The remaining four plots are electron temperature (T_e), electron density (n_e), floating potential (Φ_f) and plasma potential (Φ_p) measured from the triple probe. It is important to note that in flux surface space, the triple probe and Gundestrup probe reach different depths into the plasma. In each plot, the projected extent of the biasing probe in flux coordinates is shown as an orange strip. The LCFS is shown as a vertical dashed line.

Plot (b) in each figure, compares the measured $M_{\perp}$ to the theoretical calculation of the plasma drift. Electric fields and pressure gradients are measured from triple probe data. This limits theoretical flow calculation to the depth of the triple probe. In each plot, the projected extent of the biasing probe in flux coordinates is again shown as an orange strip and the LCFS is shown as a vertical dashed line.

For plot (c), in each of the following figures, shows the time evolution of the applied biasing voltage and resulting current measured off the biasing probe. The experimental data is analyzed during the three time intervals when the probe is at 100 V, 0 V and -100 V. The shaded area represents the time interval used for each figure. It is noted that during the initial 0 V biasing phase, the plasma is still forming in the CTH vacuum vessel. As a result plasma conditions are somewhat unstable. The second 0 V biasing phase is used as the comparison case for these studies as described in Section 3.3.1.

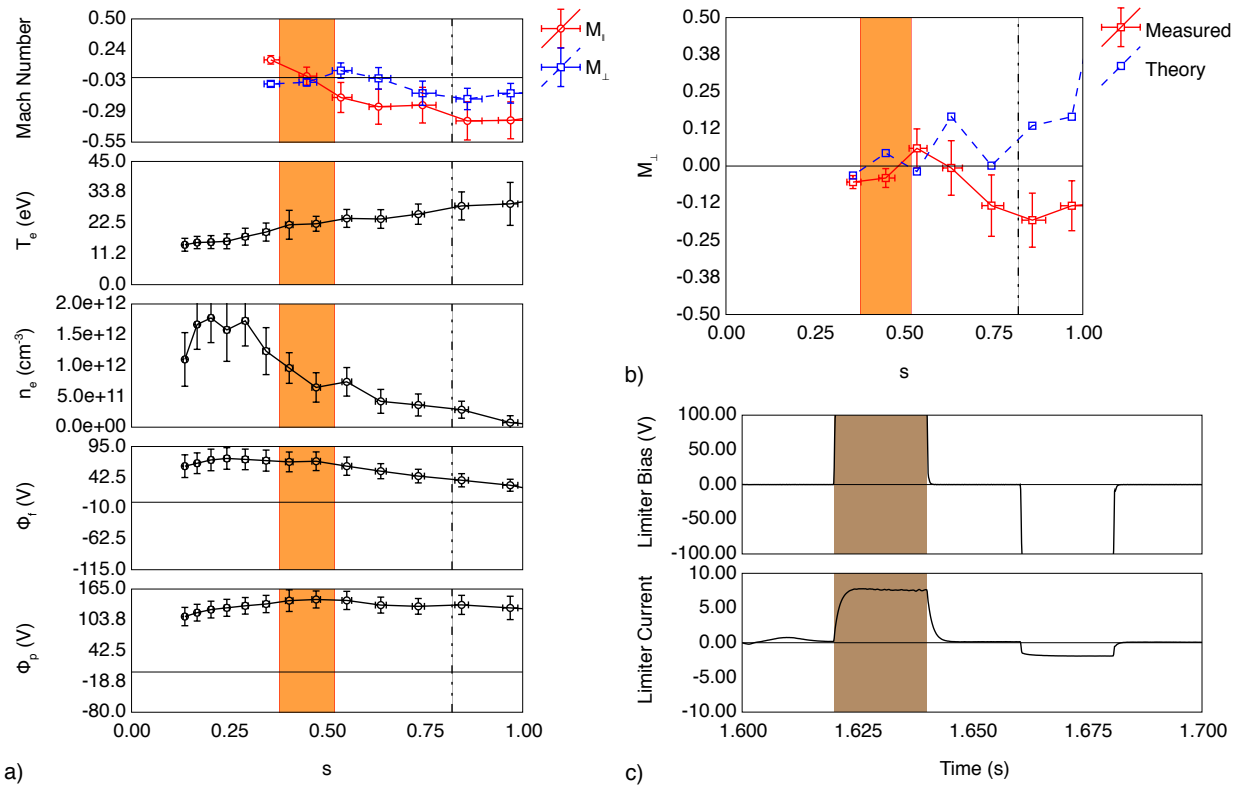

Figure 4.2: Data for experiment A from time interval 1.62 s-1.64 s. a) From Top to Bottom: Mach Number (M), Electron Temperature (T_e), Electron Density (n_e), Floating Potential (Φ_f), Plasma Potential (Φ_p). b) Measured and calculated values of $M_\perp$. c) Measured bias voltage and current. The orange shaded region represents the extent of the biasing probe tip. The vertical dashed dotted line marks the LCFS. The shaded region in the lower right corner marks the time interval that profile data is averaged over.

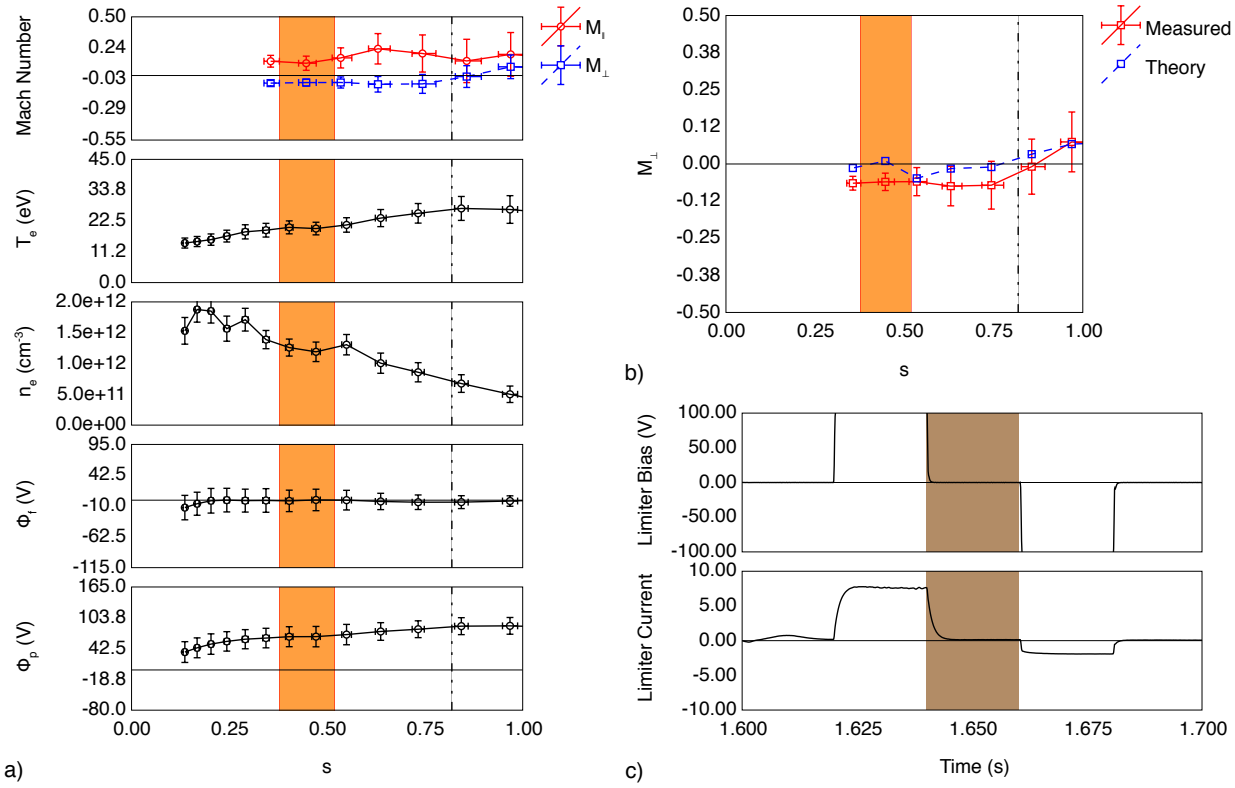

Figure 4.3: Data for experiment A from time interval 1.64 s-1.66 s. a) From Top to Bottom: Mach Number (M), Electron Temperature (T_e), Electron Density (n_e), Floating Potential (Φ_f), Plasma Potential (Φ_p). b) Measured and calculated values of $M_\perp$. c) Measured bias voltage and current. The orange shaded region represents the extent of the biasing probe tip. The vertical dashed dotted line marks the LCFS. The shaded region in the lower right corner marks the time interval that profile data is averaged over.

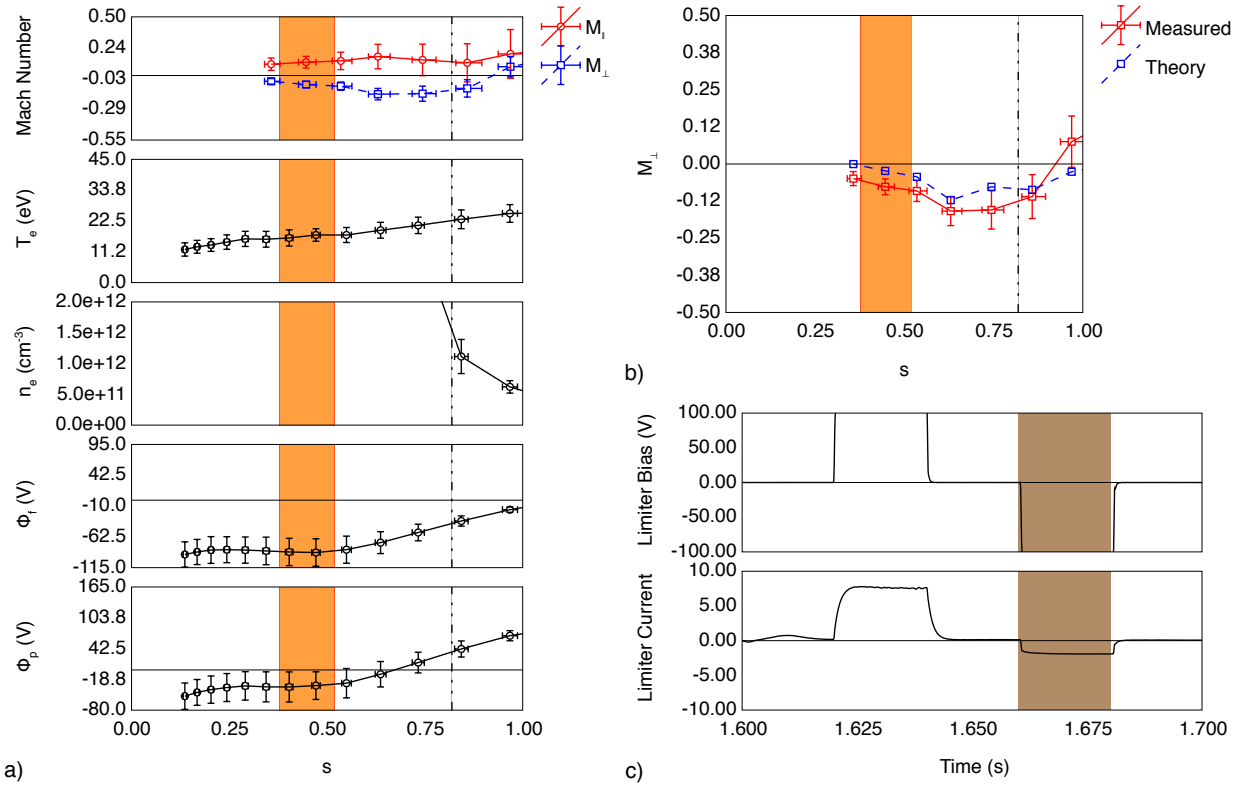

Figure 4.4: Data for experiment A from time interval 1.66 s-1.68 s. a) From Top to Bottom: Mach Number (M), Electron Temperature (T_e), Electron Density (n_e), Floating Potential (Φ_f), Plasma Potential (Φ_p). b) Measured and calculated values of $M_\perp$. c) Measured bias voltage and current. The orange shaded region represents the extent of the biasing probe tip. The vertical dashed dotted line marks the LCFS. The shaded region in the lower right corner marks the time interval that profile data is averaged over.

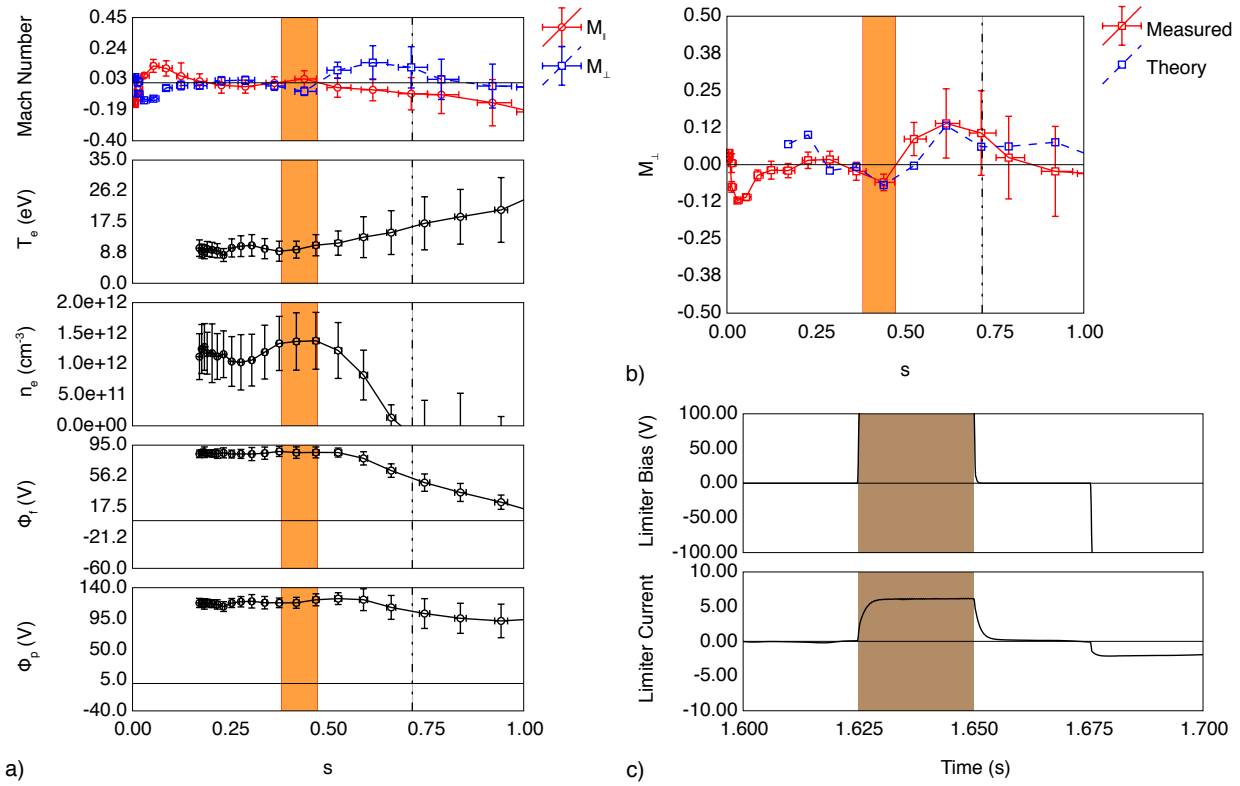

Figure 4.5: Data for experiment B from time interval $1.625\text{ s} - 1.65\text{ s}$. a) From Top to Bottom: Mach Number (M), Electron Temperature (T_e), Electron Density (n_e), Floating Potential (Φ_f), Plasma Potential (Φ_p). b) Measured and calculated values of $M_\perp$. c) Measured bias voltage and current. The orange shaded region represents the extent of the biasing probe tip. The vertical dashed dotted line marks the LCFS. The shaded region in the lower right corner marks the time interval that profile data is averaged over.

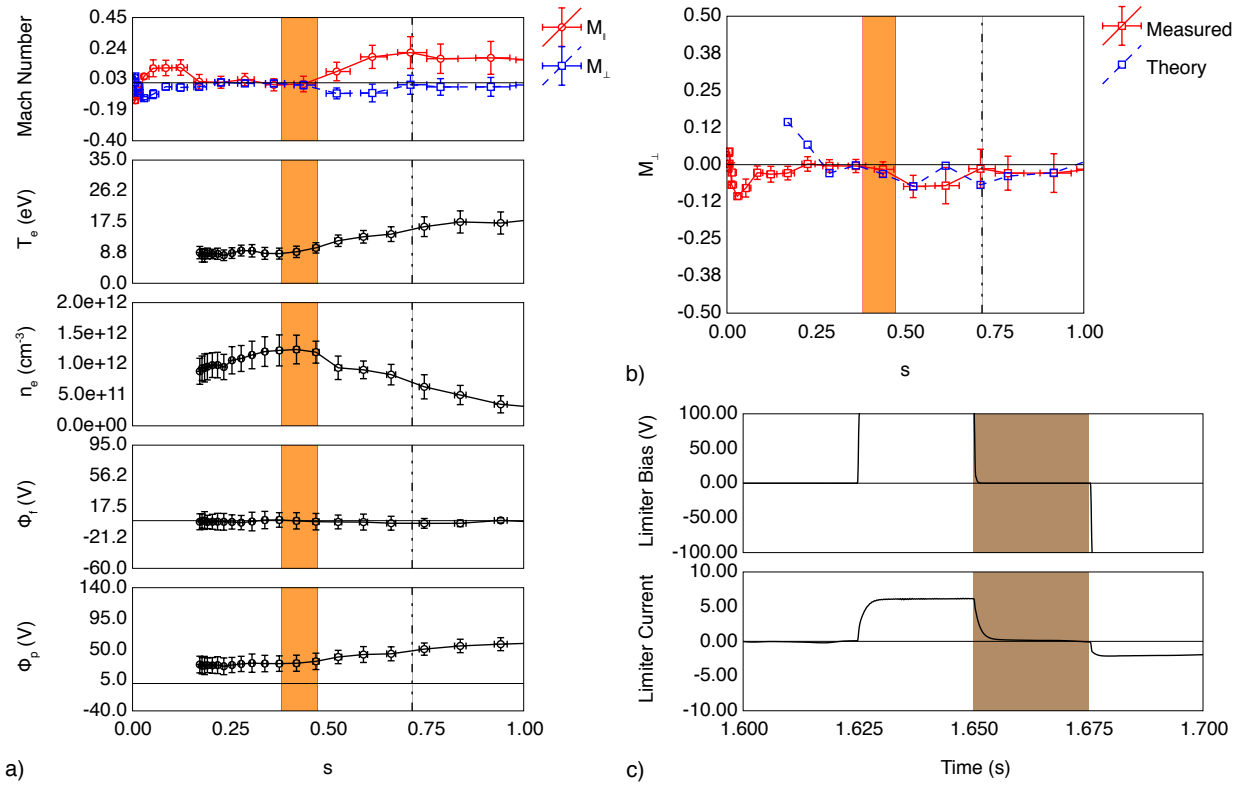

Figure 4.6: Data for experiment B from time interval $1.65\text{ s} - 1.675\text{ s}$. a) From Top to Bottom: Mach Number (M), Electron Temperature (T_e), Electron Density (n_e), Floating Potential (Φ_f), Plasma Potential (Φ_p). b) Measured and calculated values of $M_\perp$. c) Measured bias voltage and current. The orange shaded region represents the extent of the biasing probe tip. The vertical dashed dotted line marks the LCFS. The shaded region in the lower right corner marks the time interval that profile data is averaged over.

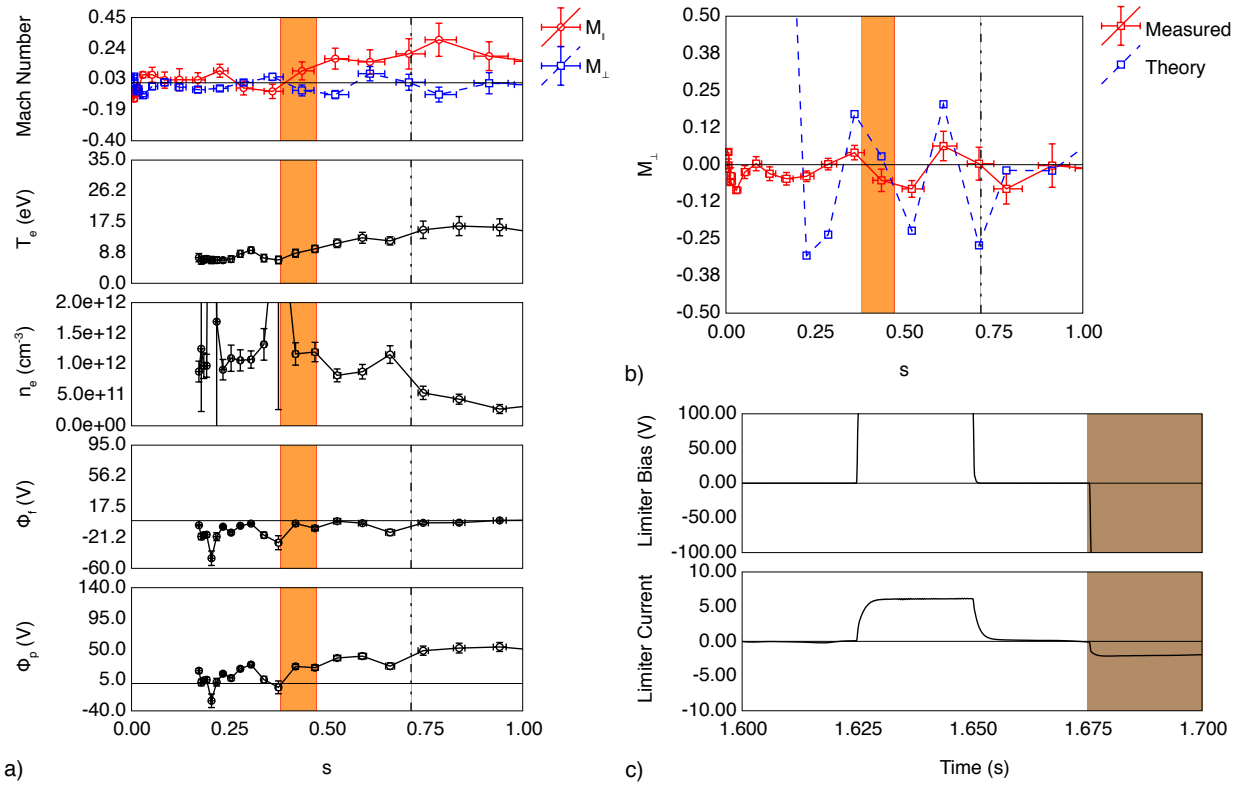

Figure 4.7: Data for experiment B from time interval $1.675s - 1.7$ s. a) From Top to Bottom: Mach Number (M), Electron Temperature (T_e), Electron Density (n_e), Floating Potential (Φ_f), Plasma Potential (Φ_p). b) Measured and calculated values of $M_\perp$. c) Measured bias voltage and current. The orange shaded region represents the extent of the biasing probe tip. The vertical dashed dotted line marks the LCFS. The shaded region in the lower right corner marks the time interval that profile data is averaged over.

Electric fields are established by gradients in the plasma potential (Φ_p). For positive biases, figures 4.2a and 4.5a, experiment A was not able to establish an electric field. The plasma potential Φ_p profiles (a) bottom plot) show a flat profile. By contrast, experiment B does generate a significant electric field. For 0 V biases, it is expected that there should be no electric fields since the biasing probe is fixed at the same potential as the CTH vacuum vessel. Φ_p profiles remain flat for both experiments as seen in figures 4.3a and 4.6a. Negative biases, figures 4.4a and 4.7a, show the opposite effect that positive biases show. In Experiment A, negative biases produce a radially inward (negative) electric field. In Experiment B, negative biases could not produce a significant electric field.

One fundamental difference between experiments A and B is the amount of ECRH heating power used. In Experiment B, the electron temperature (a; 4th plot from the bottom) is lower. On average, electron temperatures in the core of the plasma were $T_e \sim 15$ eV for Experiment A and $T_e \sim 10$ eV for Experiment B. While this is not unexpected due to the reduced inout heating power, results show that lower electron temperatures play a pivotal role in ability to produce an electric field direction. In the high electron temperatures of experiment A, radially inward or negative electric fields were produced under negative biasing. Significant radially outward or positive electric fields could not be produced by positive biasing. By contrast in the lower electron temperatures of experiment B, the opposite occurs. A positive electric field was produces from positive biasing. However, a significant negative electric field could not be produced from negative biasing. In either case, induced gradients in Φ_p are localized between the biasing limiter tip and the scrape off layer.

4.3 Ion Flows

Flows in CTH should arise from two sources, intrinsic flows present in the plasma and flows arising from edge biasing. The Gundestrup Probe, introduced in Section 3.4.2, can measure the presence of flows both parallel and perpendicular to the magnetic field lines. It is expected that electric fields induced from edge biasing will modify the perpendicular flows.

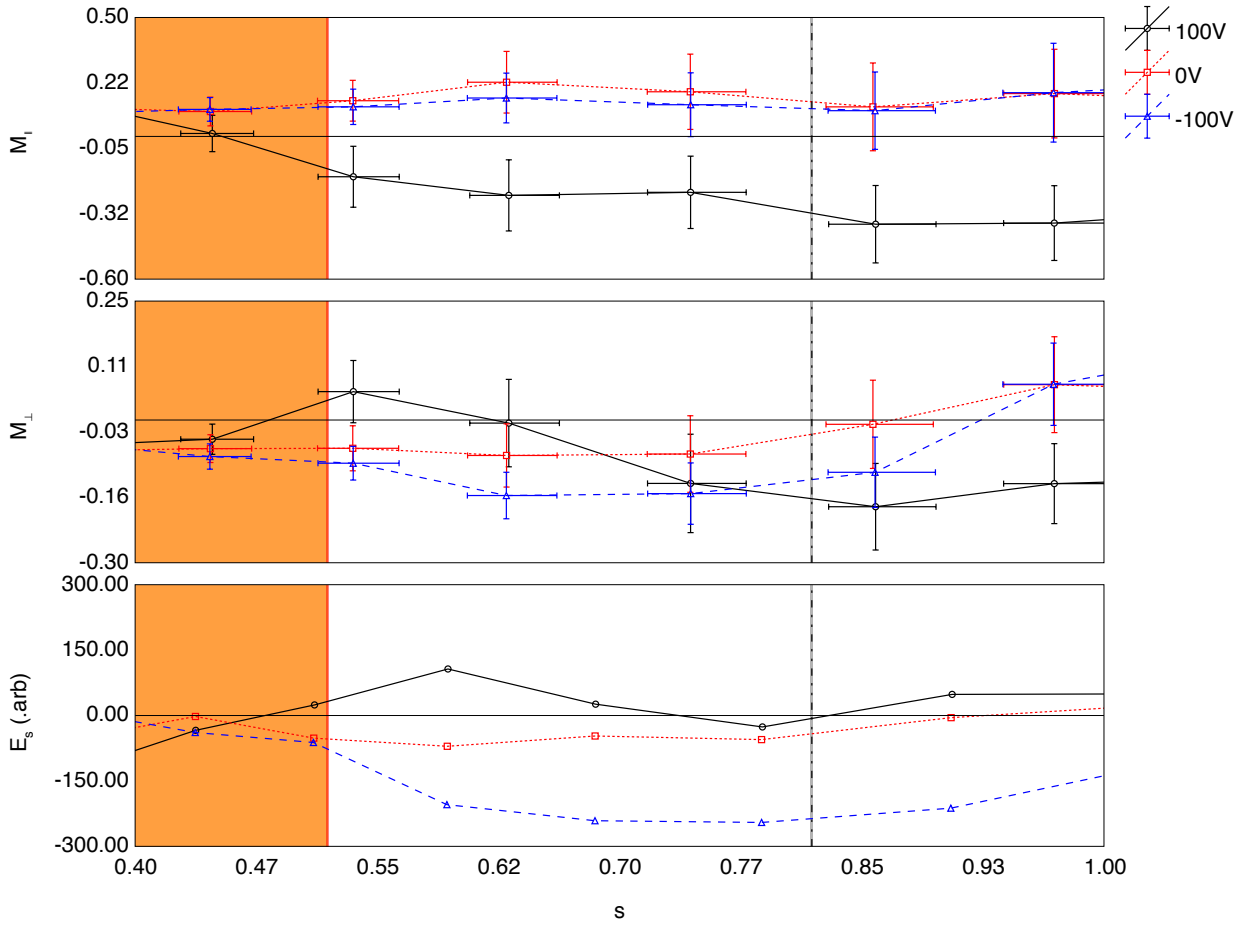

Figure 4.8: Plot comparing flux surface space electric field (E_s) with measurements of parallel and perpendicular Mach number for experiment A.

As shown in Section 4.2, the 0 V case of both presented experiments does not show the presence of a significant edge electric field. This provides a good baseline from which to compare the extent to which the application of a positive or negative bias leads to the generation of an electric field. Furthermore, it will be determined whether the presence of this electric field leads to a modification of the perpendicular flow in the plasma that is localized to the region where the gradient in the plasma potential is greatest. Cases that show the generation of edge electric fields, should show a modification of the perpendicular flow localized to the gradient region of the plasma potential Φ_p.

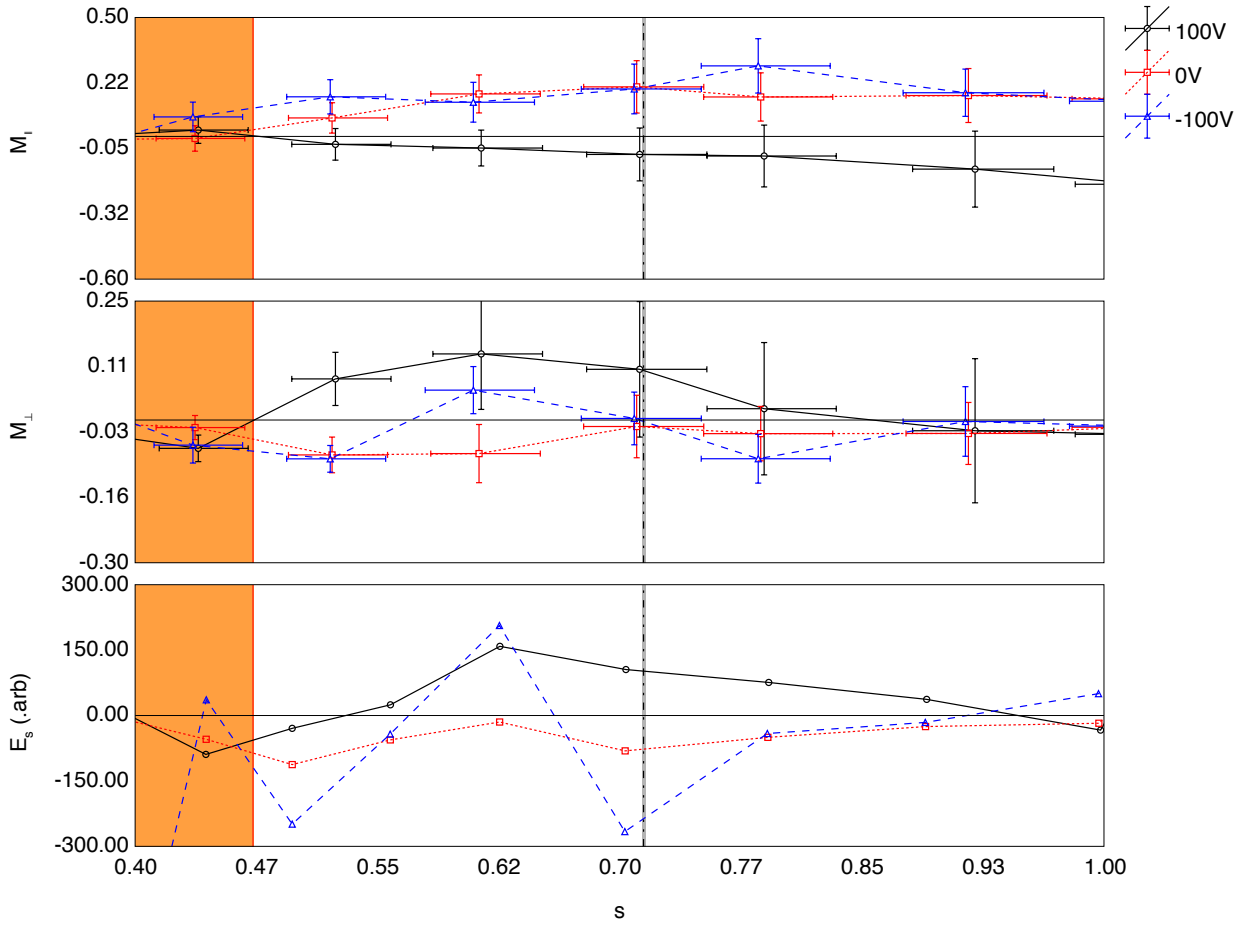

Figure 4.9: Plot comparing flux surface space electric field (E_s) with measurements of parallel and perpendicular Mach number for experiment B.

Figure 4.8 compares the flux surface space electric field (E_s) compared to the measured parallel and perpendicular Mach numbers for experiment A. For the 0 V case (dotted red line, open boxes), the perpendicular Mach number is near zero corresponding to a nearly zero electric field. Plasma flows in this case are dominated by parallel flows. By comparison to the positive bias case (solid black line, open circles), the parallel flow now reverses direction. Perpendicular flows show a negative flow in the scrape off layer however, perpendicular flows do not correspond well to measured electric fields. For the negative bias case (dashed blue line, open triangles), shows a significant negative perpendicular flows corresponding to a negative electric field. Parallel flow remains unaltered from 0 V case.

Figure 4.9 compares the flux surface space electric field (E_s) compared to the measured parallel and perpendicular Mach numbers for experiment B. For the 0 V case (dotted red line, open boxes), the perpendicular Mach number is near zero. Plasma flows in this case are dominated by parallel flows. In comparison to the positive bias case (solid black line, open circles), the parallel flow now reverses direction. Perpendicular flows show a significant positive flow corresponding to a positive electric field. The negative bias case (dashed blue line, open triangles) shows parallel flows mainly unaltered from 0 V case. The perpendicular flow profile oscillates about zero corresponding to an electric field that roughly follows the same pattern.

In both experiments positive biases show a significant change in the parallel Mach number compared to their respective 0 V cases. The perpendicular flows for 0 V cases, where Φ_p profiles are flat and corresponding electric fields are near zero, show mostly no perpendicular flow. Parallel flows remain unaltered from the 0 V biases in both -100 V bias cases. The cases where there are large gradients in the Φ_p profiles, perpendicular flows velocities show a significant deviation from the 0 V case. Perpendicular flow direction corresponds well with the direction of the flux surface space electric fields.

4.3.1 Comparison With Theory

In order to interpret the ion flow measurements, the two mechanisms that contribute to the flow are considered. The first of these is the drift that arises in the plasma from the application of the electric field; i.e. the E-cross-B drift. The second of these arises from the gradient in the plasma pressure which is the diamagnetic drift. Both of these effects were discussed in detail in Section 2.1. These combined drifts are solutions to the fluid equations when ignoring magnetic field gradient and curvature drifts. The Gundestrup probe measures the ion component of the fluid flow. Only the pressure gradients in the ion fluid impose a drift on the ions. Due to the cold ions, diamagnetic drift effects are small compared to E-cross-B drifts ($\sim 10\%$). As a result, it is expected that plasma flow is dominated by the $\boldsymbol{E} \times \boldsymbol{B}$ drift.

In figures 4.2b, 4.3b and 4.4b and 4.5b, 4.6b and 4.7b, total calculated drift is overlaid on top of measured perpendicular flows (right column, top plot). For cases of 0 V biases and cases where there is a significant gradient in the Φ_p profiles, experimental and calculated data show good agreement. The negative bias case of experiment B shows similar trends. In regions where the flow is negative, the electric field goes negative. In regions where the flow is positive, the electric fields is positive. However the magnitudes of electric fields produce an E-cross-B drift in excess of the measured perpendicular flow. This error may arise from the linear interpolations and finite difference methods used to calculate the electric fields. Only in the positive bias case of experiment A, do both the E-cross-B drift speed and direction disagree with measured perpendicular flows.

4.4 Instabilities

One of the key features that has often been associated with flowing plasmas in fusion devices has been the suppression of plasma instabilities[47–51]. This is in contrast to wide ranging studies in laboratory and space plasma environments in which plasma flows are often the source of free energy that gives rise to instabilities[32,52–55]. It is well-known that fusion plasmas are often in a vastly different range of parameters from typical laboratory and space plasma environments. This is an important contributor to the differences in plasma response.

However, for the experiments performed on the CTH device, the plasmas formed are generally have a low electron temperature ($T_e \sim 10$ eV) and moderate electron density ($n_e \sim 10^{18}$ m^{-3}). These conditions are comparable to many laboratory experiments. Therefore, this work reports that during the positive bias of experiment B ($t = 1.625$ s : 1.65 s), there is the generation of a low frequency oscillation. Figure 4.10, shows the oscillation on all triple probe, Gundestrup probe and biasing probe raw signals. All signals are filtered with a bandpass pass filter between 1 kHz and 3 kHz. In further investigations of this phenomena, all probe signals will be cropped and filtered in the same manner for spectral analysis. Figure 4.11 shows a fast Fourier transformation (FFT) of the Φ_f as a function of the probe position. This mode has a frequency of $f \sim 2$ kHz.

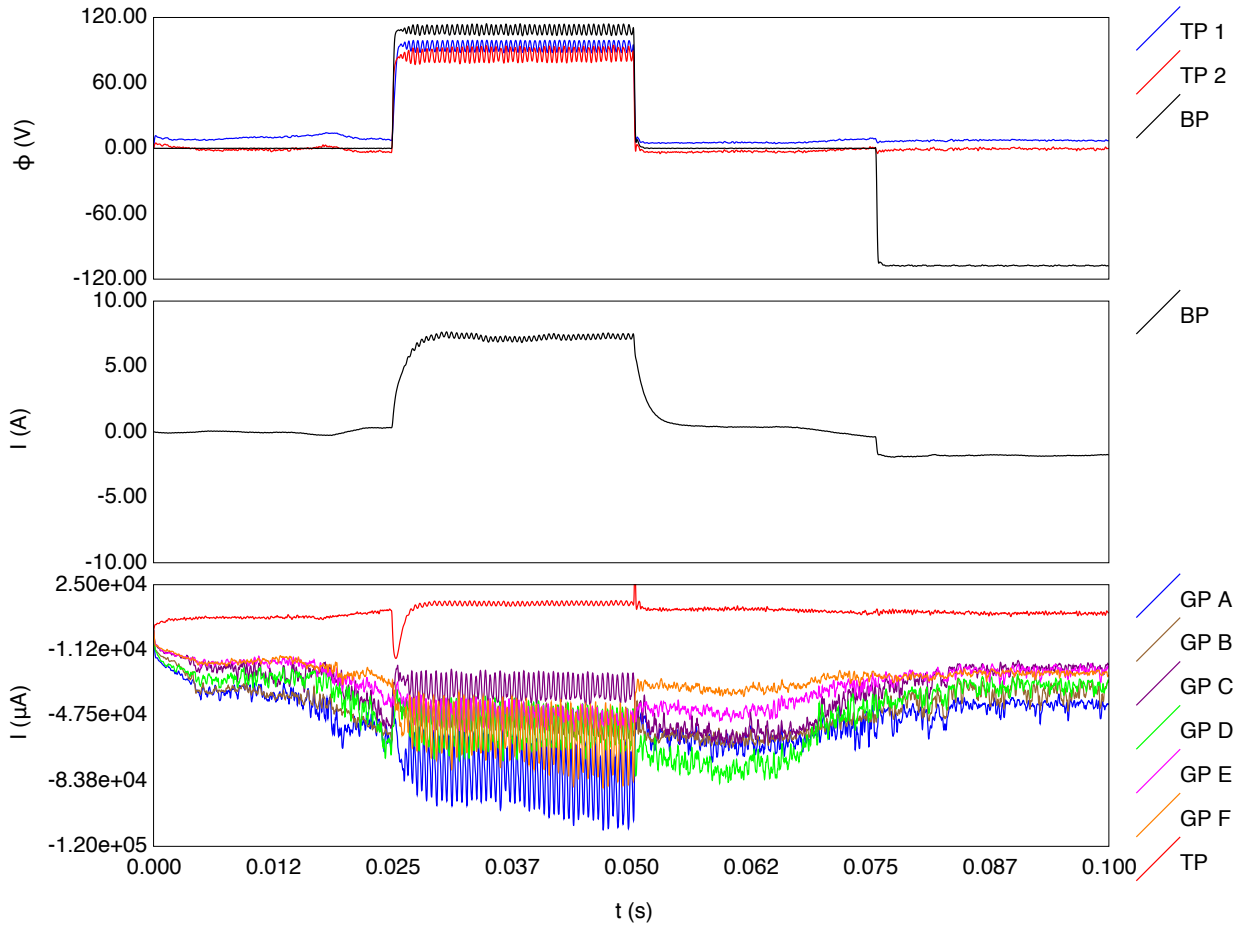

Figure 4.10: Raw voltage and current signals on all triple probe (TP), Gundestrup probe (GP) and biasing probe (BP) channels for shot number 11090836.

There is a broad spectrum of instabilities in the presence of sheared flows. However large categories of instabilities can be eliminated from examination of various scale sizes. Immediately, the investigation is limited to electrostatic branches only arising from the low value of β. Ganguli et. al.[30] provides a hierarchy of electrostatic instabilities associated with the presence of flows parallel and perpendicular to magnetic field lines. This, however, is not an exhaustive list of instabilities but does provide guidance in narrowing down the broad spectrum of instabilities. From Gundestrup probe measurements, this instability appears when there is a significant perpendicular flow induced and parallel flow is suppressed. As a result, investigations of this instability will focus on transverse flow-driven instabilities.

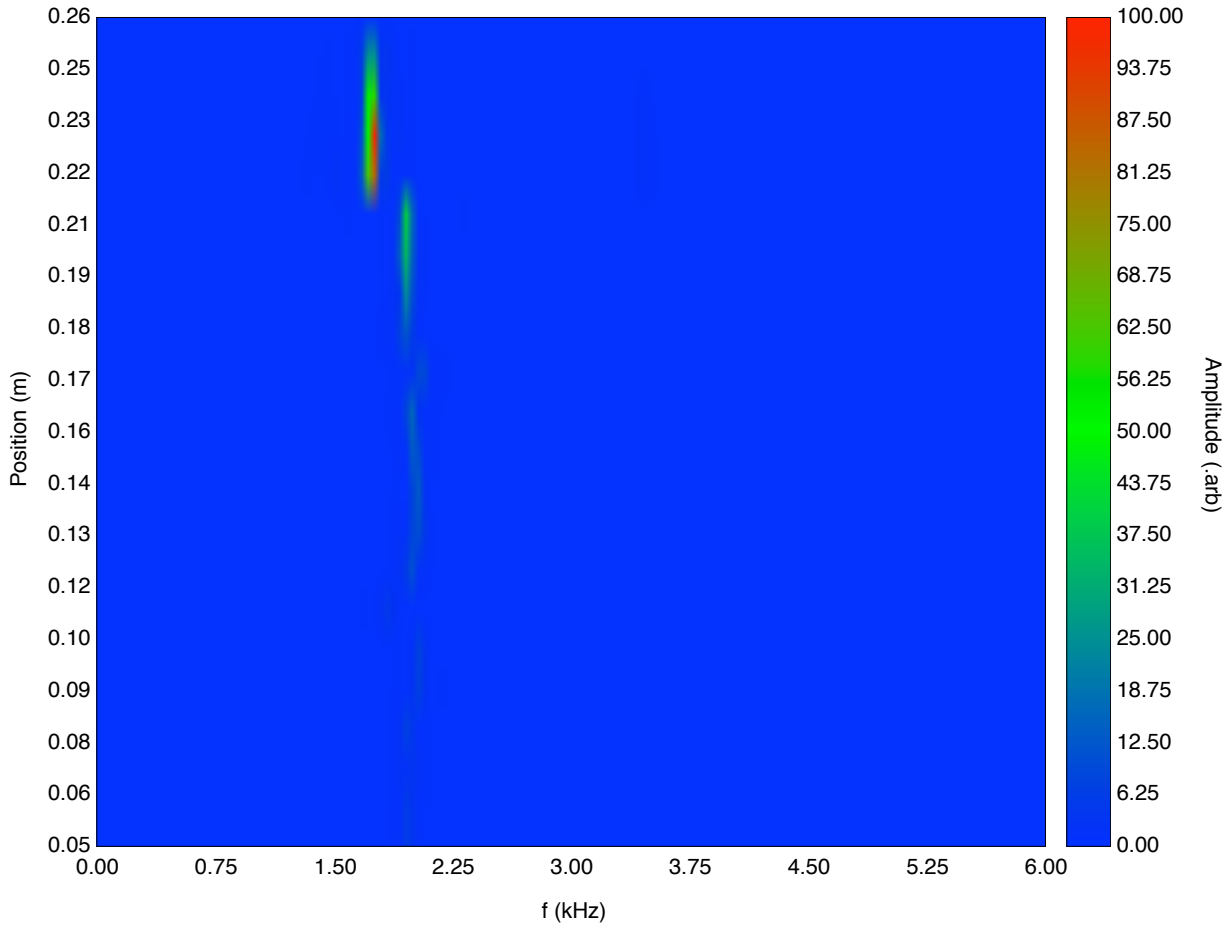

Figure 4.11: Plot of fluctuation spectrum from Φ_f measured from the triple probe under positive bias.

This instability is further parameterized by the ratio of the mode frequency compared to the ion cyclotron frequency. In the CTH device, the ion cyclotron frequency is $f_{ci} \sim 10$ MHz and the observed instability frequency is $f_l \sim 2$ kHz where $\omega = 2\pi f \sim 12.6$ kHz such that $\omega_r \ll \Omega_{ci}$. However, with the presence of an electric field and induced perpendicular flow, the observed frequency in the laboratory frame is likely to be Doppler shifted. For measured flows, and reasonable wavelengths, it is anticipated that the mode frequency will satisfy the condition $\omega_r \ll \Omega_{ci}$. As a result, the investigation of possible instabilities will be limited to low frequency modes.

This regime is also characterized by the scale length of the potential gradient size to the ion Larmor radius ($L \gg \rho_i$). For the positive bias of experiment B, the density and potential gradients,

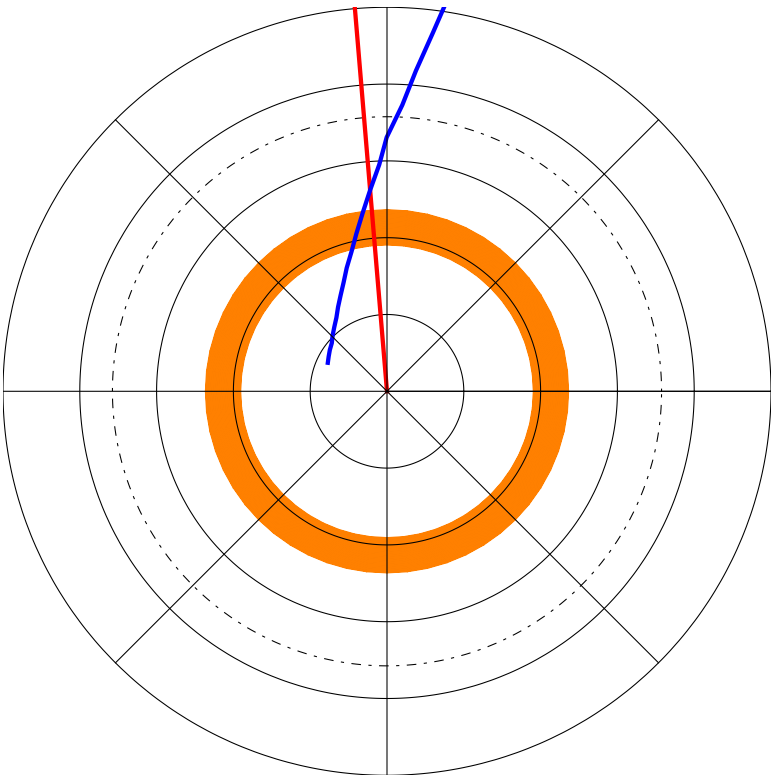

Figure 4.12: Plot of triple probe path(Blue line) in flux surface space. The red line draws a radial path from one point in the triple probe path. The orange ring shows the position of the biasing probe and the dashed-dotted line shows the location of the LCFS.

are located between the LCFS and the Biasing probe tip $L \sim 3$ cm. From Table 3.1, $\rho_i \sim 0.2$ mm, the condition of $L \gg \rho_i$ is also applicable.

In this regime, some common possible low frequency modes include, Kelvin-Helmholtz[30,56–58], Rayleigh-Taylor or interchange modes[57,58], drift waves[30,58,59] and ion acoustic waves[30,59]. Some of these modes require the presence of sheared flows as a driving mechanism while others can be stabilized or destabilized by the presence of sheared flows. To identify the possible instability, characteristics of the mode will be compared with experimental data. If possible, the dispersion relation will be solved for relevant CTH parameters to determine if that instability is likely to occur.

4.4.1 Driving Mechanism

To investigate the radial structure of the observed instability, the velocity, density and electric field gradients will be compared to the peak wave power in flux surface space at each of the Gundestrup probe positions. Peak wave power is obtained by means of taking the FFT of each probe signal and spatially locating the peak of the spectrum. Radial structure of the instability is examined by means of a cross spectral analysis. The fluctuating floating potential measurement of the triple probe is cross-correlated to the fluctuation measured on the fixed biasing probe. At each triple probe location, the cross correlation magnitude and phase difference between the triple and biasing probes are obtained. The radial phase difference is obtained by locating the phase at the maximum of the cross-correlation amplitude. The phase at the first probe position is set to be zero. The radial phase structure is accumulated from the phase difference at each probe position. It should be noted that this does not represent the true radial structure of the plasma because, as Figure 4.12 shows, the triple probe path is not radial in flux surface space.

To investigate possible driving mechanisms, profiles of n_e, Φ_p and $M_\perp$ are spline interpolated in flux surface space. The derivative of each profile is taken with respect to s from the calculated piecewise spline functions to construct the flux surface gradient of these quantities. The results of this calculation are three key quantities. The first of these, the flux surface space electric field (E_s), computed from the gradient of the plasma potential (Φ_p). The density gradient in flux surface space is computed from $-\frac{\partial n_e}{\partial s}$. Finally the flux surface space shear frequency is competed from $\omega_s = \frac{\partial}{\partial s} M_\perp$. These quantities are not the same as their laboratory space counterparts, however they are instructive for comparing with the spatial profile of the wave power with these various quantities.

Figure 4.13 shows a comparison of (from bottom to top) the wave power for each Gundestrup probe tip, the radial phase difference of the triple probe Φ_f cross correlated to the biasing probe potential, ω_s, $-\frac{\partial n_e}{\partial s}$ and E_s. Wave power is peaked between the biasing probe tip and the LCFS. Since wave power disappears inboard of the biasing probe, further investigations will concentrate on the region from the biasing probe to the scrape off layer.

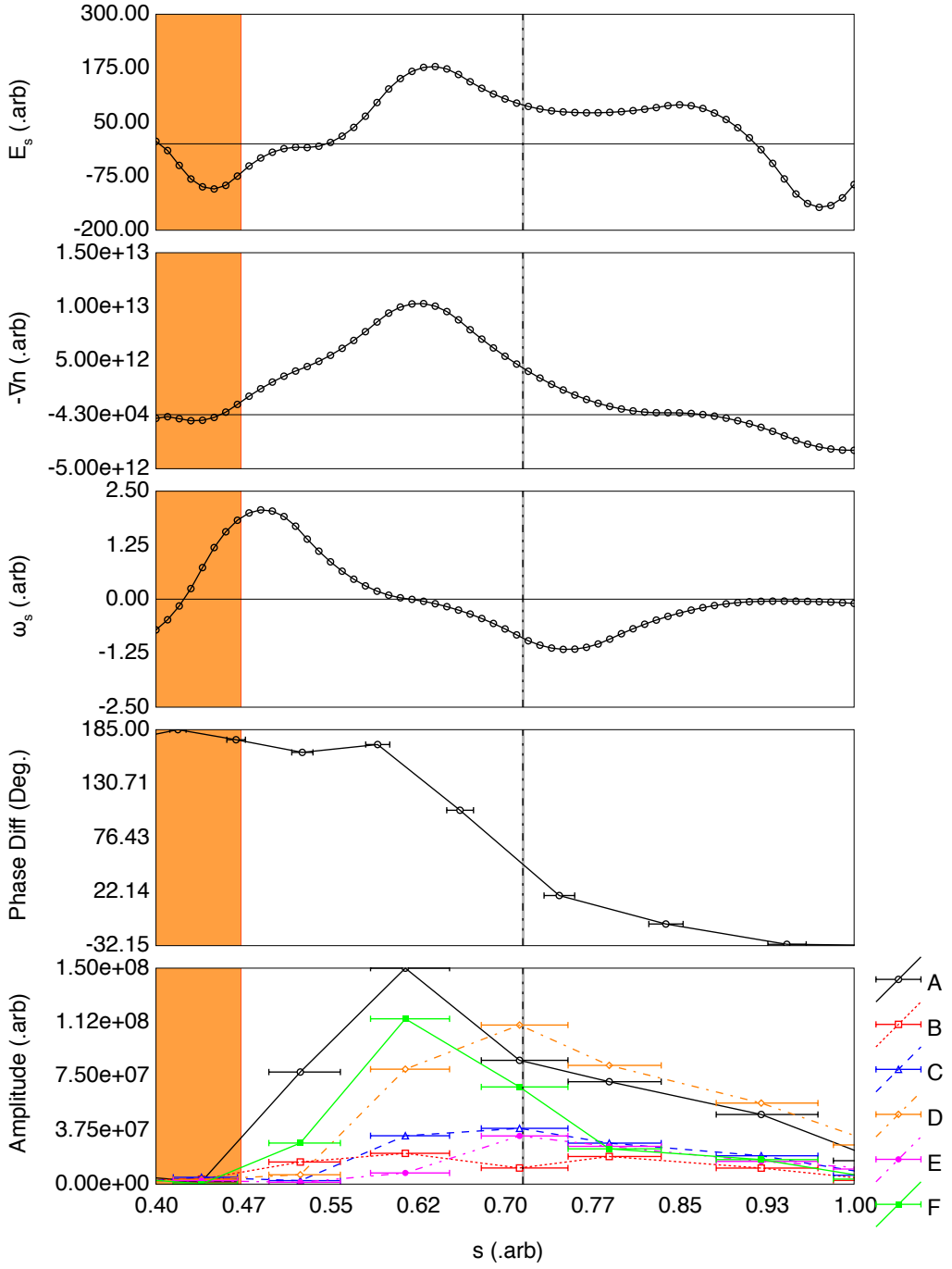

Figure 4.13: Plot comparing measured radial wave power to potential, density, and velocity gradients in flux surface space under a positive bias. Starting from the top, flux surface space electric field (E_s) measured from the gradient in the plasma potential (Φ_p), flux surface space density gradient $\left(-\frac{\partial n_e}{\partial s}\right)$, flux surface space shear frequency $\left(\frac{\partial M_\perp}{\partial s}\right)$. Peak wave power is measured from an FFT of I_{sat} collected on each Gundestrup probe tip labeled A-F.

First, we must rule out the possibility of this fluctuation coming from probe measurement circuity. If this oscillation was present on the common ground of all probe measurement circuits, it would be expected that all probe measurement fluctuations would be in phase. Radial profiles of the phase change of the Φ_f show a radial structure of the phase. Furthermore, the change in phase is correlated to the peak in the fluctuation power. This provides good evidence that this is most likely a plasma effect.

The perpendicular velocity shear, i.e., shear frequency, ω_s, has a local extrema at the edge of the biasing probe and at the LCFS as shown in Figure 4.13. Profiles of perpendicular Mach number (Figure 4.5), show the induced flow is localized between the biasing probe tip and the LCFS. Perpendicular flows inboard of the biasing probe and in the scrape off layer are generally quite small. Peak wave power is not strongly correlated with the peaks in the shear frequency. This is indicative that velocity shear maybe an unlikely driving mechanism of this instability. The peak of the wave power, however is correlated with the maxima in density gradients and electric fields. This may be indicative of a drift wave or Rayleigh-Taylor instability[58] or some intermediate mode in-between.

4.4.2 Wavenumber

The next step in identifying, possible modes, is the identification of the wavenumber $\boldsymbol{k}$. Unfortunately, due to lack of diagnostics, a true $\boldsymbol{k}$ measurement cannot be directly obtained. However, insights into the wavenumber may be obtained from an examination of the first order velocity fluctuations. Figure 4.14 shows the fluctuations in $M_{\parallel}$ and $M_{\perp}$ for a single data shot. At each data point of measured saturation current, $M_{\perp}$ and $M_{\parallel}$ are obtained as a function of time.

By averaging over this region, the zeroth order flows can be calculated as described in Section 4.3. The radial plasma flow is assumed to be diffusive in nature and small compared to induced parallel and perpendicular flows. In order to understand zeroth order flow direction, the zeroth

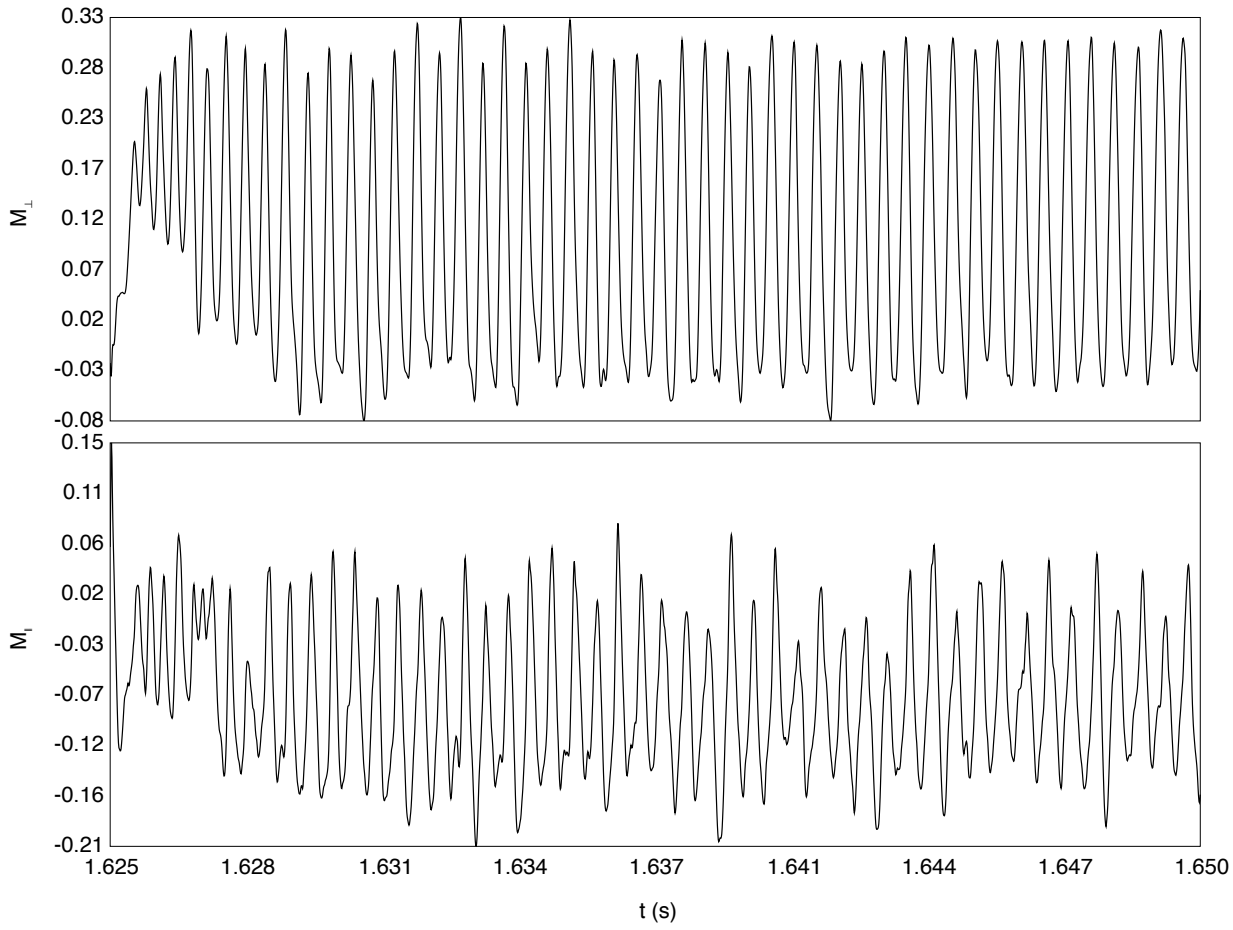

Figure 4.14: Fluctuations in the measured in $M_\perp$ and $M_\parallel$ flows.

order flow is separated into its unit vector components using;

$$\hat{\boldsymbol{m}}_{0\parallel} = \frac{M_\parallel}{\left(M_\parallel^2 + M_\perp^2\right)^{\frac{1}{2}}} \tag{4.2a}$$

$$\hat{\boldsymbol{m}}_{0\perp} = \frac{M_\perp}{\left(M_\parallel^2 + M_\perp^2\right)^{\frac{1}{2}}} \tag{4.2b}$$

For first order velocity fluctuations, $M_\parallel$ and $M_\perp$ are filtered with the same band pass filter used in earlier in this section. Power spectra for the parallel and perpendicular flows are measured from the time series of Gundestrup probe data. First order Fourier amplitudes are located from the

peak in the power spectra. Fourier amplitudes are normalized to first order unit vectors using

$$\hat{\boldsymbol{m}}_{1\parallel} = \frac{M'_{\parallel}}{\left(M'^2_{\parallel} + M'^2_{\perp}\right)^{\frac{1}{2}}} \tag{4.3a}$$

$$\hat{\boldsymbol{m}}_{1\perp} = \frac{M'_{\perp}}{\left(M'^2_{\parallel} + M'^2_{\perp}\right)^{\frac{1}{2}}} \tag{4.3b}$$

where M' represents the Fourier transformed amplitudes.

Figure 4.15 shows the measured flow direction of zeroth and first order Mach numbers normalized to unit vectors. In general, zeroth order flows are mostly perpendicular to the magnetic field direction. The same holds true for the first order velocity fluctuations as well. At the peak of the wave power for the A, B and F collecting plates, the first order velocity fluctuation are nearly completely perpendicular. This indicated that the parallel wavenumber $k_{\parallel}$ is small or nearly zero indicating either long wavelengths or no propagation along the field lines.

4.4.3 Dispersion relations

To determine an instability mode requires a measurement of the dispersion relation. Normally, this is achieved by measuring the $\boldsymbol{k}$ at various mode frequencies. A typical way of measuring the wavenumber of an electrostatic mode is by measuring the phase difference between two probe tips. However, an estimate of the expected wavelength is required a-priori to insure proper probe tip spacing. If the probe tips are spaced too far apart, multiple wavelengths can occur between the tips. If the tips are spaced two close together, the relative phase shift measured can be too small to detect.

For flow studies on CTH, it was not known what the effects of edge biasing would produce. A diagnostic measurement of $\boldsymbol{k}$ could not be performed until a possible wave mode is identified. It is possible however to identify possible wavenumbers through modeling known plasma instabilities constrained by experimental observations. When possible, the dispersion relation will be solved

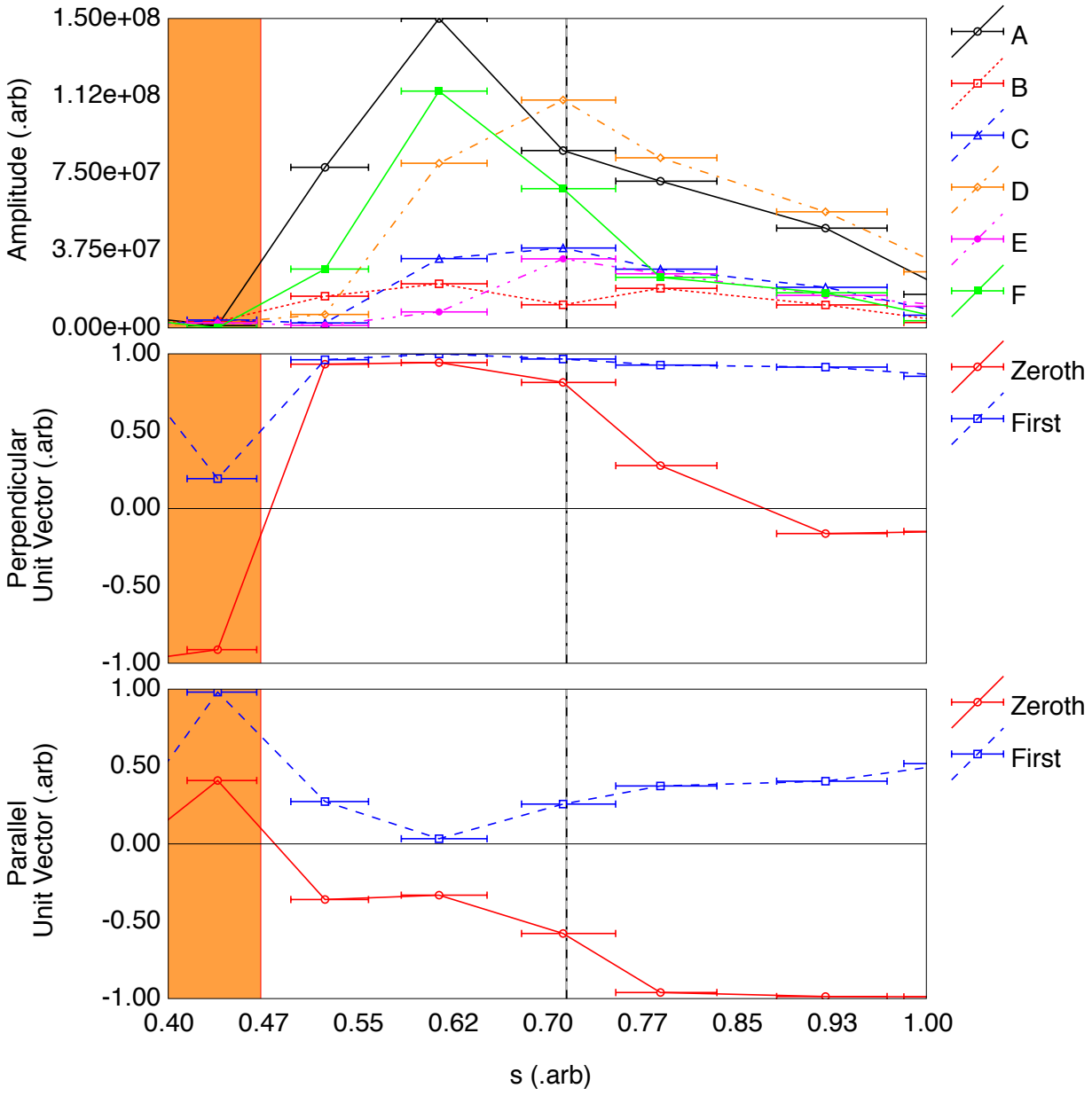

Figure 4.15: Plot comparing the parallel and perpendicular components of the zeroth and first flow unit vectors to the peak wave power as a function of flux surface space s coordinate. Peak wave power is measured from an FFT of I_{sat} measured from each of the Gundestrup probe tips. Peak wave power corresponds to the region where zeroth and first order flow directions are perpendicular to the magnetic field direction.

directly or $\boldsymbol{k}$ will be estimated from a model of the dispersion relation. The calculated values of $\boldsymbol{k}$ are subject to two limits.

1. Wavenumbers must correspond to wavelengths that fit within the CTH vacuum vessel.

2. Wavenumbers must correspond to wavelengths that are larger than the size of a probe measurement tip.

For the first limit, if it is assumed that the vacuum vessel acts like a waveguide, the poloidal or toroidal circumference of the chamber would constrain the maximum wavelength. For the second limit, if the wavelength was smaller than the probe tip, the probe would not be able to measure a fluctuation because the that fluctuation would average out over the length of the probe. Using these limits and the dispersion relation calculations, the wavelength will be determined from the k value corresponding to the measured mode frequency. Possible instability modes will be accepted or rejected based on values of k that fall within these constraints.

For the ion acoustic and drift wave modes the models for frequency and growth rate provided by Swanson[59] will be used. For the Kelvin-Helmholtz we can solve the dispersion relation directly[30,57] using a shooting method described in section 2.3.1. For the dispersion relation incorporating all the features measured in the CTH plasma, we will solve the wave function provided by Guzdar et. al.[57] using the same shooting method. Parameters and values that will be used are defined in Table 4.3. For simplicity, the plasma will be modeled using a slab geometry. Density and potential profiles will be modeled as

$$n_0(x) = 7.45 \times 10^{17}\ \mathrm{m}^{-3} \tanh\left(\frac{x}{L}\right) + 7.55 \times 10^{17}\ \mathrm{m}^{-3} \tag{4.4}$$

$$\phi_0(x) = 17\ \mathrm{V} \tanh\left(\frac{x}{L}\right) + 90\ \mathrm{V} \tag{4.5}$$

to qualitatively match the profiles measured in CTH. In the slab geometry $\boldsymbol{B}$ is assumed to point in positive $\hat{\boldsymbol{z}}$. To match the direction of gradients relative to $\boldsymbol{B}$ with respect to CTH, the plasma core is assumed to be at positive x and the scrape off layer is assumed to be at negative x.

Name	Symbol	Definition
Charge	e	$1.6 \times 10^{-19} c$
Permittivity of Free Space	ϵ_0	8.9×10^{-12} Fm^{-1}
Magnetic Field	B	$0.5T\hat{\boldsymbol{z}}$
Scale Length	L	0.03 m
Ion Mass	m_i	1.7×10^{-27} kg
Electron Mass	m_e	9.1×10^{-31} kg
Ion Temperature	T_i	1 eV
Electron Temperature	T_e	10 eV
Ion Thermal Velocity	v_i	$\sqrt{\frac{3.2 \times 10^{-19} T_i}{m_i}}$
Electron Thermal Velocity	v_e	$\sqrt{\frac{3.2 \times 10^{-19} T_e}{m_e}}$
Ion Acoustic Speed	c_s	$\sqrt{\frac{1.6 \times 10^{-19} T_e}{m_i}}$
Density	$n_0(x)$	Equation 4.4
Potential	$\phi_0(x)$	Equation 4.5
$\boldsymbol{E} \times \boldsymbol{B}$ Drift	$v_0(x)$	$\frac{\Phi_0'(x)}{B}$
Electron Debye Length	$\lambda_{De}(x)$	$\sqrt{\frac{\epsilon_0 1.6 \times 10^{-19} T_e}{n_0(x) e^2}}$
Ion Cyclotron Frequency	Ω_{ci}	$\frac{eB}{m_i}$

Table 4.3: Various parameters and definitions used for solving the dispersion relations for various instability modes.

Ion Acoustic

For the ion acoustic wave, the frequency and growth rate are defined to be

$$\omega_r^2 = \frac{k^2 c_s^2}{1 + k^2 \lambda_{De}^2} \left[1 + \frac{3T_i}{T_e} \left(1 + k^2 \lambda_{De}^2 \right) \right] \tag{4.6}$$

and

$$\frac{\omega_i}{\omega_r} = -\frac{\sqrt{\pi} \zeta_{ir}^3}{1 + 3\zeta_{ir}^{-2}} \left(\exp\left(-\zeta_{ir}^2\right) + \frac{T_i v_i}{T_e v_e} \right) \tag{4.7}$$

where $\zeta_{ri} = \frac{\omega_r}{k v_i}$. The growth rate for the ion acoustic wave is negative ($\omega_r < 0$) implying this mode is damped. Without a driving mechanism external to the plasma, this mode will not exist.

This condition does not immediately rule out this mode as an external driving source is possible. The ion acoustic mode does not take into account the possibility of flow. For application to CTH, it will be assumed that if this mode exists, that it is a rotating mode whose frequency ω_r is given by $\pm 2\pi f_l + k v_0(x)$.

Solving for both positive and negative branches for the wavelength measured frequency. The positive branch gives a $k = 0.37$ m^{-1} converted to wavelength is $\lambda = 17$ m. The negative branch gives a $k = 0.35$ m^{-1} converted to wavelength is $\lambda = 18$ m. With a minor radius of 0.26 m these wavelengths are too big to fit in the CTH vacuum vessel radially and poloidally. The CTH major radius $R_0 = 0.75$ m giving the center of the vacuum vessel a circumference of 4.71 m. If the wave was traveling purely toroidally, the CTH vacuum vessel would be too small to contain this wave mode. However, there is the possibility of the wave traveling along a field line. The length of a field line can be longer than the circumference of the vacuum vessel. To estimate the smaller value of k that can fit the CTH magnetic field, define $k_\parallel = \frac{n\bar{\iota}}{R_0}$ where n is the toroidal mode number and $\bar{\iota}$ is the rotational transform. Typical ECRH plasmas in CTH are performed in plasmas where $\bar{\iota}$ is between $\bar{\iota} = 0.22$ and $\bar{\iota} = 0.18$. This places the boundaries of k in CTH to be between $k_{0.22} = 0.3$ m^{-1} and $k_{0.18} = 0.24^{-1}$ which correspond to wavelength of $\lambda_{0.22} = 21$ m and $\lambda_{0.18} = 26$ m respectively. While these wavelengths are able to fit into the machine, estimates of $\hat{\boldsymbol{k}}$ show wave propagation is mostly perpendicular to the magnetic field line. Evidence presented shows that the measured instability is most likely not an ion acoustic mode.

Drift Waves

For the drift wave, the frequency and growth rate are defined to be

$$\omega_r = \omega_e^* \frac{1 - \lambda_i}{1 + k_\perp^2 \rho_s^2} \tag{4.8}$$

and

$$\omega_i = \sqrt{\pi}\omega_e^* \left(\frac{k_\perp^2 \rho_s^2}{1 + k_\perp^2 \rho_s^2} \right)^2 \left(1 + 2\frac{T_i}{T_e} \right) \tag{4.9}$$

where the drift frequency defined to be $\omega_e^*(x) = k_\perp \frac{1.6\times10^{-19}T_e}{eB}\frac{n_0'(x)}{n_0(x)}$, $\rho_s = \frac{c_s}{\omega_{ci}}$ and $\lambda_i = \frac{k_\perp^2 v_i^2}{2\Omega_{ci}}$. Similarly to the ion acoustic wave treatment, for application to CTH, it will be assumed that if this mode exists, that it is a rotating mode and ω_r is replaced by $\pm 2\pi f_l + k v_0(x)$. For $\pm f_i$ the calculated $k_\perp$ is 4 m^{-1} which corresponds to a wavelength of 1.5 m. CTH has a maximum poloidal circumference of 1.63 m. While this wavelength is on the edge of fitting within the vacuum vessel, this mode should not be dismissed entirely because Equations 4.8 and 4.9 were derived assuming a non-rotating drift wave.

The growth rate for the drift wave (Equation 4.9) is positive. This means that this is a naturally occurring instability in the presence of a density gradient. The estimated growth rate for CTH conditions and the $k_\perp = 4$ m^{-1} is on the order of $\omega_i \sim 10^{-8}$. This growth rate estimate shows a very slowly growing mode. Therefore, while the drift wave is a possible candidate, the slow growth rate make it an unlikely candidate.

Kelvin-Helmholtz

In the appropriate limits, the generalized dispersion relations presented in Ganguli, et. al.[30] and Guzdar, et. al.[57] reduce to the well known Kelvin-Helmholtz dispersion relation.

$$\frac{\partial^2}{\partial x^2}\Phi(x) - k_y^2 + \frac{k_y v_0''(x)}{\omega - k_y v_0(x)}\Phi(x) = 0 \tag{4.10}$$

For this dispersion relation we can solve this directly using the shooting method presented at the beginning of this section. Figure 4.16a shows the frequency and growth rate as a function of wavenumber. The growth rate is peaked at about $k = 30$ m^{-1} corresponding to a wavelength of $\lambda = 0.21$ m. The frequency associated with this peak is $15320\frac{\text{rad}}{\text{s}}$. Figure 4.16b shows a plot of the real and imaginary parts potential fluctuation amplitude. This is peaked at about $x = 0$, this roughly the same location as the peak in the velocity profile and is consistent with measurements of the location of peak wave amplitude (Figure 4.13). At $x = 0$, the Doppler shifted frequency

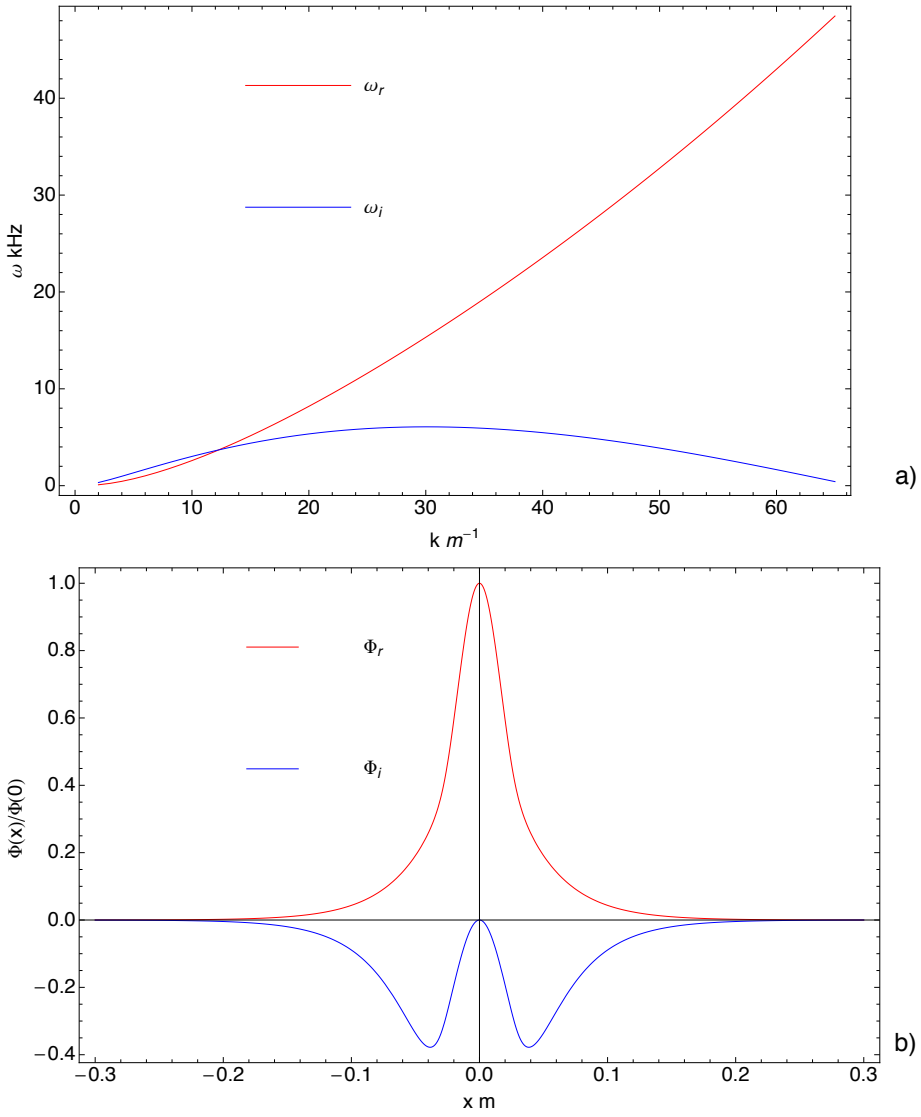

Figure 4.16: a) Frequency (ω_r) and Growth rate (ω_i) for a classical Kelvin-Helmholtz mode. b) Normalized potential fluctuation amplitude for wavelength (Φ_r) and imaginary parts (Φ_i) for the classical Kelvin-Helmholtz mode ($k = 30$ m^{-1} and $\omega = 15320 + 6075i$).

in the laboratory frame becomes $f = -3$ kHz. This frequency is within a reasonable range of the measured frequency shown in Figure 4.11.

Density Gradient Modified Kelvin-Helmholtz

Deriving the generalized dispersion relation for a density gradient modified Kelvin-Helmholtz begins by neglecting parallel wave propagation ($k_{\|} = 0$), assuming $\omega \ll \Omega_{ci}$ and the ion-neutral collision frequency $\nu_i \ll \Omega_{ci}$. The last assumption states that the ions are magnetized. Ignoring gravity and ion-neutral collisions, the general dispersion relation becomes[57]

$$\frac{\partial^2}{\partial x^2}\Phi\left(x\right) + p\left(\omega, k, x\right)\frac{\partial}{\partial x}\Phi\left(x\right) + q\left(\omega, k, x\right)\Phi\left(x\right) = 0 \tag{4.11}$$

where

$$p\left(\omega, k, x\right) = \frac{\partial}{\partial x}\ln n_0\left(x\right) \tag{4.12}$$

and

$$q\left(\omega, k, x\right) = -k^2 + \frac{k v_0\left(x\right)}{\omega - k v_0\left(x\right)}\left[\frac{1}{v_0\left(x\right)}\frac{\partial^2}{\partial x^2}v_0\left(x\right) + \frac{\partial}{\partial x}\ln v_0\left(x\right)\frac{\partial}{\partial x}\ln n_0\left(x\right)\right] \tag{4.13}$$

For this dispersion relation we can solve this directly using the shooting method presented at the beginning of this section. Figure 4.17a shows the frequency and growth rate as a function of wavenumber. The growth rate is peaked at about $k = 26\,\mathrm{m}^{-1}$ corresponding to a wavelength of $\lambda = 0.24$ m. The frequency associated with this peak is $13150\frac{\mathrm{rad}}{\mathrm{s}}$. Figure 4.17b shows a plot of the real and imaginary parts potential fluctuation amplitude. This is peaked at about $x = 0$, this is roughly the same location as the peak in the velocity profile and is consistent with measurements of the location of peak wave amplitude (Figure 4.13). At $x = 0$, the Doppler shifted frequency in the laboratory frame becomes $f = -2.6$ kHz. This frequency is within a reasonable range of the measured frequency shown in Figure 4.11. Compared to the pure Kelvin-Helmholtz mode, the presence of the density gradient narrows the instability region and decreases the growth rate.

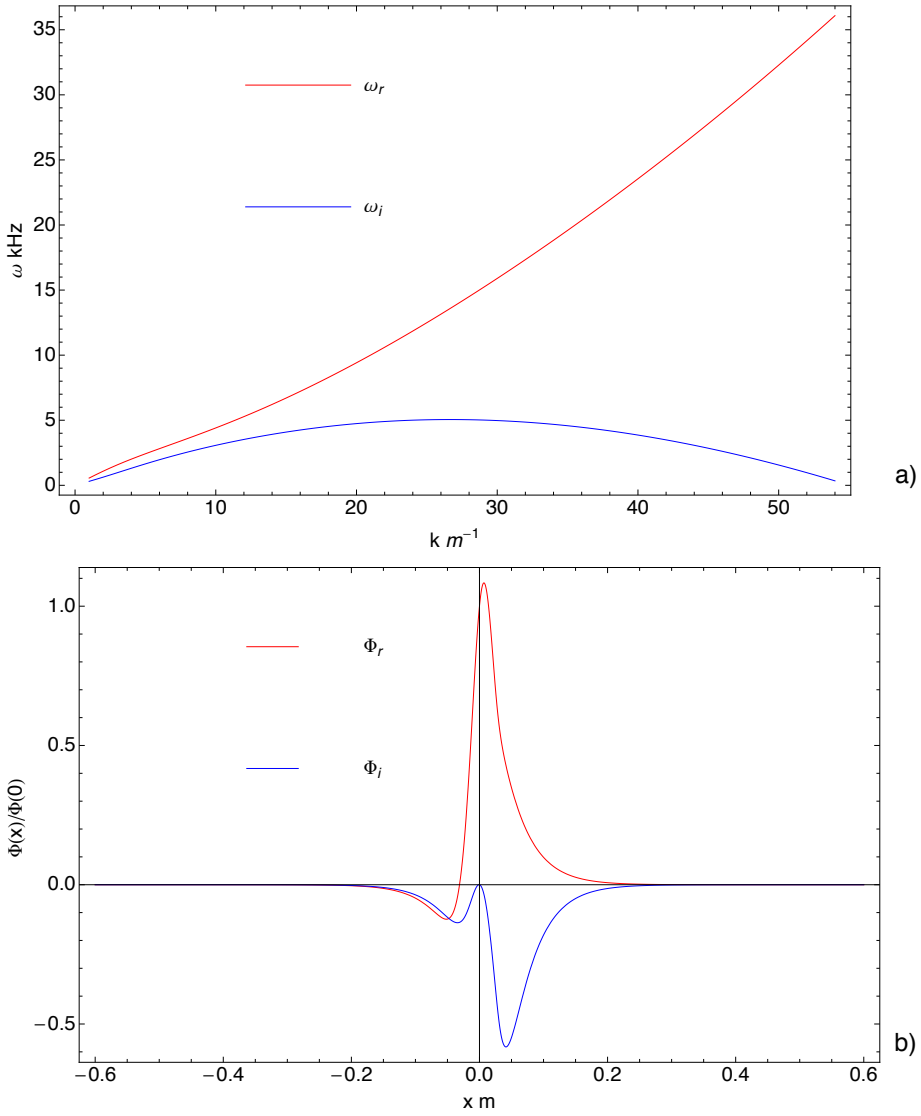

Figure 4.17: a) Frequency (ω_r) and Growth rate (ω_i) for a density gradient modified Kelvin-Helmholtz mode. The presence of density gradients narrows the regions of instability growth and decreases the growth rate compared to the pure Kelvin-Helmholtz mode. b) Normalized potential fluctuation amplitude for wavelength (Φ_r) and imaginary parts (Φ_i) for the density gradient modified Kelvin-Helmholtz mode ($k = 25$ m^{-1} and $\omega = 13150 + 5050i$).

Chapter 5

Conclusions

The study of flowing plasmas is a topic that has long been of interest to the basic, space and fusion plasma research communities. Depending upon the local plasma parameters, numerous observations have shown that these flows can have both stabilizing and destabilizing effects on plasmas. In the particular area of fusion energy research, strong plasma flows in the plasma edge are known to suppress large scale turbulence, reduce the radial transport of particles and generally provide a stabilizing influence leading to improved energy confinement in fusion devices. These effects are strongly beneficial to the long-term development of fusion as a viable energy source.

The work presented in this dissertation summarizes a series of experiments that seek to understand the role of driven plasma flows on the stability of a stellarator plasmas. While many studies of driven plasma flows in fusion devices are focused on the transition to enhanced confinement regimes (so-called, "H-modes"), it is reiterated that this is not the focus of this work. Instead, this investigation has sought to gain a more fundamental understanding of the mechanisms that can allow substantial flows to be established in the plasma, characterizing those flows, and measuring the response of the plasma to those flows.

This work is performed using the Compact Toroidal Hybrid (CTH) stellarator device operated with ECRH generated plasmas at low to moderate plasma densities ($n_e \leq 10^{18}$ m^{-3}) and low electron temperatures ($T_e \leq 15$ eV). The moderate plasma conditions these experiments were performed in allow the use in-situ probe diagnostic systems. The flow in the plasma is established by using a biased electrode to generate an electric field that is perpendicular to the magnetic flux surfaces. As a result of the application of the electric field, quasi-poloidal flows are established in the plasma. Experimental studies were performed to compare the behavior of the plasma in the presence and absence of the driven flows. A series of in situ diagnostic probes, specifically a

triple probe and a Gundestrup probe, were developed. The triple probe was used to make "instantaneous" measurements of the plasma parameters, i.e., the electron temperature, electron density, floating potential and plasma potential. The Gundestrup probe was used to make "instantaneous" measurements of the flow in the plasma.

Comparison of probe systems in the three dimensionally shaped magnetic surfaces of CTH, was made possible through the use of the equilibrium reconstruction code `VMEC`. The direct, detailed model of the magnetic field provide by `VMEC`, was critical for interpretation of probe measurements and plasma flows in the CTH device. Assumptions that certain quantities such as plasma potential and plasma pressure, are constant on a magnetic flux surface, allow localized measurements to diagnose the global structure of the plasma. Furthermore, as a result of the plasma generated with low values of beta ($\beta \sim 10^{-5}$), the vacuum magnetic flux surfaces were assumed to be unaltered by the presence of the plasma. As a result, the equilibrium reconstruction could be extended out past the normal edge of the plasma into the scrape off layer.

Figure 5.1 shows an overview of all biasing experiments performed. Electric fields are calculated between the LCFS and the Biasing Probe. Electron temperature is taken from the $z = 0.1m$ triple probe position during the zero bias time interval. The experiments performed showed that radially outward (positive) electric fields were generated using a positive bias voltage but only in plasmas with low electron temperatures ($T_e \leq 13$ eV). In plasmas with higher electron temperatures ($T_e > 13$ eV), positive bias voltages would not generate a positive electric field. By contrast, the opposite is true for radially inward (negative) electric fields. Negative electric fields were best generated when ($T_e \geq 13$ eV).

In the cases where the electric field is formed, it was noted that this electric field layer was formed between the biased electrode and the limiter making the scale-length of the electric field significantly larger than the ion Larmor radius. In particular, this fact is important to characterizing the instability that is formed in the plasma. Only in the case of the low temperature plasma with a radially outward electric field was a plasma instability observed. Under negative electric fields, the presence of a coherent plasma instability was not found.

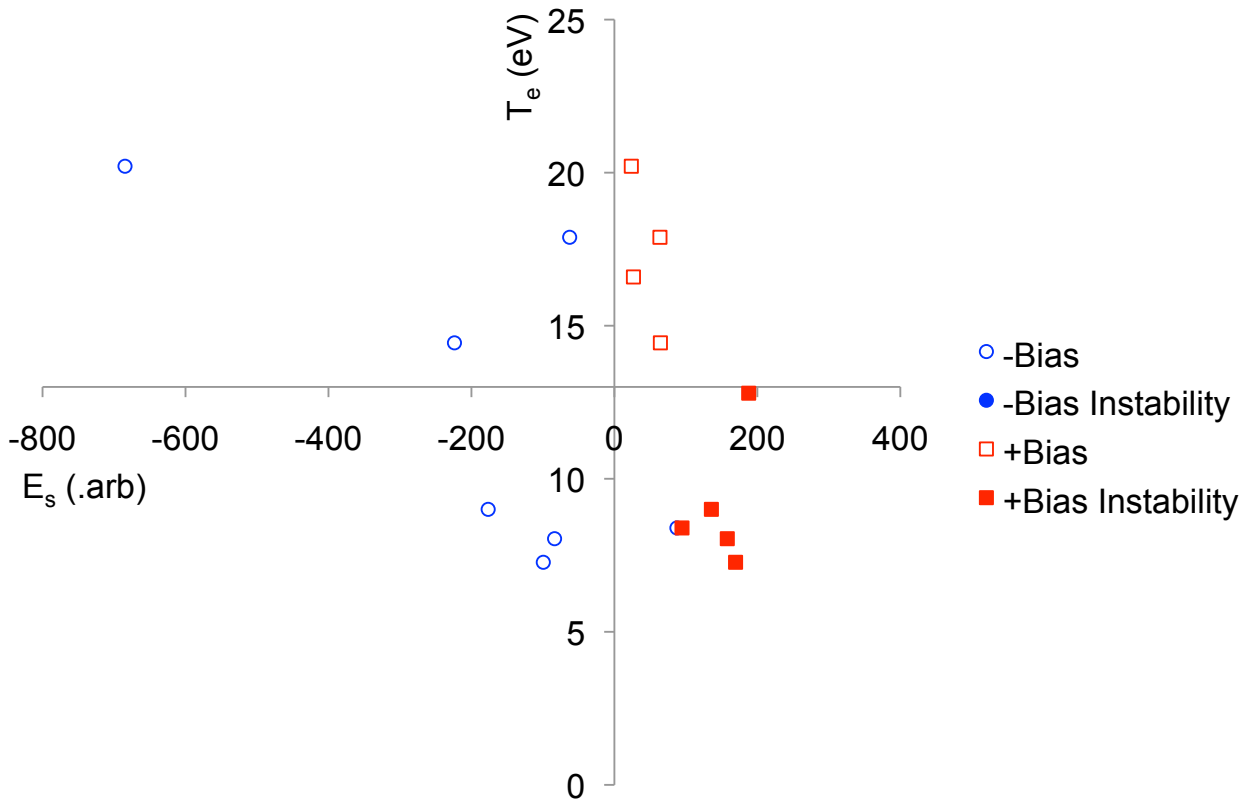

Figure 5.1: Plot shows the relationship between E_s and T_e for all positive and negative biasing experiments performed. Radially outward (positive) electric fields could not be generated above 13 eV electron temperatures. Below this threshold, positive electric fields drove instabilities. Instabilities could not be driven with negative electric fields.

Investigations of possible instability modes leads to the Kelvin-Helmholtz mode as a likely candidate. This mode is driven by the shear in the perpendicular velocity. This mode typically appears in a region where the ion gyroradius $\rho_i \ll L$ the scale size of shear layer and the mode frequency $\omega \ll \Omega_{ci}$ is much less than the ion gyrofrequency, consistent with CTH plasma conditions. When including the presence of the density gradient, the region of instability growth narrows and growth rate is reduced compared to the pure Kelvin-Helmholtz mode. However, due to the lack of a measurement of the wavenumber $\boldsymbol{k}$, a true identification of the wave mode cannot be performed. It is noted that the operating conditions for the CTH device for this work are similar to conditions found in basic laboratory type plasma experiments, so perhaps the observation of instabilities of the Kelvin-Helmholtz type are not unexpected.

5.1 Comparisons With Other Experiments

Experiments on driven flows in plasmas have been performed extensively in laboratory plasmas[31,32] and in fusion devices[33,35,60]. In many of these devices, the generation of a strong edge plasma flows and the associated transition to higher confinement regimes, is often driven by the presence of a radially inward (negative) electric field[11,17,19,48]. In these cases, the edge electric fields are self-generated from the ambipolar diffusion of ions and electrons. The work presented in this dissertation is more typical of edge biasing studies that have been performed on the TEXTOR, CASTOR, T-10 and ISTTOK tokamak experiments[33] and on the TJ-II stellarator experiment[35,60] and Compact Auburn Torsatron (CAT)[34].

5.1.1 Comparison to Tokamak Experiments

Biasing experiments on TEXTOR sought to investigate the role between E-cross-B shear and transport barrier formation. In TEXTOR, a mushroom shaped carbon limiter was inserted past the LCFS and biased to a maximum of 600 V. As the bias was increased, the edge electric field increased until a bifurcation occurred. The edge electric field jumps to a high level and density gradient is generated. A low frequency *ringing* of the plasma is developed. This is similar to results shown on CTH. By contrast, the *ringing* on TEXTOR was assumed to be caused by the biasing supply. In this work, extensive measurements show that the oscillation on CTH has a radial structure in the plasma edge. On both devices, under positive biases, a strong edge electric field is generated along with a strong density gradient and low frequency occultation induced.

Biasing experiments on CASTOR examined the sought to measure the edge E-cross-B flow and the structure of turbulence. On CASTOR instead of biasing past the LCFS, the biasing limiter was just touching the edge of the plasma and not extending into it. Flows were measured by a Gundestrup probe and compared to calculation of E-cross-B flows made from electric field measurements. The radial structure of the edge plasma flow show good agreement with E-cross-B flows with diamagnetic drifts included as well. Measurements of the turbulent structure show

a wave like mode propagating poloidally. This is similar to results obtained on CTH however, measured electric fields on CASTOR are radially inward or negative electric field.

Biasing experiments on T-10 achieved H-mode by applying a positive bias to the plasma edge. In a broad range of density and plasma current conditions, negative biases had no observable effect on plasma parameters. This is consistent with the results of biasing experiments on CTH. Measurements of electric field produced showed a strong shear electric field. At the edge of the biasing electrode, a strong radially outward (positive) electric field immediately followed by a radially inward (negative) electric field in the region between the limiter and the biasing electrode. It should be noted also be noted that in CTH, there was a broadband suppression of low frequency fluctuations during this phase of the experiment. The presence of the sheared electric fields suppressed broadband fluctuations between $3 - 30$ kHz.

An important difference between these biasing experiments and CTH is that each of the aforementioned studies were performed in tokamaks. As such, each of these experiments were are performed in plasmas with ohmic heating current and with an axisymmetric plasma. Typical densities under these conditions are $n_e \sim 10^{19}$ m^{-3} are a factor of 10 larger and core plasma temperatures are $T_e \sim 1$ keV are a factor of 100 larger than densities and temperatures on CTH under ECRH heating. As such absolute electric fields were determined from measured values of the Φ_f. Comparisons of perpendicular flows and E-cross-B flows measured from profiles of Φ_f have poor agreement as compared to E-cross-B flows measured from Φ_p. For conditions on CTH, profiles of Φ_f are a poor proxy for electric field measurements.

In TEXTOR, T-10 and CTH, the biasing electrode is inserted past the LCFS whereas on CASTOR, the bias was applied to the scrape off layer only. Experiments on ISTTOK compared both biasing regimes. It was shown that when the biasing electrode was inserted past the LCFS as performed on TEXTOR, T-10 and CTH, that positive biased produced the best correlation between enhancement of confinement and sheared E-cross-B flows. When the bias was applied to the scrape off layer only, it was found that negative biases decreased particle losses. While absolute comparison between these biasing experiments and CTH is not possible due to differences in plasma

conditions, qualitatively, results obtained on CTH show qualitative agreement with previous results obtained on tokamak edge biasing experiments.

5.1.2 Comparison to Stellarator Experiments

The forerunner to CTH was the smaller CAT device. Edge biasing experiments on CAT used a heated filament to inject current into the plasma. Typical plasma densities on CAT were $n_e \sim 10^{16}$ m^{-3}, a factor of 100 lower than CTH. Plasma temperatures were comparable to CTH conditions under ECRH at $T_e \sim 5 - 20$ eV. Rotation experiments on CAT focused on a negative biases and the generation of radially outward (negative) electric fields. Measurements of plasma flow velocity were performed with a rotatable Mach probe. Comparisons of poloidal flow measurements and E-Cross-B flow calculations in plasmas with a low neutral pressure show good agreement consistent with previous experiments and measurements performed on CTH. The rotation experiments on CAT show a consistent increase in plasma density and temperature when in the presence of edge biasing. Experiments on CTH did not show a significant change in electron temperature during biasing.

TJ-II is a stellarator with a plasma cross-section that has a "C" shape. Edge biasing experiments performed on TJ-II illustrate the ability of positive and negative electric fields to modify the plasma parameters. Under negative biasing, there is a reduction of board band turbulent fluctuations observed. Experiments on CTH qualitatively show as suppression of broadband fluctuations during positive biasing. Figure 5.2 shows the change in potential fluctuation on CTH for various biases. This is opposite of plasma response seen on TJ-II. However, plasma conditions on these devices differ. Electron temperatures and density are a factor of 10 higher in TJ-II than the values obtained in the CTH plasma. Both machines use a bias of $\Phi_{Bias} \pm 100$ V.

One fundamental difference between experiments performed on CAT and TJ-II is the addition of equilibrium reconstruction for probe measurements. On CAT, all probe measurements were performed on the mid-plane at equal field periods. Measurements on both machines do not account for the shaped nature of the magnetic fields when interpreting data. This is made necessary on CTH,

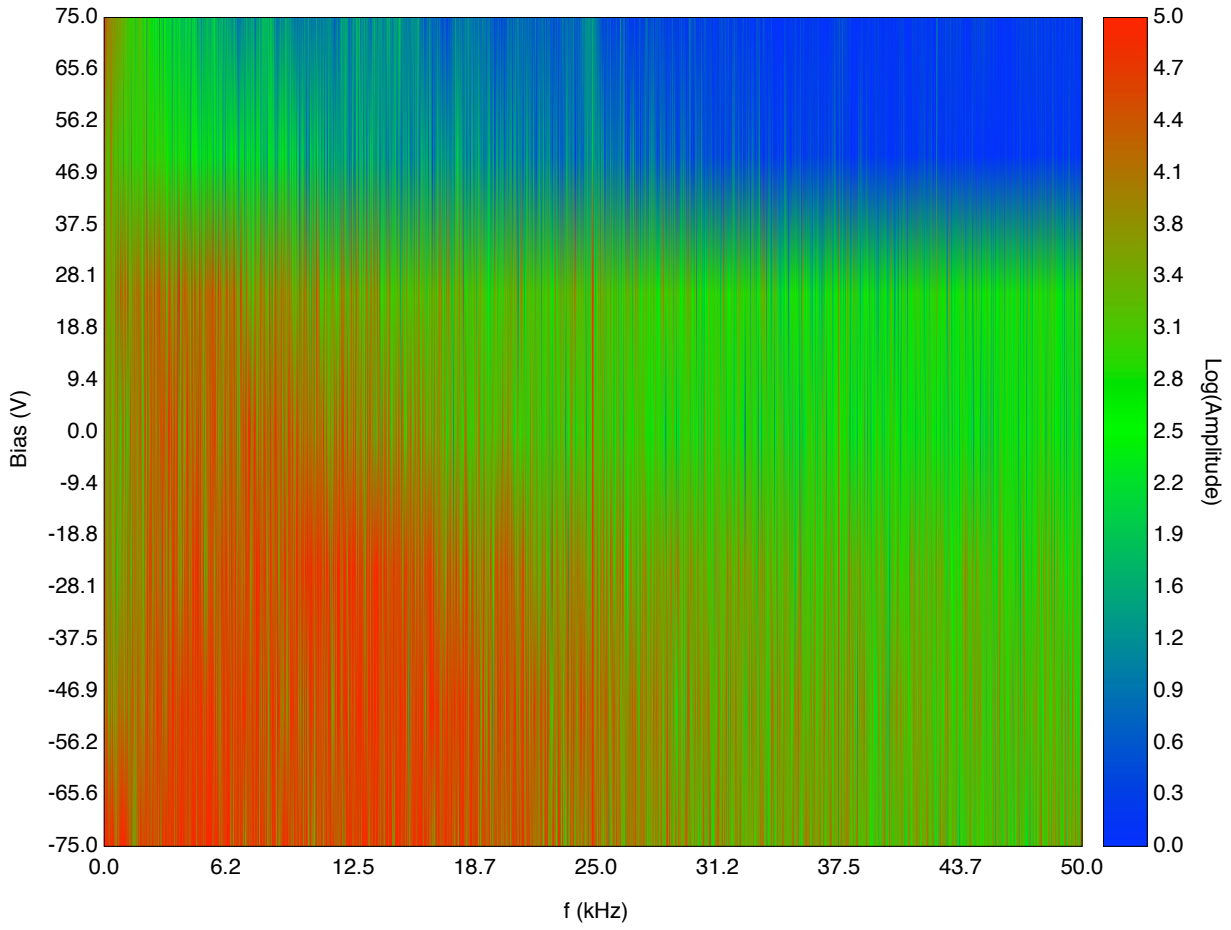

Figure 5.2: FFT if the fluctuations in Φ_f measurements at different applied biases.

due to the mounting position of probes. It has been shown in section 3.5.2 that measurements of global electric fields and density measurements are made possible through the use of the `VMEC` coordinate system provided from equilibrium reconstruction.

5.1.3 Comparison with Laboratory Experiments

Extensive work performed on linear machines shows the role that sheared flows play in the driving and suppression of plasma instabilities. In general, laboratory experiments typically have densities in the range of $n_e \sim 10^{16}$ m^{-3} and temperature of about $T_e \sim 5$ eV. Magnetic fields are generally in the range of $B \sim 0.1$ T to 0.01 T. Under these conditions, fundamental plasma frequencies, such as the ion cyclotron frequency, are on the order of $\Omega_{ci} \sim 10$ kHz and ion Larmor

radius is on the order of $\rho_i \sim 1$ cm for typical argon plasmas. By contrast, on CTH under ECRH heating in hydrogen plasmas, Densities are $n_e \sim 10^{18}$ m^{-3}. Temperatures can be produced in a comparable range. Magnetic fields are an order of magnitude higher, making $\Omega_{ci} \sim 10$ MHz and $\rho_i \sim 0.1$ mm.

Experiments on the Auburn Linear Experiment for Instability studies, show that measurements of an electrostatic ion cyclotron instability in the presence of flow shear driven by a radially inward (negative) electric field. Measurements of mode frequency show the mode frequency on the order of the ion cyclotron frequency. Biasing experiments performed on the Space Physics Simulation Chamber (SPSC) show that a sheared negative radial electric field profile drives an electrostatic ion cyclotron wave via the Inhomogeneous Energy Density Driven Instability (IEDDI) mechanism. In both these experiments, electric fields are induced in the plasma by biasing a ring electrode. Electric field scale-lengths generated are on the order of $L \sim 2 - 5$ cm which is roughly the size of the ion gyroradius. By contrast, observed modes in CTH exist in a region where mode frequencies are much less than Ω_{ci} and electric field scale-lengths are much larger than the ion gyroradius. As such direct comparison of CTH fluctuation and typical laboratory experiments cannot be performed.

5.2 Future Work

There are a number of unanswered questions and experimental regimes not covered in this dissertation. Due to limitations of experimental hardware and operational conditions, not all experimental opportunities can be explored at the moment. However, there are some possible avenues beyond the scope of this dissertation.

5.2.1 Argon Plasmas

In CTH, lowering the ion cyclotron frequency by dropping the magnetic field strength is not possible due to the use of electron cyclotron resonance heating as the primary method of generating the plasma. As such, certain magnetic field strengths on the order of $B \sim 0.5$ T are necessary to make use of the first harmonic ECRH. However, the ion cyclotron frequency can be lowered by

increasing the mass of the ions. In CTH, hydrogen plasmas have $\Omega_{ci} \sim 10$ MHz. By changing the ion mass to argon, the ion cyclotron frequency can be reduced to $\Omega_{ci} \sim 200$ kHz. The ion Larmor radius increases to $\rho_i \sim 1$ mm. If a similar electric field structure could be produced in argon plasmas, as hydrogen plasmas, it maybe possible to drive an instability closer to the conditions seen in laboratory experiments or some intermediate mode.

5.2.2 Higher Bias Voltages

Positive electric fields on CTH were only capable of producing positive electric fields in cold plasmas. Due to limitations of the biasing power supply, biasing experiments are limited to ± 100 V. The plasma could only achieve up to subsonic speeds $M \sim 0.1 - 0.2$. In experiments performed on TEXTOR, a bias of ± 600 V was able to produce positive electric fields in a plasma with much higher temperature than CTH conditions. By increasing the biasing voltage, it may simplify edge biasing experiments by expanding the range where positive edge electric fields are produced.

5.2.3 Ohmic Heating

CTH has the unique design where the device can be operated in stellarator like condition or near tokamak like conditions. Due to the fragility of diagnostics build for this dissertation it was discovered early, that operation in plasmas with driven plasma currents was not possible. If a new, more robust diagnostic can be build, CTH has the unique opportunity to bridge the gap between the early biasing experiments on tokamak device and edge biasing experiments on stellarator devices.

5.2.4 Magnetic Shear and Islands

If the conditions of electric field generation can be achieved consistently or edge rotational transform can be altered over the course of a single shot, then the effects of magnetic shear and its role in enhancing or suppressing edge plasma flows and confinement can be studied. The CTH device has a number of toroidal field coils that can alter the toroidal field and change the edge rotational transform. If the coils currents are varied enough, a rational surface can be created in

the edge. Measurements of plasma flows and confinement in the presence of magnetic islands is of specific interest in stellarators devices. However, it should be noted that the diagnostic analysis technique using VMEC, developed in chapter 2, is invalid in the presence of magnetic islands since VMEC assume nested magnetic surfaces. Future numerical studies on CTH using the NIMROD code maybe able to study the effects of magnetic islands.

5.2.5 Wavelength Measurements

As discussed in section 4.4 a true identification of the wave mode cannot be identified without a measurement of the wavenumber. It has been stated in this dissertation that a density gradient modified Kelvin-Helmholtz mode is a likely candidate for the identification of the instability mode. Estimation of wave propagation direction and structure suggest that this instability is a real plasma effect and not a power supply effect. By recreating the conditions to drive the instability observed again along with a measurement of the wavenumber, it may be possible to further confirm or reject the existence of this wave mode. Further it maybe possible to identify the structure of the turbulence like experiments performed on the CASTOR tokamak.

Bibliography

[1] S. Atzeni and J. Meyer-ter-Vehn, *The Physics of Inertial Fusion* (Oxford University Press, 2004).

[2] R. Repice, R. Adler, J. Berry, J. Micheals, R. Schmitt, *et al.*, "Annual energy review 2009," Tech. Rep. DOE/EIA-0384(2009) (U.S. Energy Information Administration, 2010).

[3] F. F. Chen, *Introduction to Plasma Physics and Controlled Fusion*, 2nd ed. (Plenum Press, 1990).

[4] C. M. Braams and P. E. Stott, *Nuclear Fusion, Half a Century of Magnetic Confinement Fusion Research* (IOP Publishing Ltd, 2002).

[5] U. Stroth, Plasma Physics and Controlled Fusion **40**, 9 (1998).

[6] H.-S. Bosch, A. Werner, R. Konig, R. Stadler, *et al.*, *Fusion Engineering, 2009. SOFE 2009. 23rd IEEE/NPSS Symposium on*, , 1 (2009).

[7] F. S. B. Anderson, A. F. Almagri, D. T. Anderson, P. G. Matthews, J. N. Talmadge, and J. L. Shohet, Fusion Technol. **27**, 273 (1995).

[8] J. Peterson, G. Hartwell, S. Knowlton, J. Hanson, R. Kelly, and C. Montgomery, Fusion Energy **26**, 145 (2007).

[9] B. A. Stevenson, *3D Reconstruction of Plasma Equilibrium using Magnetic Diagnostics on the Compact Toroidal Hybrid*, Ph.D. thesis, Auburn University (2011).

[10] F. Wagner, G. Becker, K. Behringer, D. Campbell, A. Eberhagen, *et al.*, Phys. Rev. Lett. **49**, 1408 (1982).

[11] F. Wagner, Plasma Physics and Controlled Fusion **49**, B1 (2007).

[12] M. Greenwald, R. Boivin, F. Bombarda, P. Bonoli, *et al.*, Nuclear Fusion **37**, 793 (1997).

[13] B. Tubbing, B. Balet, D. Bartlett, C. Challis, *et al.*, Nuclear Fusion **31**, 839 (1991).

[14] K. H. Burrell, S. L. Allen, G. Bramson, N. H. Brooks, *et al.*, Plasma Physics and Controlled Fusion **31**, 1649 (1989).

[15] S. Tsuji, K. Ushigusa, Y. Ikeda, T. Imai, *et al.*, Phys. Rev. Lett. **64**, 1023 (1990).

[16] R. J. Hawryluk, S. Batha, W. Blanchard, M. Beer, *et al.*, Physics of Plasmas **5**, 1577 (1998).

[17] V. Erckmann, F. Wagner, J. Baldzuhn, R. Brakel, R. Burhenn, *et al.*, Phys. Rev. Lett. **70**, 2086 (1993).

[18] M. Shigeru, M. Tomohiro, T. Kenji, *et al.*, Journal of Plasma and Fusion Research **80**, 279 (2004).

[19] R. M. McDermott, B. Lipschultz, J. W. Hughes, P. J. Catto, *et al.*, Physics of Plasmas **16**, 056103 (2009).

[20] H. Biglari, P. H. Diamond, and P. W. Terry, Physics of Fluids B: Plasma Physics **2**, 1 (1990).

[21] Z. Lin, T. S. Hahm, W. W. Lee, W. M. Tang, and R. B. White, Science **281**, 1835 (1998).

[22] T. S. Hahm, Plasma Physics and Controlled Fusion **44**, A87 (2002).

[23] K. Itoh and S.-I. Itoh, Plasma Physics and Controlled Fusion **38**, 1 (1996).

[24] P. H. Diamond, S.-I. Itoh, K. Itoh, and T. S. Hahm, Plasma Physics and Controlled Fusion **47**, R35 (2005).

[25] K. Itoh, S.-I. Itoh, P. H. Diamond, T. S. Hahm, *et al.*, Physics of Plasmas **13**, 055502 (2006).

[26] Z. Lin, T. S. Hahm, W. W. Lee, W. M. Tang, and P. H. Diamond, Phys. Rev. Lett. **83**, 3645 (1999).

[27] C. Hidalgo, M. A. Pedrosa, L. García, and A. Ware, Phys. Rev. E **70**, 067402 (2004).

[28] M. A. Pedrosa, C. Hidalgo, E. Calderón, T. Estrada, *et al.*, Plasma Physics and Controlled Fusion **47**, 777 (2005).

[29] T. Estrada, T. Happel, L. Eliseev, D. López-Bruna, *et al.*, Plasma Physics and Controlled Fusion **51**, 124015 (2009).

[30] G. Ganguli, M. J. Keskinen, H. Romero, H. R, *et al.*, J. Geophys. Res. **99**, 8873 (1994).

[31] W. E. Amatucci, D. N. Walker, G. Ganguli, J. A. Antoniades, *et al.*, Phys. Rev. Lett. **77**, 1978 (1996).

[32] E. E. Thomas Jr., J. D. Jackson, E. A. Wallace, and G. Ganguli, Physics of Plasmas **10**, 1191 (2003).

[33] G. V. Oost, J. Adḿek, V. Antoni, P. Balan, *et al.*, Plasma Physics and Controlled Fusion **45**, 621 (2003).

[34] E. E. Thomas Jr., *An Investigation of Helically Trapped Ion Orbits in the Compact Auburn Torsatron*, Ph.D. thesis, Auburn University (1996).

[35] C. Hidalgo, M. A. Pedrosa, N. Dreval, K. J. McCarthy, *et al.*, Plasma Physics and Controlled Fusion **46**, 287 (2004).

[36] S. P. Hirshman and J. C. Whitson, Physics of Fluids **26**, 3553 (1983).

[37] S. Hirshman, W. van Rij, and P. Merkel, Computer Physics Communications **43**, 143 (1986).

[38] J. D. Hanson, S. P. Hirshman, S. F. Knowlton, L. L. Lao, E. A. Lazarus, and J. M. Shields, Nucl. Fusion **49**, 075031 (2009).

[39] S. Chen and T. Sekiguchi, Journal of Applied Physics **36**, 2363 (1965).

[40] W. H. Press, S. A. Teukolsky, W. T. Vetterling, and B. P. Flannery, *Numerical Recipes: The Art of Scientific Computing*, 3rd ed. (Cambridge University Press, 2007).

[41] R. A. Jefferson, M. Cianciosa, and E. Thomas, Physics of Plasmas **17**, 113704 (2010).

[42] J. A. Stillerman, T. W. Fredian, K. Klare, and G. Manduchi, Review of Scientific Instruments **68**, 939 (1997).

[43] D. S. Sivia, *Data Analysis: A Bayesian Tutorial*, 2nd ed. (Oxford University Press, 2007).

[44] B. K. Jones, *Electronics for Experimentation and Research* (Prentice-Hall International, 1986).

[45] L. Patacchini and I. H. Hutchinson, Phys. Rev. E **80**, 036403 (2009).

[46] I. H. Hutchinson, Phys. Rev. Lett. **101**, 035004 (2008).

[47] C. P. Ritz, H. Lin, T. L. Rhodes, and A. J. Wootton, Phys. Rev. Lett. **65**, 2543 (1990).

[48] E. J. Doyle, R. J. Groebner, K. H. Burrell, P. Gohil, *et al.*, Physics of Fluids B: Plasma Physics **3**, 2300 (1991).

[49] T. S. Hahm and K. H. Burrell, Physics of Plasmas **2**, 1648 (1995).

[50] R. J. Groebner, K. H. Burrell, and R. P. Seraydarian, Phys. Rev. Lett. **64**, 3015 (1990).

[51] E. Mazzucato, S. H. Batha, M. Beer, M. Bell, *et al.*, Phys. Rev. Lett. **77**, 3145 (1996).

[52] M. E. Koepke, W. E. Amatucci, J. J. Carroll, and T. E. Sheridan, Phys. Rev. Lett. **72**, 3355 (1994).

[53] M. E. Koepke, W. E. Amatucci, J. J. C. III, V. Gavrishchaka, and G. Ganguli, Physics of Plasmas **2**, 2523 (1995).

[54] W. E. Amatucci, D. N. Walker, G. Ganguli, J. A. Antoniades, *et al.*, Phys. Rev. Lett. **77**, 1978 (1996).

[55] W. E. Amatucci, D. N. Walker, G. Ganguli, D. Duncan, *et al.*, J. Geophys. Res. **103**, 11,711 (1998).

[56] V. Gavrishchaka, M. E. Koepke, and G. Ganguli, Physics of Plasmas **3**, 3091 (1996).

[57] P. N. Guzdar, P. Satyamarayama, J. D. Huba, and S. L. Ossakow, Geophys. Res. Lett. **9**, 547 (1982).

[58] F. Brochard, E. Gravier, and G. Bonhomme, Physics of Plasmas **12**, 062104 (2005).

[59] D. G. Swanson, *Plasma Waves*, 2nd ed. (IOP Publishing, 2003).

[60] C. Hidalgo, C. Alejaldre, A. Alonso, J. Alonso, *et al.*, Nuclear Fusion **45**, S266 (2005).

[61] W. D. D'haeseleer, W. N. G. Hitchon, J. D. Callen, and J. L. Shohet, *Flux Coordinates and Magnetic Field Structure* (Spriner-Verlag, 1991).

Appendices

Appendix A
Generalized Coordinates

A brief overview for the development of generalized coordinates relevant to this dissertation, is provided from the first chapter of the book "Flux Coordinates and Magnetic Field Structure"[61]. In this section, a set a vectors defining the directions of our coordinate system is developed in a generalized manner. These direction vectors will be allowed to be non-orthonormal. As a result, definitions of common vector operations need to be redefined.

A.1 Basis Vectors

A point in three dimensional space can be specified as a vector parameterized by three independent parameters or coordinates, u^i.

$$\boldsymbol{R}\left(u^1, u^2, u^3\right) \tag{A.1}$$

By holding one coordinate constant and allowing the other two to vary, surfaces of constant u^i can be mapped out. Varying one coordinate while holding the other two constant, maps out coordinate curves. A coordinate curve along the direction of u^i is located at the intersection of coordinate surfaces defined by u^j and u^k. Figure A.1 shows the coordinate surfaces and curves for the familiar cylindrical coordinate system. The direction tangental to a coordinate curve produces covariant basis vectors. The direction normal to a coordinate surface produces contravariant basis vectors. In Cartesian coordinates, these directions are the same and there is no distinction between covariant and contravariant vectors. This will not be the case for the VMEC-coordinate system.

A.1.1 Covariant Basis

The vectors tangential to the coordinate curve (covariant basis vectors) are determined by taking the derivative of equation A.1 with respect to each coordinate.

$$\frac{\partial \boldsymbol{R}}{\partial u^i} = \boldsymbol{e}_i \tag{A.2}$$

This set of vectors forms the covariant basis set of a coordinate system. It should be noted that unlike the familiar cartesian coordinate system, the basis vectors $\boldsymbol{e}_i$ are not constrained to have any special properties such as being orthonormal or even unit-less.

A.1.2 Contravariant Basis

The vectors normal to the coordinate surface (contravariant basis vectors) are defined from the covariant basis set as

$$\boldsymbol{e}^i = \frac{1}{J}\left(\boldsymbol{e}_j \times \boldsymbol{e}_k\right) \tag{A.3}$$

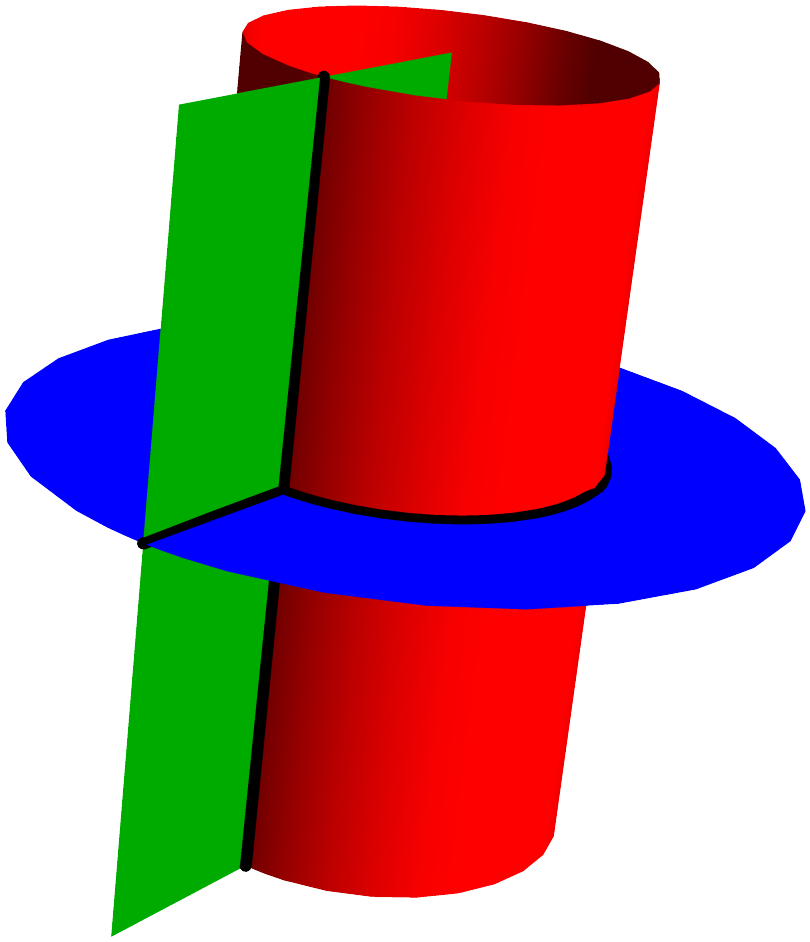

Figure A.1: Coordinate curves and surfaces for the cylindrical coordinate system (ρ, θ, z). Red $\phi = const$, Green $\theta = const$, Blue $z = const$. The black lines show the coordinate curves.

for cyclic permutations of i, j and k. J is the Jacobian and is defined to be;

$$J = \boldsymbol{e}_i \cdot \boldsymbol{e}_j \times \boldsymbol{e}_k \tag{A.4}$$

This set of vectors forms the contravariant basis set of a coordinate system. Again like the covariant basis, this set of coordinates might also not be orthonormal or unit-less. In the more familiar cartesian coordinate system, the covariant and contravariant basis sets are equal to each other. Thus no distinction is made between the two. However, in the generalized case, the differences between basis sets become important. Because these basis sets form reciprocal sets, the following relationship between basis sets holds;

$$\boldsymbol{e}_i \cdot \boldsymbol{e}^j = \delta_i^j \tag{A.5}$$

A.1.3 Metric Coefficients

A vector $\boldsymbol{D}$ maybe defined in either basis set as

$$\boldsymbol{D} = \begin{cases} \left(\boldsymbol{D} \cdot \boldsymbol{e}^1\right) \boldsymbol{e}_1 + \left(\boldsymbol{D} \cdot \boldsymbol{e}^2\right) \boldsymbol{e}_2 + \left(\boldsymbol{D} \cdot \boldsymbol{e}^3\right) \boldsymbol{e}_3 = D^1 \boldsymbol{e}_1 + D^2 \boldsymbol{e}_2 + D^3 \boldsymbol{e}_3 \\ \left(\boldsymbol{D} \cdot \boldsymbol{e}_1\right) \boldsymbol{e}^1 + \left(\boldsymbol{D} \cdot \boldsymbol{e}_2\right) \boldsymbol{e}^2 + \left(\boldsymbol{D} \cdot \boldsymbol{e}_3\right) \boldsymbol{e}^3 = D_1 \boldsymbol{e}^1 + D_2 \boldsymbol{e}^2 + D_3 \boldsymbol{e}^3 \end{cases} \tag{A.6}$$

where D^i and D_i are the contravariant and covariant components respectively of the vector $\boldsymbol{D}$. To facilitate conversion between covariant and contravariant vectors, metric coefficients are defined as

$$g_{ij} = \boldsymbol{e}_i \cdot \boldsymbol{e}_j \tag{A.7a}$$

$$g^{ij} = \boldsymbol{e}^i \cdot \boldsymbol{e}^j \tag{A.7b}$$

for the covariant and contravariant cases, respectively. When a coordinate $\boldsymbol{e}_i$ or $\boldsymbol{e}^i$ is orthogonal to $\boldsymbol{e}_j$ or $\boldsymbol{e}^j$ respectively, the associated metric coefficient is zero. We can convert the covariant components of a vector $\boldsymbol{D}$ to contravariant components, and vice versa, using the metric coefficients.

$$D_i = g_{ij} D^j \tag{A.8a}$$

$$D^i = g^{ij} D_j \tag{A.8b}$$

In this notation there is an implied summation over repeated indices. In the same manner, the conversion between basis vectors is

$$\boldsymbol{e}_i = g_{ij} \boldsymbol{e}^j \tag{A.9a}$$

$$\boldsymbol{e}^i = g^{ij} \boldsymbol{e}_j \tag{A.9b}$$

for the covariant and contravariant bases vectors respectively. A curvilinear coordinate system vector maybe transformed back in to a vector in the original coordinate system by

$$\boldsymbol{D}_{x^i} = G^T \boldsymbol{D}_{u^i} \tag{A.10}$$

where G^T

$$G = \begin{pmatrix} \boldsymbol{e}_1 \cdot \hat{\boldsymbol{x}}_1 & \boldsymbol{e}_1 \cdot \hat{\boldsymbol{x}}_2 & \boldsymbol{e}_1 \cdot \hat{\boldsymbol{x}}_3 \\ \boldsymbol{e}_2 \cdot \hat{\boldsymbol{x}}_1 & \boldsymbol{e}_2 \cdot \hat{\boldsymbol{x}}_2 & \boldsymbol{e}_2 \cdot \hat{\boldsymbol{x}}_3 \\ \boldsymbol{e}_3 \cdot \hat{\boldsymbol{x}}_1 & \boldsymbol{e}_3 \cdot \hat{\boldsymbol{x}}_2 & \boldsymbol{e}_3 \cdot \hat{\boldsymbol{x}}_3 \end{pmatrix} (Covariant) \tag{A.11a}$$

$$G = \begin{pmatrix} \boldsymbol{e}^1 \cdot \hat{\boldsymbol{x}}_1 & \boldsymbol{e}^1 \cdot \hat{\boldsymbol{x}}_2 & \boldsymbol{e}^1 \cdot \hat{\boldsymbol{x}}_3 \\ \boldsymbol{e}^2 \cdot \hat{\boldsymbol{x}}_1 & \boldsymbol{e}^2 \cdot \hat{\boldsymbol{x}}_2 & \boldsymbol{e}^2 \cdot \hat{\boldsymbol{x}}_3 \\ \boldsymbol{e}^3 \cdot \hat{\boldsymbol{x}}_1 & \boldsymbol{e}^3 \cdot \hat{\boldsymbol{x}}_2 & \boldsymbol{e}^3 \cdot \hat{\boldsymbol{x}}_3 \end{pmatrix} \ (Contravariant) \tag{A.11b}$$

is the transposed matrix of the covariant or contravariant basis vectors depending on whether the $\boldsymbol{D}_{u^i}$ is defined using the covariant or contravariant basis vectors respectively.

A.1.4 Vector Operators

From equations A.5 and A.7, there are four possible variations on the dot product operator.

$$\boldsymbol{A} \cdot \boldsymbol{B} = \begin{cases} A^i B_j \delta_j^i \\ A_i B^j \delta_i^j \\ g_{ij} A^i B^j \\ g^{ij} A_i B_j \end{cases} \tag{A.12}$$

Again there is an implied summation over repeated indices. For orthogonal systems, the cross components in the last two-forms are zero.

Unlike the dot product, there are only two natural forms of the cross product,

$$\boldsymbol{A} \times \boldsymbol{B} = \begin{cases} J \sum\limits_k \left(A^i B^j - A^j B^i \right) \boldsymbol{e}^k \\ \dfrac{1}{J} \sum\limits_k \left(A_i B_j - A_j B_i \right) \boldsymbol{e}_k \end{cases} \tag{A.13}$$

for cyclic permutations of i, j and k. The gradient operator is defined as

$$\nabla \Phi = \frac{\partial \Phi}{\partial u^i} \boldsymbol{e}^i \tag{A.14}$$

again with an implied summation over repeated indices.

A.1.5 Derivatives of Covariant and Contravariant Vectors

The MHD equations contain term of the form $(\boldsymbol{A} \cdot \nabla) \boldsymbol{A}$ where the resulting differential operator acts on each component of a vector $\boldsymbol{A}$. Unlike the cartesian coordinate system, covariant and contravariant basis vectors can be functions of their coordinates. When taking the derivative of vector one also must account for changes in the basis vectors as well. For a vector $\boldsymbol{W}$, the derivative may be taken in two ways

$$\frac{\partial \boldsymbol{W}}{\partial u^k} = \begin{cases} \left(\dfrac{\partial \boldsymbol{W}}{\partial u^k} \right)^j \boldsymbol{e}_j \\ \left(\dfrac{\partial \boldsymbol{W}}{\partial u^k} \right)_j \boldsymbol{e}^j \end{cases} \tag{A.15}$$

in terms of the covariant and contravariant basis vectors. The contravariant components can now be expanded in two ways.

$$\left(\frac{\partial \boldsymbol{W}}{\partial u^k}\right)^j = \begin{cases} \dfrac{\partial W^i}{\partial u^k}\delta_i^j + W^i \dfrac{\partial \boldsymbol{e}_i}{\partial u^k} \cdot \boldsymbol{e}^j \\ \dfrac{\partial W_i}{\partial u^k} g^{ij} + W_i \dfrac{\partial \boldsymbol{e}^i}{\partial u^k} \cdot \boldsymbol{e}^j \end{cases} \tag{A.16a}$$

$$\left(\frac{\partial \boldsymbol{W}}{\partial u^k}\right)_j = \begin{cases} \dfrac{\partial W_i}{\partial u^k}\delta_j^i + W_i \dfrac{\partial \boldsymbol{e}^i}{\partial u^k} \cdot \boldsymbol{e}_j \\ \dfrac{\partial W^i}{\partial u^k} g_{ij} + W^i \dfrac{\partial \boldsymbol{e}_i}{\partial u^k} \cdot \boldsymbol{e}_j \end{cases} \tag{A.16b}$$

Appendix B
VMEC Coordinates

VMEC is a three-dimensional MHD equilibrium solver that uses a steepest-descent moment method[36] assuming nested magnetic surfaces. For a given set of input parameters (coil currents, pressure profile, current profile, etc.) VMEC will construct the resulting plasma equilibrium. This equilibrium is solved in a flux coordinate system parameterized by coordinates s, u, and v. The s coordinate is a normalized coordinate labeling a magnetic surface. The coordinate s is normalized in such a way that $s = 0$ is the magnetic axis and $s = 1$ is the LCFS. The coordinate u represents a poloidal like angle. The coordinate v represents the toroidal angle and is the same as ϕ in the cylindrical coordinate system.

The output of VMEC is a file containing various parameters that can be used to describe the magnetic field structure at any point inside the LCFS of the CTH device. A partial list of important available parameters are provided in Table B.1. Each value is represented as a linear combination of modes of u and v. A value A may be calculated by[36];

$$A(s,u,v) = \sum_{mn} A_{mnc}(s)\cos(mu - nv) + \sum_{mn} A_{mns}(s)\sin(mu - nv) \tag{B.1}$$

The coefficients $A_{mnc}(s)$ and $A_{mns}(s)$ are defined on a grid of discrete s values. Values are defined on either a full grid starting at $s = 0$ going to $s = 1$ at regular intervals or a half grid on s positions between the full grid points. Any value in Table B.1 may be obtained at any u and v position for a given s value. However, because of the discrete nature of values in the s coordinate, an interpolation must be employed for values of s that fall between grid points.

$Value$	Name	Description	Grid spacing
$R_c\,(s)$	rmnc	Radius cos components	Full grid
$R_s\,(s)$	rmns	Radius sin components†	Full grid
$Z_c\,(s)$	zmnc	Height above the mid-plane cos components†	Full grid
$Z_s\,(s)$	zmns	Height above the mid-plane sin components	Full grid
$B_c^u\,(s)$	bsupumnc	Contravariant magnetic field component in $\boldsymbol{e}_u$ cos components	Half grid
$B_s^u\,(s)$	bsupumns	Contravariant magnetic field component in $\boldsymbol{e}_u$ sin components†	Half grid
$B_c^v\,(s)$	bsupvmnc	Contravariant magnetic field component in $\boldsymbol{e}_v$ cos components	Half grid
$B_s^v\,(s)$	bsupvmns	Contravariant magnetic field component in $\boldsymbol{e}_v$ sin components†	Half grid
$B_{sc}\,(s)$	bsubsmnc	Covariant magnetic field component in $\boldsymbol{e}^s$ cos components†	Half grid
$B_{ss}\,(s)$	bsubsmns	Covariant magnetic field component in $\boldsymbol{e}^s$ sin components	Half grid
$B_{uc}\,(s)$	bsubumnc	Covariant magnetic field component in $\boldsymbol{e}^u$ cos components	Half grid
$B_{us}\,(s)$	bsubumns	Covariant magnetic field component in $\boldsymbol{e}^u$ sin components†	Half grid
$B_{vc}\,(s)$	bsubvmnc	Covariant magnetic field component in $\boldsymbol{e}^v$ cos components	Half grid
$B_{vs}\,(s)$	bsubvmns	Covariant magnetic field component in $\boldsymbol{e}^v$ sin components†	Half grid

Table B.1: List of VMEC Output Parameters. Parameters labelled as "asymmetric" are present only in output files allowing for up-down asymmetry of the magnetic flux surfaces.

† Asymmetric Only

B.1 Basis Vectors

A position around the torus is defined in cylindrical coordinates, parameterized by flux coordinates s, u and v, as

$$\boldsymbol{R}(s,u,v) = R(s,u,v)\,\hat{\boldsymbol{r}} + Z(s,u,v)\,\hat{\boldsymbol{z}} \tag{B.2}$$

where $R(s,u,v)$ and $Z(s,u,v)$ have the form of equation B.1. When applying A.2, the derivatives with respect to u and v can be taken analytically. However, since the coefficients are only defined on discrete s positions, an interpolation or finite difference must be taken for these functions. Lastly since v is equivalent to ϕ,

$$\frac{\partial \hat{\boldsymbol{r}}}{\partial v} = \hat{\boldsymbol{\phi}} \tag{B.3}$$

The covariant basis vectors for `VMEC` coordinate system are;

$$\begin{aligned} \boldsymbol{e}_s &= \left[\sum_{mn} \frac{\partial}{\partial s} R_{mnc}(s)\cos(mu-nv) + \sum_{mn} \frac{\partial}{\partial s} R_{mns}(s)\sin(mu-nv)\right]\hat{\boldsymbol{r}} \\ &+ \left[\sum_{mn} \frac{\partial}{\partial s} Z_{mnc}(s)\cos(mu-nv) + \sum_{mn} \frac{\partial}{\partial s} Z_{mns}(s)\sin(mu-nv)\right]\hat{\boldsymbol{z}} \end{aligned} \tag{B.4a}$$

$$\begin{aligned} \boldsymbol{e}_u &= \left[-\sum_{mn} R_{mnc}(s)\,m\sin(mu-nv) + \sum_{mn} R_{mns}(s)\,m\cos(mu-nv)\right]\hat{\boldsymbol{r}} \\ &- \left[\sum_{mn} Z_{mnc}(s)\,m\sin(mu-nv) - \sum_{mn} Z_{mns}(s)\,m\cos(mu-nv)\right]\hat{\boldsymbol{z}} \end{aligned} \tag{B.4b}$$

$$\begin{aligned} \boldsymbol{e}_v &= \left[\sum_{mn} R_{mnc}(s)\,n\sin(mu-nv) - \sum_{mn} R_{mns}(s)\,n\cos(mu-nv)\right]\hat{\boldsymbol{r}} \\ &+ \left[\sum_{mn} R_{mnc}(s)\cos(mu-nv) + \sum_{mn} R_{mns}(s)\sin(mu-nv)\right]\hat{\boldsymbol{\phi}} \\ &+ \left[\sum_{mn} Z_{mnc}(s)\,n\sin(mu-nv) - \sum_{mn} Z_{mns}(s)\,n\cos(mu-nv)\right]\hat{\boldsymbol{z}} \end{aligned} \tag{B.4c}$$

The contravariant basis vectors for the `VMEC` coordinate system are obtained through equation A.3.

Magnetic fields, in this coordinate system, can be defined as either using covariant or contravariant basis vectors.

$$\boldsymbol{B} = B^u \boldsymbol{e}_u + B^v \boldsymbol{e}_v \tag{B.5a}$$

$$\boldsymbol{B} = B_s \boldsymbol{e}^s + B_u \boldsymbol{e}^u + B_v \boldsymbol{e}^v \tag{B.5b}$$

When defined using equation B.5a, the field lines have no $\boldsymbol{e}_s$ component. B^u represents a quasi poloidal component and B^v represents a quasi toroidal component. The magnetic field lines run along surfaces of constant s. Thus, the surfaces defined by a constant s coordinate represent a nested flux surface in `VMEC`. However, it should be noted that the $\boldsymbol{e}_s$ basis vector need not be orthogonal to $\boldsymbol{B}$ and need not represent a "radial" direction. From this definition we can measure an important

flux surface constant quantity in stellarators.

$$\bar{\iota} = \frac{B^u}{B^v} \tag{B.6}$$

$\bar{\iota}$ represents the measure of the twist of the field line.

Appendix C
Computer Codes Used

C.1 Shooting Code

Kelvin-Helmholtz

Shooting Code CTH

Introduction

Attempting to solve for a dispersion relation using CTH relivant parameters. The equation we are tying to solve is equation 6 in Guzdar, P. N., P. Satyanarayana, J. D. Huba, and S. L. Ossakow (1982), Influence of velocity shear on the Rayleigh-Taylor instability, Geophys. Res. Lett., 9(5), 547–550. To simplify this we start by assuming $g = 0$ and ignore, ion-neutral colsitions.

Initialization

Constants

In[1]:=
```
b0 = 0.5;
l = 0.03;
n = 10;
me = 9.1094*^-31;
```

Fuctions

Density and Potential profiles.

In[5]:=
```
ϕ0 = 17 * Tanh[# / l] + 90 &;
Plot[ϕ0[x], {x, -n * l, n * l}, PlotRange → All]
```

Out[6]=

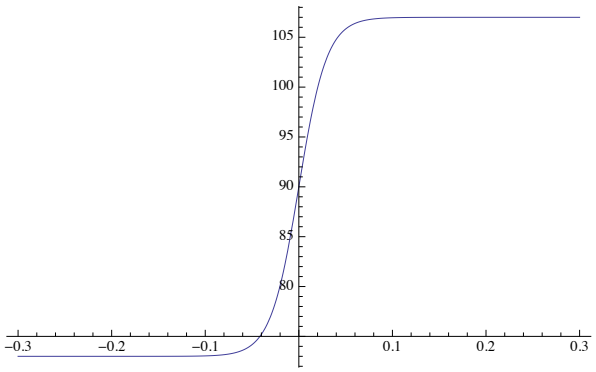

Drift velocity

In[7]:=
```
ve0 = ϕ0'[#] / b0 &;
```

In[8]:=
```
κ = #2^2 - (#2 * ve0''[#3]) / (#1 - #2 * ve0[#3]) &;
```

■ Dopler Shifted Frequency

In[9]:=
```
ω1 = #1 - #2 * ve0[#3] &;
```

Shooting Code

Set up the functions for the shooting code. Assume solutions of the form

$$e^{k_y x}$$

In[10]:=
```
shoot[Φ_, ω_, k_] :=
 NDSolve[{Φ''[x] - ϰ[ω, k, x] Φ[x] == 0, Φ[-n * l] == 0.1, Φ'[-n * l] == 0.1 * k},
   Φ, {x, -n * l, n * l}][[1]]
funct[ω_?NumericQ, k_?NumericQ] := Φ[n * l] / Exp[k * n * l] /. shoot[Φ, ω, k];
eigenValue[k_, ω0_] := ω /. FindRoot[funct[ω, k], {ω, ω0}];
```

Plots

In[13]:=
```
Plot[{Re[ϰ[1 + I, 1, x]], Im[ϰ[1 + I, 1, x]]}, {x, -n * l, n * l}]
```

Out[13]=

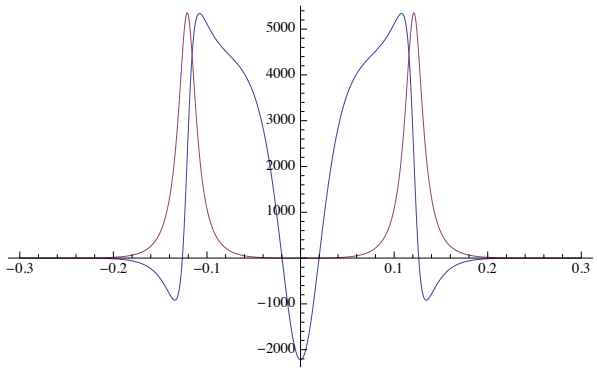

■ Frequency and Growth Rate

In[14]:=
```
<< PlotLegends`
```

In[15]:=
```
Module[{},
 ks = Table[k, {k, 2, 65, 1}];
 ev = List[eigenValue[First[ks], 0.4 * 2 * ve0[0] + 0.3 * 2 * ve0[0] I]];
 Do[ev = Append[ev, eigenValue[ks[[i]], Last[ev]]], {i, 2, Length[ks], 1}];
 ListLinePlot[{Thread[{ks, Re[ev] / 1000}], Thread[{ks, Im[ev] / 1000}]},
  PlotStyle -> {Red, Blue}, Frame → True, LegendPosition → {-0.5, 0},
  PlotLegend → {Text[Style["ωr", FontSize → 18, FontFamily → "Helvetica"]],
    Text[Style["ωi", FontSize → 18, FontFamily → "Helvetica"]]},
  ShadowBorder → None, LegendBackground → Opacity[0], ShadowBackground → Opacity[0],
  FrameLabel → {Text[Style["k m^-1", FontSize → 18, FontFamily → "Helvetica"]],
    Text[Style["ω kHz", FontSize → 18, FontFamily → "Helvetica"]]},
  FrameStyle → Directive[FontSize → 18, FontFamily → "Helvetica"],
  ImageSize -> {800, 600}]
]
```

FindRoot::lstol :
The line search decreased the step size to within tolerance specified by AccuracyGoal and PrecisionGoal but was unable to find a sufficient decrease in the merit function. You may need more than MachinePrecision digits of working precision to meet these tolerances. ≫

Out[15]=

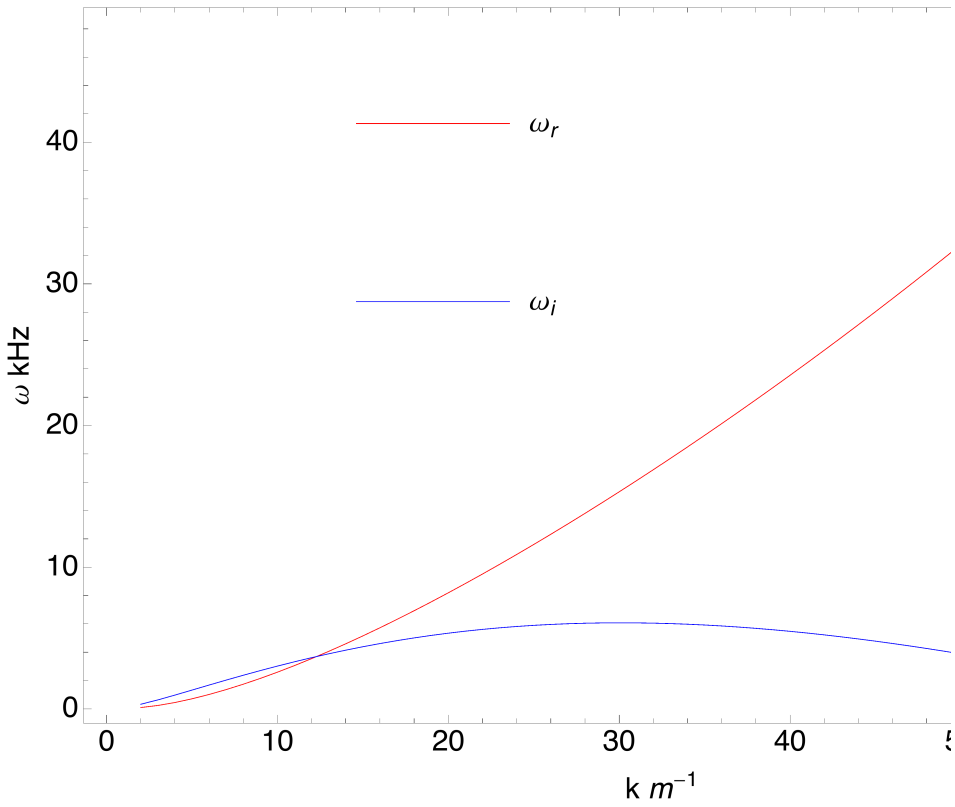

The growth rate peaks at about, $k_y = 26$. Get the eigen value at that wave length.

In[16]:=
```
ωeigen = eigenValue[30, 1 + I]
```

Out[16]= 15 320.7 + 6075. i

Check the eigen function to make sure it goes to zero at the boundary.

In[17]:=
```
Module[{},
 sol = Φ /. shoot[Φ, ωeigen, 30];
 Plot[{Re[sol[x] / sol[0]], Im[sol[x] / sol[0]]}, {x, -n * l, n * l}, PlotRange → All,
  PlotStyle -> {Red, Blue}, Frame → True, LegendPosition → {-0.5, 0},
  PlotLegend → {Text[Style["Φr", FontSize → 18, FontFamily → "Helvetica"]],
    Text[Style["Φi", FontSize → 18, FontFamily → "Helvetica"]]},
  ShadowBorder → None, LegendBackground → Opacity[0], ShadowBackground → Opacity[0],
  FrameLabel → {Text[Style["x m", FontSize → 18, FontFamily → "Helvetica"]],
    Text[Style["Φ(x)/Φ(0) ", FontSize → 18, FontFamily → "Helvetica"]]},
  FrameStyle → Directive[FontSize → 18, FontFamily → "Helvetica"],
  ImageSize -> {800, 600}]
]
```

Out[17]=

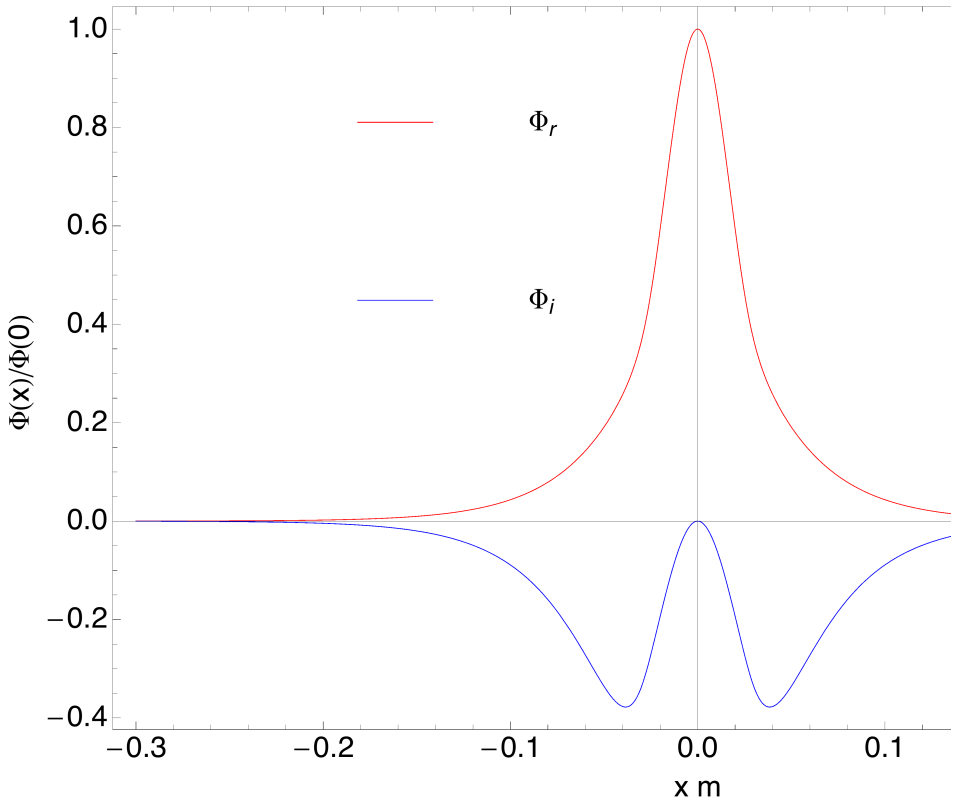

It is peaked at about, x = 0. Look at the dopler shifted frequency at that point and convert it to real frequency.

In[18]:=
```
ω1[Re[ωeigen], 30, 0] / (2 * Pi)
```

Out[18]=
```
-2972.9
```

This is inline with measured frequency. Convert the measured frequency to see if it's fits in the machine.

In[19]:=
```
2.0 Pi / 30
```

Out[19]=
```
0.20944
```

Shooting Code CTH

Introduction

Attempting to solve for a dispersion relation using CTH relivant parameters. The equation we are tying to solve is equation 6 in Guzdar, P. N., P. Satyanarayana, J. D. Huba, and S. L. Ossakow (1982), Influence of velocity shear on the Rayleigh-Taylor instability, Geophys. Res. Lett., 9(5), 547–550. To simplify this we start by assuming $g = 0$ and ignore, ion-neutral colsitions.

Initialization

Constants

In[1]:=
```
e = 1.6022*^-19;
ϵ0 = 8.8542*^-12;
b0 = 0.5;
l = 0.03;
te = 10;
ti = 1;
n = 20;
mi = 1.6737*^-27;
me = 9.1094*^-31;
Ωci = e * b0 / mi;
Ωce = e * b0 / me;
vti = Sqrt[2 * 1.60217733*^-19 * ti / mi];
ρi = vti / Ωci;
```

Fuctions

Density and Potential profiles.

In[14]:=
```
n0 = 7.45*^17 * Tanh[# / l] + 7.55*^17 &;
ϕ0 = 17 * Tanh[# / l] + 90 &;
```

Drift velocity

In[16]:=
```
ve0 = ϕ0 ' [#] / b0 &;
```

Drift Special Functions

In[17]:=
```
lnN = Log[n0[#]] &;
lnV = Log[ve0[#]] &;
```

Dopler Shifted Frequency

In[19]:=
```
ω1 = #1 - #2 * ve0[#3] &;
```

Coffeiffients

In[20]:=
```
p = lnN'[#] &;
q = -#2^2 + #2 * ve0[#3] / ω1[#1, #2, #3] (ve0''[#3] / ve0[#3] + lnN'[#3] lnV'[#3]) &;
```

Shooting Code

Set up the functions for the shooting code. Assume solutions of the form

$$e^{k_y x}$$

In[22]:=
```
shoot[Ξ_, ω_, k_] :=
 NDSolve[{Ξ''[x] + p[x] Ξ'[x] + q[ω, k, x] Ξ[x] == 0, Ξ[-n * l] == 0.1, Ξ'[-n * l] == 0.1 * k},
   Ξ, {x, -n * l, n * l}][[1]]
funct[ω_?NumericQ, k_?NumericQ] := Ξ[n * l] / Exp[k * n * l] /. shoot[Ξ, ω, k];
eigenValue[k_, ω0_] := ω /. FindRoot[funct[ω, k], {ω, ω0}];
```

Plots

Frequency and Growth Rate

In[25]:=
```
<< PlotLegends`
```

In[26]:=
```
Module[{},
 ks = Table[k, {k, 1, 54, 0.5}];
 ev = List[eigenValue[First[ks], 556.946 + 304.971 I]];
 Do[ev = Append[ev, eigenValue[ks[[i]], Last[ev]]], {i, 2, Length[ks], 1}];
 ListLinePlot[{Thread[{ks, Re[ev] / 1000}], Thread[{ks, Im[ev] / 1000}]},
  PlotStyle -> {Red, Blue}, Frame → True, LegendPosition → {-0.5, 0},
  PlotLegend → {Text[Style["ω_r", FontSize → 18, FontFamily → "Helvetica"]],
    Text[Style["ω_i", FontSize → 18, FontFamily → "Helvetica"]]},
  ShadowBorder → None, LegendBackground → Opacity[0], ShadowBackground → Opacity[0],
  FrameLabel → {Text[Style["k m^-1", FontSize → 18, FontFamily → "Helvetica"]],
    Text[Style["ω kHz", FontSize → 18, FontFamily → "Helvetica"]]},
  FrameStyle → Directive[FontSize → 18, FontFamily → "Helvetica"],
  ImageSize -> {800, 600}]
]
```

FindRoot::lstol :
The line search decreased the step size to within tolerance specified by AccuracyGoal and PrecisionGoal but was unable to find a sufficient decrease in the merit function. You may need more than MachinePrecision digits of working precision to meet these tolerances. ≫

FindRoot::lstol :
The line search decreased the step size to within tolerance specified by AccuracyGoal and PrecisionGoal but was unable to find a sufficient decrease in the merit function. You may need more than MachinePrecision digits of working precision to meet these tolerances. ≫

FindRoot::lstol :
The line search decreased the step size to within tolerance specified by AccuracyGoal and PrecisionGoal but was unable to find a sufficient decrease in the merit function. You may need more than MachinePrecision digits of working precision to meet these tolerances. ≫

General::stop : Further output of FindRoot::lstol will be suppressed during this calculation. ≫

Out[26]=

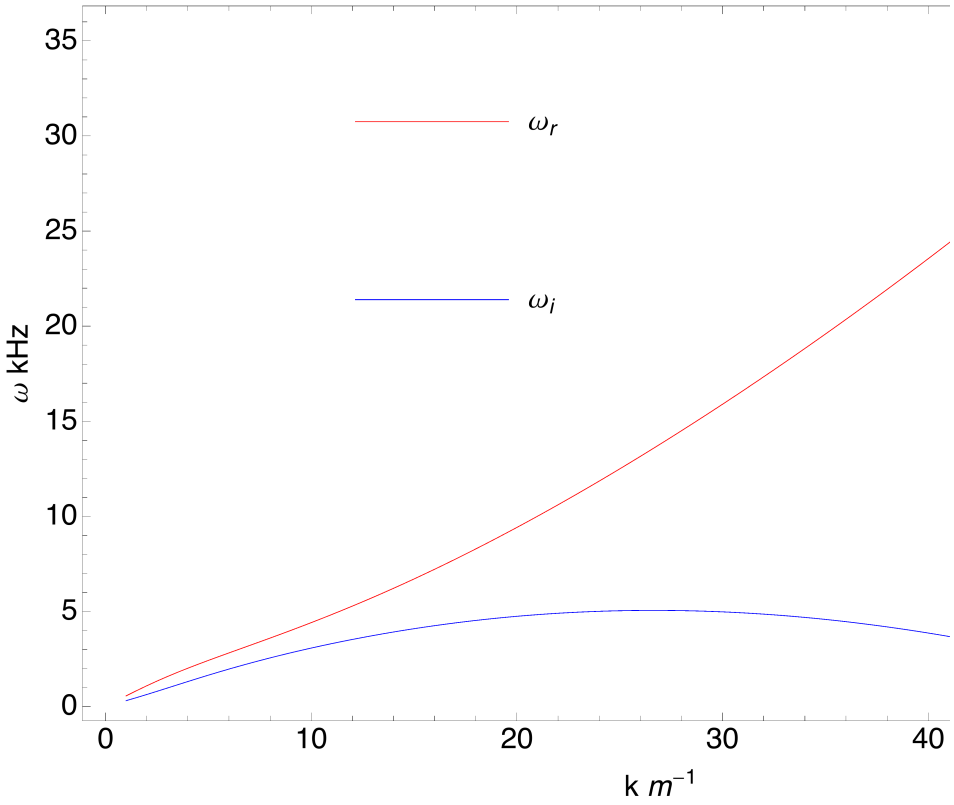

The growth rate peaks at about, $k_y = 26$. Get the eigen value at that wave length.

In[27]:=
```
ωeigen = eigenValue[26, 1 + I]
```

Out[27]=
```
13 150.6 + 5050.38 i
```

Check the eigen function to make sure it goes to zero at the boundary.

In[28]:=
```
Module[{},
 sol = Φ /. shoot[Φ, ωeigen, 26];
 Plot[{Re[sol[x] / sol[0]], Im[sol[x] / sol[0]]}, {x, -n * l, n * l}, PlotRange → All,
  PlotStyle -> {Red, Blue}, Frame → True, LegendPosition → {-0.5, 0},
  PlotLegend → {Text[Style["Φr", FontSize → 18, FontFamily → "Helvetica"]],
    Text[Style["Φi", FontSize → 18, FontFamily → "Helvetica"]]},
  ShadowBorder → None, LegendBackground → Opacity[0], ShadowBackground → Opacity[0],
  FrameLabel → {Text[Style["x m", FontSize → 18, FontFamily → "Helvetica"]],
    Text[Style["Φ(x)/Φ(0) ", FontSize → 18, FontFamily → "Helvetica"]]},
  FrameStyle → Directive[FontSize → 18, FontFamily → "Helvetica"],
  ImageSize -> {800, 600}]
]
```

Out[28]=

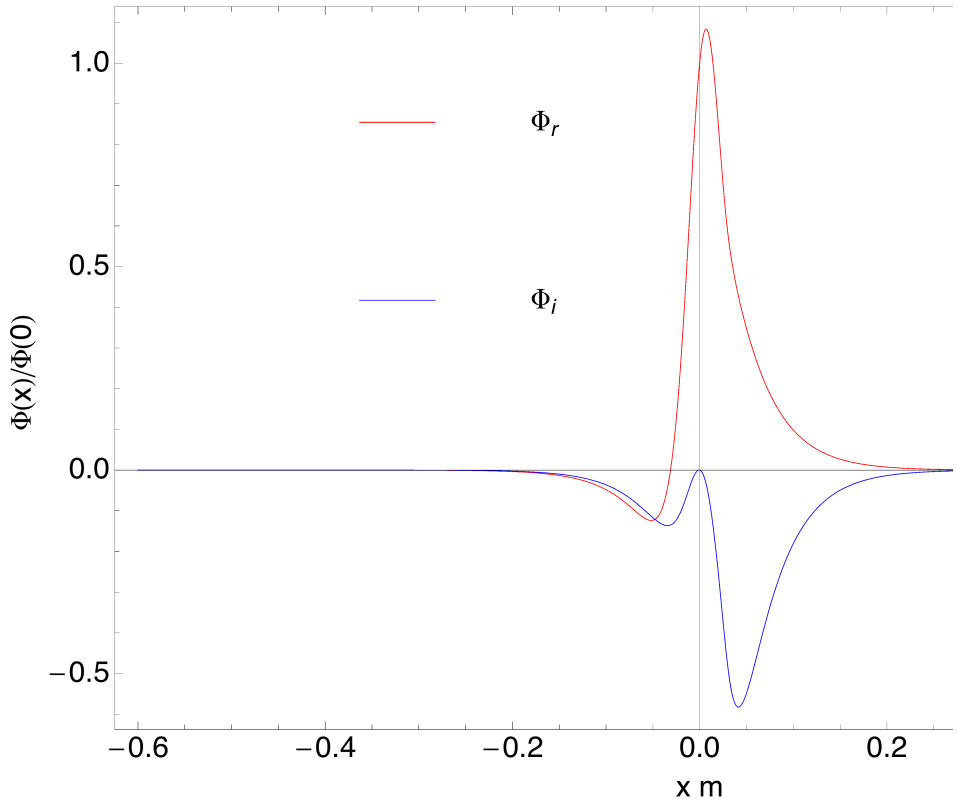

It is peaked at about, x = 0. Look at the dopler shifted frequency at that point and convert it to real frequency.

In[29]:=
```
ω1[Re[ωeigen], 26, 0] / (2 * Pi)
```

Out[29]=
```
-2596.78
```

This is inline with measured frequency. Convert the measured frequency to see if it's fits in the machine.

In[30]:=
```
2.0 Pi / 26
```

Out[30]=
```
0.241661
```

In[31]:=
```
26 * ρi
```

Out[31]=
```
0.00751615
```